Mercury optical lattice clock : from high-resolution spectroscopy to frequency ratio measurements

Maxime Favier

Maxime Favier

Pour obtenir le titre de
DOCTEUR de l'UNIVERSITÉ PIERRE ET MARIE CURIE

Sujet de Thèse :

Horloge à Réseau Optique de Mercure

Spectroscopie Haute Résolution et Comparaison d'Étalons de Fréquence Ultra-Précis

Mercury Optical Lattice Clock

From High-Resolution Spectroscopy to Frequency Ratio Measurements

Abstract

This thesis presents the development of a high-accuracy optical frequency standard based on neutral mercury ^{199}Hg trapped in an optical lattice.

We will present the experimental setup and the improvements that were made during this thesis, which have allowed us to perform spectroscopy on the doubly forbidden $^1S_0 \rightarrow {}^3P_0$ mercury clock transition at the Hz level resolution.

With such a resolution, we have been able to perform an in-depth study of the physical effects affecting the clock transition.

This study represents a factor 60 improvement in accuracy on the knowledge of the clock transition frequency, pushing the accuracy below the current realization of the SI second by the best cesium atomic fountains.

Finally, we will present the results of several comparison campaigns between the mercury clock and other state-of-the-art frequency standards, both in the optical and in the microwave domain.

Résumé

L'objet de cette thèse est le développement d'un étalon de fréquence optique basé sur l'atome de mercure ^{199}Hg piégé dans un réseau optique.

Nous présenterons le dispositif expérimental, les améliorations apportées au cours de la thèse qui ont permis d'effectuer la spectroscopie de la transition doublement interdite $^1S_0 \rightarrow {}^3P_0$ du mercure dans le domaine ultraviolet avec une résolution de l'ordre du Hz. Une telle résolution nous a permis de mener une étude approfondie des effets physiques affectant la fréquence de la transition d'horloge.

Cette étude a permis un gain d'un facteur 60 sur la connaissance de la fréquence de la transition d'horloge, et de pousser l'incertitude au delà de la réalisation de la seconde SI par les étalons de fréquence basés sur le césium.

Enfin nous présenterons les résultats de plusieurs campagnes de comparaison entre notre étalon au mercure et d'autres horloges de très haute précision fonctionnant dans le domaine optique ainsi que dans le domaine micro-onde.

Contents

Acknowledgements

First and foremost, I want to thank Sébastien Bize and Luigi De Sarlo, my PhD supervisors. Sébastien is probably the most selfless, intelligent and dedicated scientist I have ever met. His tendency to be always right has been a very important safety net throughout this thesis, and I can just hope that a few of his scientific qualities have rubbed off on me during the past three years.

Luigi and I had some epic moments in the lab during measurement campaigns, such as ending up with a Ti:Sa Lyot filter in my hand instead of actually IN the laser at 2 a.m. in the middle of the night, and some head-scratching moments while cleaning-up the electronics of the experiment. He taught me almost everything that I know about cold atoms physics and was not only the perfect scientific advisor and guide, but also a friend.

I would like to thank the members of the jury, starting with Martina Knoop and Leonardo Fallani, who accepted the task of reviewers, and contributed significant improvements to this manuscript with their re-marks and advice. I would also like to thank Thomas Udem, Philippe Grangier and Jean Michel Raimond for agreeing to be a part of the jury, and for fruitful and inspiring discussions about the research and the PhD manuscript.

From SYRTE, I want to thank first and foremost the members of the mercury team, current and past. Rinat Tyumenev was my predecessor on the experiment. Rinat, thank you for teaching me everything you knew about the experiment, and for the long hours spend taking data and listening to hard rock music in the lab. Valentin, it was a pleasure to teach you a little bit of physics and experimental techniques, as well as to discuss french politics and many other topics, and I rest assured that the future of the experiment and of the french frisbee team are in good hands. I want to also thank James Calvert and Changlei Guo,

the two "new" postdocs on the experiment that now form the mercury task-force. I know that you three will to great things on this "c*** of an experiment" (James, that one is for you). To conclude with the mercurians, I want to thank all the intern and Master's students that worked at one point or another on the experiment, with a special mention to Nicolas Galland, who very efficiently built the link between the lattice light and the frequency comb, and was a very cool person to work with. From SYRTE, I want to also thank all the members of the optical frequency group, particularly the "strontium guys" with whom I worked in close collaboration, the comb team, especially Rodolphe for countless frequency measurements throughout these 3 years and the optical fiber links team who make the long distance European comparisons possible. The frequency ratios results of Chapter 6 are also the fruit of a collaboration with the microwave fountains team and I want to wholeheartedly thank them as well. A research lab such as SYRTE wouldn't work as well (or at all for that matter) without the work of all the departments, and I want to thank everyone from the electronics department, the mechanics department, and the administrative department who all contributed to the results presented here.

To conclude, I want to thank all the people around me that not only contributed to my sanity and peace of mind, but also to my development as a human being.

I have to start with my parents, who fostered my love for physics from an early age by crafting solar systems with apple and oranges at breakfast, or by using a static-charged plastic ruler to "magically" bend a thin stream of water in the bathroom. Mom and Dad, thank you for loving me so much, and as a result, granting me the most important quality for successfully carrying-out a PhD work: faith in one's ability to succeed.

To my sister Chachou, thank you for always being my most faithful ally, and for never letting me become arrogant and full of myself (aka "le petit parfait").

J'écris ces quelques lignes en français pour le reste de la famille, qui n'a pas forcément une connaissance poussée de l'anglais. À toutes les générations, des grands-parents aux cousines, merci de votre amour et de votre soutien permanent depuis toujours, et en particulier pendant la thèse, même lorsque mon travail vous semblait parfois un peu abstrait et barbare.

A big thank you to the other members of the "first four", Kévinou, Piduss, and Théo, for many adventures, pints of beer, and philosophical discussions at 3 or 4 in the morning, and I hope many more to come. Thank you to the other members of the "colloc' de l'amour", Boubou et Nini, aka "le monstre à deux têtes" for their friendship, the many movie nights and for sharing my life during these two amazing years rue Claude Bernard. Thank you to Marion "les bons tuyaux" Gaudry for her constant bromitude, and the countless hours of heroic badminton training. I know she will always have my back. In short, thank you to all my friends for Paris, Supop', Grenoble, who one way or another, sometimes without knowing it, contributed to this thesis through their love and friendship.

As my family and close friends know, one of my defining characteristics is to always keep the best for last. Colombine, thank you for reminding me that the meaning of life cannot be found inside of a lab. Thank you for being such a smart, funny and wonderful person, thank you for always picking me up when I am down, in a nutshell, thank you for being the best partner that one could ever hope for. You're my lighthouse.

x   Acknowledgements

Introduction

0.1 Optical Atomic Clocks

Optical clocks are the new state of the art in the world of atomic frequency standards, and have surpassed microwave frequency standards in both stability [37] [7] and accuracy [75] [39] [113].

It has been recognized decades ago that an unperturbed atom with quantized energy levels can provide an ideal frequency reference by linking the energy difference between two energy levels with a frequency through Planck's relation:

$$\Delta E = E_e - E_g = h\nu_0 \tag{1}$$

An atomic frequency standard realizes the physical implementation of
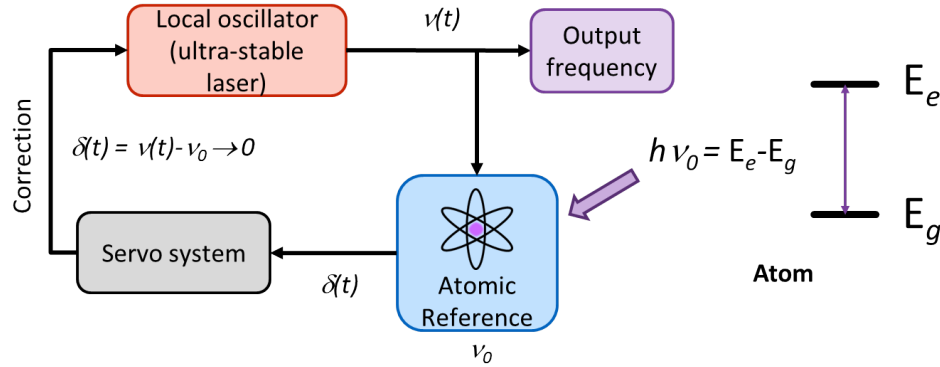
Figure 1. *Principle of a frequency standard based on an atomic transition. The frequency of a tunable macroscopic (local) oscillator $\nu(t)$ is compared against the frequency of an ultrastable atomic reference ν_0. The difference in frequency $\delta(t)$ is used to correct the frequency fluctuations and drifts of the oscillator thanks to a servo-system and keep it locked to the atomic reference. The in-loop output of the oscillator provides the useful signal of the clock which can be sent to potential users, for example via optical fiber links or microwave links.*

this concept into a useful macroscopic device (see Figure 1).

2   Introduction

In this short introduction, we will review the key aspects of such devices, as an introduction to the rest of the manuscript which deals with the implementation of an optical frequency standard based on the interrogation of laser-cooled and trapped neutral mercury atoms by an ultrastable laser.

The two most commonly used figures of merit for atomic frequency standards are accuracy and stability. The accuracy is the difference between the mean frequency of the macroscopic oscillator (usually in the microwave or optical domains) and its reference value, defined as the frequency of a specific transition of a hypothetical single, isolated, unperturbed atom in its own rest frame. The stability represents the frequency noise of the oscillator. This can be formally represented by the equation:

$$\nu_{osc}(t) = \nu_0(1 + \epsilon + y(t)) \tag{2}$$

Here, ν_0 is the reference frequency , ϵ is the offset of the mean oscillator frequency with respect to ν_0, which arises because of environmental perturbation of the atom's energy levels (the detailed study of such perturbations in the case of a clock based on neutral mercury will be the subject of Chapter 5), and $y(t)$ is the frequency noise of the oscillator. In the frequency metrology community, the uncertainty that we have on the knowledge of ϵ is called the uncertainty of the frequency standard, and $y(t)$ is called its frequency (in)stability, often characterized using the Allan variance [2] and throughout this manuscript, we will use as a measure of clock noise performance the fractional frequency instability, i.e. the square-root of the Allan variance.

Another key parameter governing the performances of any frequency discriminator is its quality factor

$$Q_{at} = \nu_0/\Delta\nu \tag{3}$$

where ν_0 is the frequency of the oscillator and $\Delta\nu$ is its linewidth.

The fractional frequency instability of an oscillator locked to an atomic transition with a quality factor Q_{at} often shows white frequency noise behavior, and we can write it as:

$$\sigma_y(\tau) \propto \frac{1}{Q_{osc}} \frac{1}{S/N} \sqrt{\frac{1}{\tau}} \tag{4}$$

where S/N is the signal to noise ratio of the spectroscopic signal, and τ is the integration time. As can be seen from Equations 4 and 3,

for a given linewidth of the atomic signal $\Delta\nu$ (which is usually set by the time spent interrogating the atomic reference, see Section 3.1.3 for a more detailed discussion in the context of this thesis), a huge gain in clock performance is to be expected when switching from microwave to optical frequency standards owing to the dependence of σ_y on the transition frequency. Indeed, microwave frequency standards have transition frequencies in the vicinity of 10^{10} Hz, while optical frequency standards possess clock frequencies above 10^{14} Hz, promising a potential improvement of the clock stability by more than 4 orders of magnitude. This is the main motivation for building optical frequency standards.

Historically, the main hindrance to the development of optical frequency standards was the evaluation and control of frequency shifts (Doppler, recoil) related to atomic motion. Indeed, a first manifestation of this occurs when probing a gas of atoms at finite temperature. A broadening of the spectroscopic signal much larger than the fundamental linewidth associated with the interrogation of a single atom can be observed [91]. This so-called Doppler broadening arises because different atoms in the gas have distinct thermal velocities, and therefore experience different Doppler shifts of the laser frequency. For a large ensemble of atoms of mass m at temperature T, this broadening is linked to the velocity distribution of the atoms in the gas and it can be written [91]:

$$\frac{\Delta\nu}{\nu} = 2\sqrt{2ln(2)\frac{k_B T}{mc^2}} \tag{5}$$

where k_B is the Boltzmann constant. This Doppler broadening is on the order of 10^{-9} for ^{199}Hg atom at 100 μK, which is representative of the case studied in this thesis. With the clock transition frequency of $\simeq$ 10^{15} Hz, this yields a Doppler-broadened linewidth of 100 kHz, much higher than the natural linewidth of the atomic transition (sub-Hz). In order to suppress frequency shifts associated with atomic motion, the most effective solution is to trap the atoms to such a small length scale (less than a wavelength of the light used to interrogate them) that atomic motion becomes quantized, the so-called Lamb-Dicke regime [117].

In this regime, the change in kinetic energy associated with the absorption of a single probe photon is small compared to the quantized energy spacing of the trap levels. An alternative way to think about

this is to consider that if an atom is confined to much less than a wavelength of the probing light, the spread of its atomic wavefunction in position space Δx_{at} verifies:

$$\Delta x_{at} \ll \frac{\lambda_{ph}}{4\pi} \tag{6}$$

where λ_{ph} is the probe wavelength. In addition, Heisenberg's uncertainty principle states that

$$\Delta k_{at} \Delta x_{at} > 1/2 \tag{7}$$

where Δk_{at} is the spread in atomic wavefunction in momentum space. Combining Equation 6 with Equation 7, we obtain

$$\Delta k_{at} >> \frac{2\pi}{\lambda_{ph}} = k_{ph} \tag{8}$$

This implies that in momentum space, the absorption of a probe photon induces a minor change of the atomic wave packet, or equivalently, when reasoning in terms of energy conservation, the shift of the resonance frequency induced by the absorption of a probe photon is small. More quantitatively, this regime is parametrized by the Lamb Dicke parameter η, which for an harmonic trapping potential writes:

$$\eta = k_{ph} \sqrt{\frac{\hbar}{2m\omega_{trap}}} \tag{9}$$

where m is the mass of the ion, ω_{trap} is the trapping frequency, and k_{ph} is the probe wave-vector. The Lamb-Dicke regime is reached when $\eta \ll 1$.

A more complete description of this regime and the physics associated with probing strongly confined atoms in the context of optical lattice clocks is discussed in Section 3.1.1.

0.1.1   Ion-based optical clocks

Trapping in the Lamb-Dicke regime was first realized with ions, since their electric charge provides a convenient mean of trapping them using the Coulomb interaction in a Paul [81] or Penning trap [19]. The conditions for Lamb-Dicke interrogation are routinely attainable using a single ion in most ion trapping apparatus which feature trapping potentials with trap frequencies in the MHz range and relatively heavy ions.

In this regime, the atomic motion in the trap appears as motional sidebands far apart ($\simeq$ MHz) from the carrier which is free of motional effects, and frequency shifts associated with 1st order Doppler effect and recoil effects vanish almost completely. For high accuracy standards, the 2nd order Doppler effect (or time-dilation shift) is still a dominant contribution to the clock accuracy, but recently this effect has been shown to be manageable at the low 10^{-18} level by realizing sympathetic cooling of the Al^+ clock ion to the 3D motional ground state, contributing a final shift of $-1.9(1) \times 10^{-18}$ [12].

Another advantage of ion clocks is that, thanks to the large confinement strength and trap depth attainable in ions traps, an ion can be trapped for several days, up to months or even years, providing long interrogation times (mostly limited by local oscillator noise) in a metrological environment, provided that the external heating rates are small enough so that they do not expel the ion out of the trap. An evaluation of these rates was performed in [22] on a Hg^+ ion clock, and the experimental findings yield a heating time constant of 95 h, mainly due to stray noise fields at radio frequencies. Incidentally, this heating rate corresponds to 6 motional quantas per second, and limits the attainable temperature after sideband cooling.

Up until a couple of years ago, optical ion clocks have held the record for atomic clock accuracy, with a Al^+ clock showing an accuracy of 8.6×10^{-18} [13], allowing for frequency ratio measurements at the 17th digit accuracy [96]. More recently, a Yb^+ clock at PTB has demonstrated an accuracy of 3×10^{-18} [39].

However, because of the strong Coulomb interaction between nearby trapped ions, operating an optical clock using multiple ions simultaneously trapped and interrogated has proven very challenging. Progress have been made towards this goal [47], but so far optical ion clocks have been mainly limited to a regime in which only a single ion is interrogated, greatly limiting the achievable clock stability, (see equation 4 and Section 4.3.1).

0.1.2   Optical lattice clocks

To benefit from the frequency stability enhancement associated with the interrogation of many atoms on an optical transition, we therefore have to work with neutral atoms. Since they do not have

an electric charge, we need to find another way to trap these particles. Luckily, focused laser light can create optical dipole traps, light structures that trap atoms by inducing an ac Stark shift of the atomic levels which is proportional to the intensity of the light [30]:

$$E_n = -\frac{1}{2}\alpha_n(\omega)|\mathbf{E_{pot}}(\omega, t)|^2 \qquad (10)$$

Where $|n\rangle$ is the particular quantum state under consideration, $\alpha_n(\omega)$ is its atomic polarizability and $E_{pot}(\omega, t)$ is the external electric field. If ω is chosen such that $\alpha_n(\omega) > 0$, then E_n becomes negative and it is therefore energetically favorable for the atoms to sit in the regions of space where the light is most intense.

A one-dimensional optical lattice consists in an array of such optical dipole traps created by counter-propagating high-intensity laser beams, possibly in an enhancement cavity configuration (see Section 1.3.3 in Chapter 1) [31]. The optical lattice potential has the form [6]:

$$U(r, z) = U_0 \exp\left[-2\left(\frac{r}{w(z)}\right)^2\right] \cos^2(k_l z) \qquad (11)$$

Where U_0 is the trap depth, defined as the difference between the asymptotic value of the potential and the potential minimum, r is the transverse coordinate, $w(z)$ is the beam width as a function of the longitudinal coordinate z, and k_l is the lattice-laser wave-vector. In the context of optical lattice clocks, the natural energy scale to describe the trap depth is the lattice recoil energy

$$E_{rec} = \frac{\hbar^2 k_{lat}^2}{2m} \qquad (12)$$

where m is the ^{199}Hg mass and $k_{lat} = 2\pi/\lambda_{lat}$. E_{rec} is the kinetic energy that a mercury atom would have if it acquired a momentum kick equal to that of a lattice photon. In the case of mercury, $E_{rec} \simeq h \times 7.57$ kHz.

Such a potential can trap several thousands of neutral atoms for extended periods of time (a few seconds in a 1D lattice, up to 1 minute in a 3D lattice [10]) allowing long interrogation pulses and therefore narrow spectroscopic resonances in the optical domain (at the Hz level or better [10]), provided that the trapping light is sufficiently far detuned from any atomic resonance in order to avoid heating the atoms out of the trap. For a detuning $\Delta = \omega_L - \omega_0$ of the trapping laser frequency ω_L from an atomic resonance with frequency ω_0 and excited

state decay rate Γ, the condition $|\Delta| >> \Gamma$ needs to be satisfied. The high attainable trap depths (several tens of recoil energies) allow complete cancellation of motional effects below the 10^{-19} level of accuracy.

However, as seen from Equation 10, in order to confine neutral atoms in the Lamb-Dicke regime, one needs an intense **optical** field, which creates a strong AC-Stark shift of the clock levels. One key point to note is that the overall shift of the the atomic clock **transition** is given by the **differential** AC-Stark shift between the two clock levels. The concept of Optical Lattice Clock put forward by H. Katori in the early 2000s [43],[106], [45] lies in the fact that since the shift is proportional to the **difference** in the atomic polarizability of the two relevant clock levels at the lattice light frequency $\Delta\nu_{LS} \propto \Delta\alpha(\nu_{lattice}) \times |\mathbf{E_{pot}}(\omega,t)|^2$, if we can find a frequency ν_m for which $\Delta\alpha(\nu_m) = \alpha_e(\nu_m) - \alpha_e(\nu_m) = 0$ (while $\alpha_n \simeq$ a few tens of $a.u.$, in order to get reasonable trap depths), then the frequency shift vanishes and becomes independent from trapping light intensity fluctuations, at least to 1st order. For a given atom, there usually exist several frequencies ν_m, and in the case of ^{199}Hg, explored in this thesis, the most convenient magic wavelength is found close to 362 nm.

A key advantage of using neutral atoms as opposed to ions is that inter-atomic interactions are much weaker (dipole-dipole interactions rather than Coulomb interaction), which means that we can trap and interrogate several thousand atoms at the same time in metrological conditions. This confers to the optical lattice clock technology a great gain in frequency stability compared to optical frequency standards based on a single trapped ion (about $\sqrt{N}$ were N is the number of atoms being interrogated, see Section 4.3.1).

In summary, provided that the optical-lattice-related shifts can be managed to the desired degree of uncertainty, we have found in the optical lattice clock the equivalent of having multiple uncorrelated ion clocks working in parallel.

0.1.3 Current and prospective applications of optical frequency standards

I would now like to emphasize several new envisioned applications for optical frequency standards, which provide the motivation for worldwide research efforts towards increasingly high levels of clock fre-

quency accuracy and stability, and for this thesis in particular.
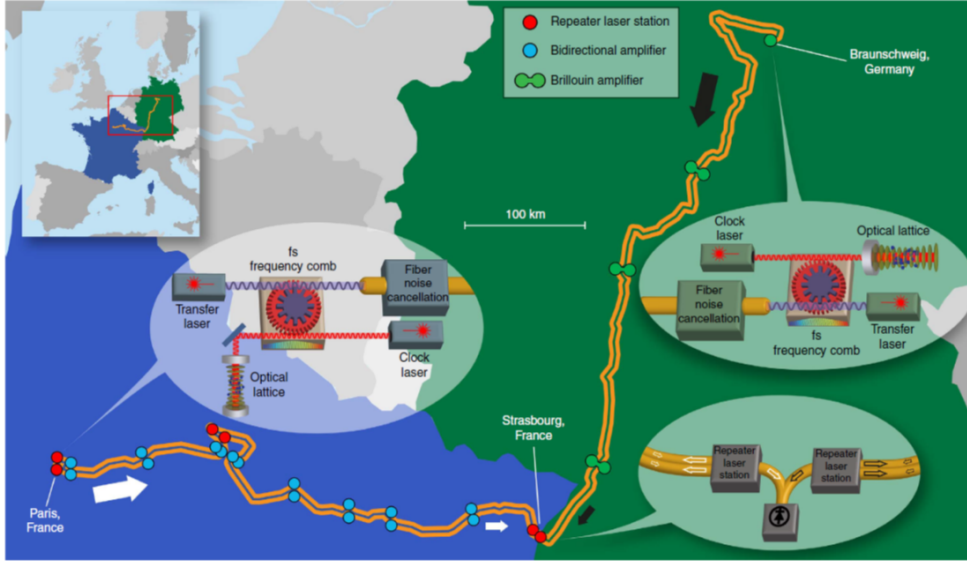
Figure 2. *Schematics of the optical fiber network linking optical atomic clocks located at PTB in Braunschweig, Germany and at SYRTE in Paris, France. Picture taken from [56].*

The first one is chronometric geodesy, namely that a measurement of the gravitational redshift of the clock transition with respect to the known bare-transition frequency can allow a local probing of the gravitational field at the position of the atoms [109]. On earth, the gravitational redshift scales as 1×10^{-16} per meter of elevation. This means that a clock working with an accuracy of 10^{-18} can probe the gravitational field with a resolution of 1 cm, making it a very useful tool for testing geoid models and for geophysics applications. To that end, transportable optical clocks are being developed in several laboratories around the world [49].

Another topic of high interest to the optical clock community is the possible redefinition of the SI second in terms of (an) optical transition(s), and the dissemination of optical time and frequency references via optical fibers networks [94]. Such a network is currently being built on the French side in a collaboration between our group and the LPL (Laboratoire de Physique des Laser) group in Villetaneuse, linking SYRTE (SYstèmes de Références Temps-Espace) in Paris with other national metrology institutes in Europe, namely NPL (National Physical Laboratory) in the UK, PTB (Physikalisch-Technische Bunde-

sanstalt) in Germany and INRIM (Istituto Nazionale di Ricerca Metrologica) in Italy [56] (see Figure 2). These fiber links also allow distant comparisons of optical clocks for fundamental physics tests [20].

Finally, another application in fundamental physics is the probing and monitoring of the variation of fundamental constants of nature, such as the fine structure constant, by looking at the time evolution of frequency ratios between clocks based on different atomic species over a few years [114] (see Section 0.2 for a more detailed discussion). These variations are predicted by many theories aiming at unifying electroweak and strong interactions (Standard Model) with gravity (currently described by General Relativity), a longstanding goal of modern physics.

0.1.4   Context and objectives of my PhD work

My PhD work, performed in the optical frequency group of SYRTE in Paris Observatory, is part of a global effort to improve the performances of optical clocks to a level compatible with applications mentioned above.

In our lab, two Strontium optical lattice clocks are currently under development, which have reached an accuracy of 4.1×10^{-17} [57] and have shown nice agreement when compared with each other, as well as great reproducibility when comparing with microwave clocks [52], [57].

On an international scale, a single clock instability of 1.4×10^{-15} at one second has been demonstrated for a single Al^+ ion optical clock [13], optical lattice clocks have shown instabilities as low as 1.4×10^{-16} at one second [102], reaching 10^{-18} measurement precision after a few thousand seconds. As far as accuracy is concerned, single ion clocks have long been the reference for optical clocks, with a single ion Al^+ clock demonstrating a total frequency uncertainty of 8.6×10^{-18} [13]. Recently, a single ion Yb^+ clock has improved upon this remarkable accuracy with a record 3×10^{-18} total frequency uncertainty [39]. Optical lattice clocks are now reaching similar accuracies at the 10^{-18} level [75], [113].

However, I want to emphasize the fact that in order to be useful tool for precision measurements, clocks have to be compared with each other, and most of the applications detailed in Section 0.1.3 rely

upon comparison of optical clocks over long distances which has been demonstrated by [109] with a resolution of 5.9×10^{-18}, and/or comparison of optical clocks based on different atomic elements for which the best published accuracy is the ratio reported in [73] with an accuracy of 4×10^{-17}.

At the beginning of this thesis, the mercury clock had demonstrated a short term stability of 5.7×10^{-15} at one second averaging time [63], and the overall accuracy of the clock was 5.4×10^{-15} [65]. The objective of my PhD work was to lower the instability and improve the accuracy of the mercury clock below the performances of state of the art microwave frequency standards, and perform clock comparisons with the mercury clock once the accuracy was established. This manuscript details the technical improvements which allowed to push the short term stability to 1.2×10^{-15} at one second, to subsequently lower the uncertainty to 9.6×10^{-17}, and finally to measure three frequency ratios involving the mercury clock.

0.2   The Mercury Atom: a Short Overview

In our experiment, we have chosen to use neutral mercury atoms as a frequency reference. I would now like to highlight a few basic properties of the mercury element.

Mercury is a chemical element with symbol Hg and atomic number 80, making it the second heaviest chemical elements ever laser-cooled. It is a liquid at room temperature (freezing point $\sim$ -40°C), removing the need for an atomic oven from the experimental constraints for building a mercury clock.

Mercury forms amalgams with many other metals. This property is important since the vacuum chamber is built out of metallic (aluminum and titanium) and glass parts, and therefore mercury will likely be adsorbed on the surface of the metallic walls of the vacuum chamber instead of being pumped out, which could have implications for the long-term quality of the vacuum reached in the science chamber.

Mercury has 7 stable isotopes, which can be found in Table 1 along with their abundance and nuclear spin. Two of these isotopes are fermions with relatively high abundance, and therefore suitable for use in a 1D optical lattice clock. This rich isotope structure allows

Atomic Mass Number	Natural Abundance	Nuclear Spin
196	0.15 %	0
198	9.97 %	0
199	16.87 %	1/2
200	23.10 %	0
201	13.18 %	3/2
202	29.86 %	0
204	6.87 %	0

Table 1. *List of the naturally occurring isotopes of mercury, along with their relative abundance and nuclear spin.*

for studies of collisional properties, and since different isotopes can have very different collisional properties, this gives us the freedom to shift from one fermion to the other if collisional shift ever becomes a problem for clock accuracy.

All the experiments discussed in this thesis have been performed using the isotope ^{199}Hg, owing to its simple atomic structure and relative abundance.

0.3 Mercury Level Structure: the Key to a Highly Accurate Frequency Standard

Following Klechkowski's rule, the electronic configuration for mercury can be written $[Xe]4f^{14}5d^{10}6s^2$. It is an alkaline-earth-like atom with 2 valence electrons, giving rise to two categories of electronic states with spin singlet and spin triplet states exhibiting long lived metastable states, making it an ideal candidate for a high accuracy frequency standard.

The structure of the energy levels of ^{199}Hg relevant for our work is shown on Figure 3. The ground state is $^1S_0$, and in our experiment, the relevant excited states are those of the triplet P state ($^3P_1$ and $^3P_0$). In commonly used alkaline-earth-like atoms like Yb or Sr, the atoms are first cooled using the broad $^1S_0 \rightarrow ^1P_1$ transition. However, in the particular case of mercury, this transition has a wavelength of 185 nm, making it highly impractical for laser cooling, and it has a 119 MHz natural linewidth, corresponding to a Doppler temperature of 2.8
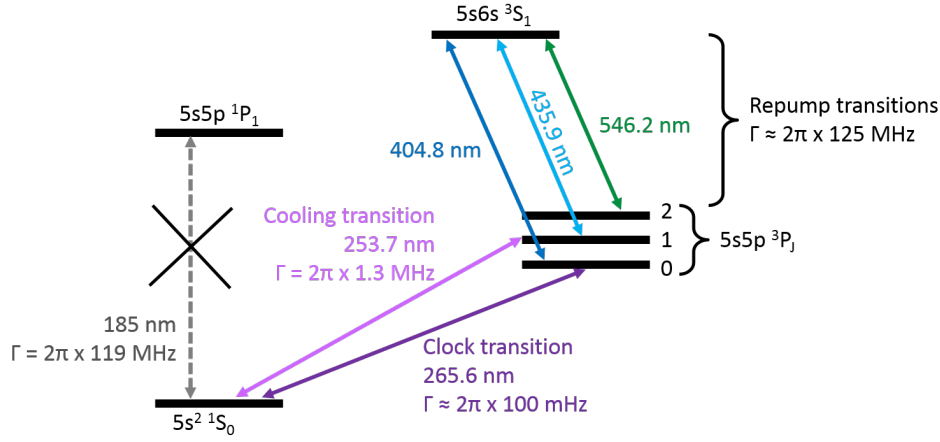
Figure 3. *Level scheme of the first excited states of neutral mercury. The atomic transitions that are used throughout this thesis to manipulate and probe the atoms are all linking the $^1S_0$ ground state to the triplet P states (see text for more details).*

mK, too high for directly loading an optical lattice.

Instead, we use single-stage cooling on the $^1S_0 \to {}^3P_1$ inter-combination line at a wavelength of 254 nm (more details on the mercury laser-cooling can be found in Chapter 1). This transition is in principle not electric-dipole-coupled, due to the dipole selection rule $\Delta S = 0$, and is only weakly allowed due to the breakdown of LS coupling (A = 8.17 $\times$ 10^6 s^{-1} [35]). This weak but closed dipole transition permits single-stage cooling below 100 μK temperatures and straightforward loading in the optical lattice.

Similarly, the $^1S_0 \to {}^3P_0$ transition is in principle strictly forbidden, but for the fermionic isotope, the presence of a non zero nuclear spin allows the hyperfine interaction to weakly mix the $^3P_0$ state with the $^1P_1$ and $^3P_1$ states, giving rise to a very weak dipole coupling (A = 0.76 s^{-1} for ^{199}Hg [4], [87]). This very weak transition has a lifetime of 1.3 s (^{199}Hg) and a natural linewidth of $\Delta\nu$ = A/2π = 121 mHz, making it a very good narrow "clock" transition. However, the wavelength of 265.6 nm presents a challenge for high resolution spectroscopy, as we will discuss in Chapter 1. Furthermore, the frequency of this clock transition is highly immune to many environmental perturbations which are the source of frequency offsets and fluctuations of atomic frequency standards. Of particular interest is the weak sensitivity of mercury to the blackbody radiation shift, which stems from the low polarizability of neutral mercury. This frequency shift is one of the limiting factor

of many neutral-atom-based optical clocks (see Section 5.5 for an in depth discussion of this effect).

We can therefore argue that the mercury atom possess key properties that make it a potential highly accurate frequency standard at room temperature, provided that the experimental challenges related to the complex laser systems needed to manipulate it can be overcome.

0.4   Thesis Overview

The thesis is structured as follows:

- **Chapter 1** is intended as a general description of the physics of the mercury optical lattice clock, an introduction to the experimental setup and provides the necessary background to apprehend the rest of the thesis. Some technical improvement, mainly to the lattice laser system are also highlighted.

- **Chapter 2** presents the new laser system for cooling of Hg which I designed and built at the beginning of my thesis, a crucial improvement to the experimental setup which enabled the results presented in the final chapters.

- **Chapter 3** deals with high resolution (Hz level) spectroscopic measurements on trapped neutral mercury atoms, an important step towards a high-stability frequency standard. A study of atomic motion inside the trap has also been performed, and used as a diagnostic tool to characterize the trapping potential, a key result for accurate evaluation of frequency shifts related to the optical lattice AC Stark effect.

- **Chapter 4** draws on the results of Chapter 3 to study experimentally and theoretically the stability of the mercury clock when locked to the atomic resonance. We then turn to the implementation of a spectral purity transfer via the operational optical frequency comb to realize correlated mercury/strontium lattice clock interrogation for high-stability frequency ratio measurements.

- **Chapter 5** details an in-depth study of the physical effects affecting the atoms and resulting in frequency shifts of the clock

transition. Several quantities are measured and, when available, compared to similar measurements reported in the literature.

- **Chapter 6** contains a detailed description of frequency ratios measurements against other SYRTE's frequency standards and a discussion of the relevance of such frequency ratios for physics and metrology.

Chapter 1

A Mercury Optical Lattice Clock

This chapter serves as a general introduction to the experimental setup and physics of the mercury optical lattice clock experiment that we are building at SYRTE.

The mercury experiment was started in 2005 from an empty lab. The vacuum chamber and a first generation of cooling laser system based on Yb:YAG disk laser technology allowed Magneto-Optical trapping of neutral mercury in 2008 [84]. The first major result fro the experiment was the first spectroscopy of the ultra-narrow clock transition performed on free falling atoms, using the newly constructed clock laser, yielding an improved (4 orders of magnitude) measurement of the ^{199}Hg clock transition frequency with an uncertainty of 5 kHz [83]. These results are reported in the PhD thesis of M. Petersen [85]. Subsequently, lattice trapping of neutral mercury using a home-made Ti:Sa laser allowed for the first determination of the magic wavelength [120] and the first clock spectroscopy performed on trapped mercury atoms [68]. Finally, a first accuracy evaluation of the mercury clock was performed in 2012 with an uncertainty of 5.7×10^{-15}, and the mercury clock was compared to a Cs microwave fountain [65]. These results were mainly limited by the poor available trap depth (20 E_{rec}) and the unreliability of the cooling laser system. The PhD thesis of R. Tyumenev [112], with whom I had a one year overlap, describes key steps toward operating the mercury experiment as a clock, with the implementation of a new doubling cavity for the generation of the cooling light at 254 nm, and a new under vacuum lattice cavity which

allowed trap depth of 50 E_{rec} to be reached.

1.1   Overview of the Experimental Setup

The purpose of this brief section is to give a general description of the mercury experiment, the different building blocks and their purposes, before providing more details in dedicated sections in the remainder of the chapter.
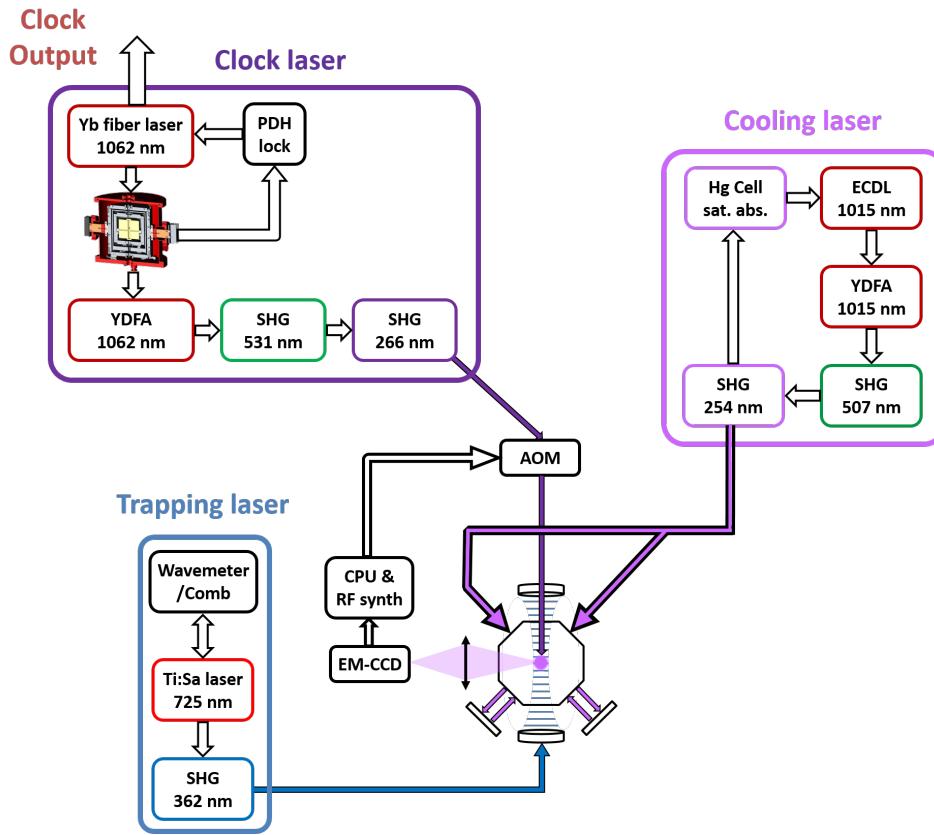
Figure 1.1. *Overview of the experimental setup of the mercury clock. The highlighted subsystems are described in more details in the text. PDH: Pound-Drever-Hall, YDFA: Ytterbium-Doped Fiber-Amplifier, SHG: Second-Harmonic Generation, OFC: Optical Frequency Comb, ECDL: External-Cavity Diode-Laser, EM-CCD: Electron-Multiplied Charge-Coupled Device, AOM: Acousto-Optic Modulator.*

An overview of the experimental setup is show on Figure 1.1.

We can separate it in 5 main subsystems, which will be the subject of detailed explanations in the next sections:

- The science chamber, where the atoms are cooled trapped and

probed. It has a very compact design, with minimal optical access, which allows for a more uniform blackbody environment around the atoms. The atomic source is a droplet of liquid mercury kept at -40°C in a copper tube thanks to a Peltier element. The atoms go through the 2D-MOT section, linked to the 3D-MOT chamber by a differential pumping section consisting of a 1.5 mm wide conical gold-plated segment, and are interrogated in a very-high-vacuum environment of $\simeq 10^{-9}$ mbar in the science chamber. The science chamber also contains under-vacuum curved mirrors forming a build-up cavity for enhanced trapping power.

- The cooling laser system, which will be the subject of Chapter 2. Briefly, we start with a home-built external cavity diode laser at 1014.9 nm, which we amplify in a commercial fiber amplifier (YDFA). This light is frequency doubled twice, first in a commercial, single-pass setup, and then in a home-built doubling cavity to reach the cooling wavelength for ^{199}Hg of 253.7 nm. This system can reliably (over the course of months) provide 50 mW of UV light to cool down mercury atoms in a 3D Magneto-Optical Trap (3D-MOT), which we will investigate in section 1.2.

- Once cooled down to a few tens of μK [64], the atoms are trapped in a vertical one-dimensional optical lattice in order to suppress Doppler effects. As was previously mentioned our setup uses a build-up cavity trap, to reach high trap depths ($\simeq 100$ E$_{rec}$). The trapping laser systems which is used to generate the 1D optical lattice, starts with a commercial Ti:Sa laser outputting up to 5.5 W at 725.2 nm, followed by frequency doubling to 362.6 nm, which is the magic wavelength for mercury [120]. The laser is referenced either to a commercial wavemeter for crude calibration and frequency-locking at the magic wavelength, or to a frequency comb when ultra-high accuracy is needed. More details can be found in section 1.3.

- The probe (or clock) laser is the local oscillator of our clock. We use it to interrogate the atoms trapped in the 1D lattice in the direction of strong confinement. We start with a Yb fiber laser at 1062.5 nm, whose linewidth is narrowed to a few hundreds of mHz by locking it to an Ultra-Stable Cavity (USC) [71], [17].

The laser is then frequency doubled twice to reach the probing wavelength close to 265.6 nm.

- The Detection is done by detecting fluorescence on the $^1S_0 \rightarrow {}^3P_1$ transition on a Electron-Multiplied Charged-Coupled Device (EM-CCD) camera. Some more details will be provided in Section 1.5.

1.2   Cooling of Mercury Atoms in a Magneto-Optical Trap

Ultimately, our goal is to trap mercury atoms in the optical lattice to suppress the huge motional (Doppler, recoil) frequency shifts associated with operating an optical frequency standards.

Since the lattice trap has a depth of a few tens of μK, we have to cool down the atomic sample to a temperature below $100\,\mu K$. One very efficient way to do that is to use laser light to Doppler-cool and trap them in a magneto-optical trap operated on a cyclic optical transition [89].

In the case of bosonic species, which lack hyperfine structure, a good estimate for the minimal obtainable temperature is given by the Doppler limit. If Γ is the natural linewidth of the cooling transition, the minimum attainable temperature in the Doppler cooling regime is

$$T_{Dop} = \frac{\hbar\Gamma}{2k_B} \tag{1.1}$$

where k_B is the Boltzmann constant.

In the case of mercury, this corresponds to $50\,\mu K$, cold enough to trap atoms in the optical lattice. Moreover, in the case of ^{199}Hg, our group has demonstrated sub-Doppler cooling effects to temperatures as low as $30\,\mu K$ [64].

1.2.1   The cooling-laser system

The laser system used to cool down mercury atoms needs to be designed taking into account the target wavelength, of course, but also the specific properties of the interrogated atomic transition. The cooling transition $^1S_0 \rightarrow {}^3P_1$ has a natural linewidth $\Gamma_{{}^3P_1}$ = 1.3 MHz, at a wavelength of 254 nm. These parameters put stringent technical constraints on the laser system.

The most straightforward way to reach such a low wavelength is to take a laser in the infra-red at 1015 nm, and frequency-double twice to reach the deep UV at 254 nm. Since several tens of mW are needed to drive the MOT transition, the infrared seed laser must be both powerful enough to yield several milliwatts of power after two stages of doubling, and have a narrow enough linewidth (sub MHz) to efficiently cool the atoms.

Prior to the beginning of this thesis, a commercial Yb:YAG thin-disk laser, designed to output 50 W at 1030 nm was modified and adapted to work at 1015 nm in order to provide the first step of the cooling system. This laser was troublesome and took several hours to warm-up.

In the meantime, high-power ytterbium-doped fiber amplifiers became commercially available. We therefore decided to design and build a new laser system for cooling mercury atoms, which will be described in its entirety in Chapter 2.

1.2.2 3D-MOT of ^{199}Hg

We will now give a few experimental details about the MOT. The MOT is operated with three orthogonal σ-polarized beams with an approximate waist of 3.3 mm retro-reflected on themselves thanks to mirrors mounted on the vacuum chamber. One of these beams is horizontal and lies along the axis of the detection (see section 1.5 for more details). The experimental sequence for the MOT is shown on Figure 1.2.

The MOT is first operated red detuned (-5.5 Γ) from resonance for 750 ms, with a quadrupole magnetic field gradient of 0.10 T m^{-1} (10 G cm^{-1} to catch as many atoms as possible in a broad range of velocity classes. The magnetic field gradient is then increased in 5 ms to 150 μT/mm and the cooling laser frequency is shifted closer to resonance (-1.5 Γ). This operation compresses the MOT cloud and allows us to get a colder and smaller cloud of atoms, greatly enhancing the loading efficiency into the optical lattice. The compression phase lasts roughly 50 ms and yields a cloud of mercury atoms whose temperature and diameter we estimate to be respectively 60 μK and 120 μm thanks to a time of flight measurement [68]. The parameters of detuning and magnetic filed gradient mentioned above are empirically determined
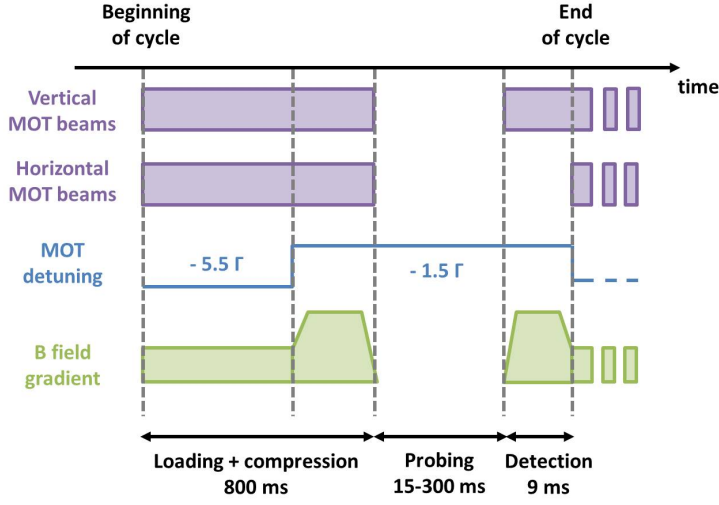
(a)
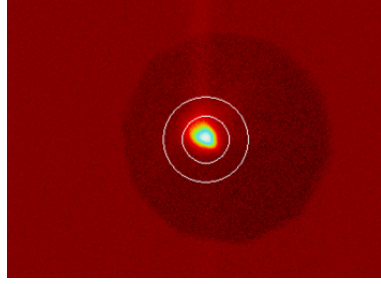
(b)

Figure 1.2. *(a) MOT experimental sequence. The loading phase is followed by a com-pression phase during which the magnetic filed is ramped-up and the cooling laser is tuned closer to resonance. The MOT is off during probing, and on again during detection. VMOT: vertical MOT arms, HMOT: horizontal MOT arm, DET: detuning (b) Fluorescence signal of the MOT trapped atoms as imaged on the EMCCD.*

capture as many atoms as possible in the MOT. The MOT light is then turned off during the probing of the atoms with the clock laser, and the vertical MOT (VMOT) beams are then turned back on for the detection.

In total, the loading time of the MOT is 800 ms and yields $\simeq 10^6$ atoms with a total (sum of the 3 MOT arms beams) UV power of 50 mW.

1.2.3   Vapor pressure and MOT lifetime

We model the MOT loading process by a constant loading rate Γ_{load}, and a loss rate Γ_{loss} which scales with the number of atoms. The atom

number then follows a simple rate equation:

$$\frac{dN}{dt} = \Gamma_{load} - \Gamma_{loss} \times N \qquad (1.2)$$

The solution to this equation is:

$$N(t) = \frac{1}{\Gamma_{loss}}(\Gamma_{load} - e^{-t/\tau}) \qquad (1.3)$$

where $N_0 = \Gamma_{load}/\Gamma_{loss}$ is the number of atoms at MOT saturation, and $\tau = 1/\Gamma_{loss}$ is the loading time of the MOT. A MOT loading curve can be seen on Figure 1.3 (a). The loading time of the MOT (during the uncompressed phase) is incrementally increased until the MOT saturation is reached. We then fit the obtained curve with equation 1.3 and extract the MOT loading time of 1.0 second and atom counts at saturation of 4×10^6 counts.

The study of the MOT loading process also gives us information about the mercury vapor pressure inside the science chamber, which is linked to the lifetime of the atoms in the lattice trap. This parameter is crucial for the clock when targeting ultimate accuracies, since collisions with hot background mercury atoms can expel atoms from the trap, reducing the achievable interrogation time, and can also create a frequency shift of the clock transition.

Over the course of one month, we have studied the effect of a reduced background pressure on the loading time of the MOT. We estimate that the residual background pressure at our operating point is $\simeq 3 \times 10^{-9}$ mbar for a current running through the Peltier element which cools down the mercury source of 0.5 A. By increasing the current driving the Peltier, we can decrease the temperature of the source, and therefore we reduce the background pressure of mercury in the science chamber.

On the plot of Figure 1.3 (b), the current in the Peltier was raised from 0.4 A to 0.55 A on the 1st of February, and again from 0.55 A to 0.6 A on the 11th. We see that it takes several days for the pressure to reach an equilibrium, and that a gain of a factor 2 on the loading time of the MOT is easily attainable.

However, this increase in lifetime comes at the price of an equal decrease in the number of trapped atoms in the MOT, which means that we have to find a compromise between good vacuum conditions for longer lifetimes in the MOT and in the lattice, and higher background

(a)

(b)
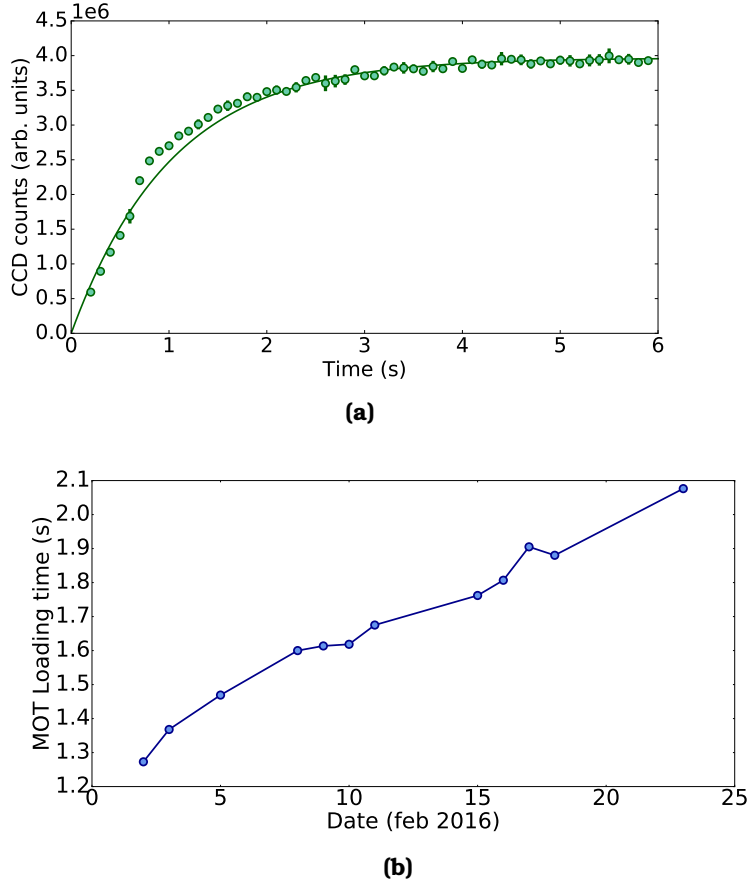
Figure 1.3. *(a) Curve of the MOT loading. Shown here is the fluorescence counts as a function of the loading time (the data points represent the average of 3 identical MOT loading curves). The solid line shows a fit with equation 1.2 which allows us to extract the key MOT loading parameters. (b) Evolution of the MOT loading time as a function of days during the course of one month while decreasing the mercury vapor pressure.*

pressure to trap more atoms. In the end, we run the experiment with a background pressure close to 4×10^{-9} mbar which we have found to be a good compromise in term of atom number and lifetime.

1.2.4   Pre-cooling with a 2D-MOT

In the very near future, we plan to enhance the MOT loading rate by using a 2D-MOT. The 2D-MOT creates a bright beam of pre-cooled atoms [95], and therefore its main effect is to greatly enhance the loading rate of the 3D-MOT.

A foreseeable benefit of this enhancement lies in the prospect of lowering the pressure in the 3D-MOT chamber. The lifetime of the

atoms in the optical lattice is approximately 300 ms (see inset of Figure 1.3 (a)). Based on our study of the MOT loading time as a function of the mercury atoms background pressure (1.3 (b)), we have good reason to believe that this lifetime, and therefore the lattice lifetime, is limited by collisions with the hot background gas of mercury atoms, whose pressure is set relatively high (several 10^{-9} mbar) to allow efficient loading in the 3D-MOT. A more efficient loading with the 2D-MOT would therefore allow us decrease the vapor pressure of mercury in the chamber, resulting in an increased lifetime of the atoms in the lattice. With longer lifetimes, we could interrogate the atoms for several hundreds of ms while keeping a good signal to noise ratio, and therefore obtain narrower linewidths.

Finally, the 2D-MOT will allow us to trap more atoms (potentially up to a factor of 10 [84], [85]), which will provide a great increase in signal to noise ratio, as well as a much needed increase in lever arm for study of collisional properties of mercury (see Chapter 5), which has been very little studied in the cold and ultra-cold regimes.

1.3   Trapping in a 1D "Magic" Optical Lattice

We will now present the experimental setup for trapping mercury atoms at the magic wavelength. As we have briefly mentioned in the introduction, the chosen magic wavelength for neutral mercury is expected to lie close to 362.5 nm. At this wavelength, the polarizability of the 2 clock states is equal to first order, and rather small ($\simeq$20 a. u., or 5.7 kHz/(kW/cm^2)) [80], [44]. This implies that a given lattice intensity will create a magic trap of relatively small depth compared for example to the case of Sr, for which the polarizability at the magic wavelength is close to 9 times higher.

The low polarizability at the magic wavelength and the need for accurate and stable control of the lattice light frequency put stringent constraints on the laser system needed to trap the atoms. Our experimental effort to meet these constraints will be the subject of the following chapter.

1.3.1   The trapping laser system

Several requirements must be met by the trapping laser system in order to reach clock performances below the 10^{-17} level.

We need a highly tunable laser, over several hundreds of MHz to study lattice light shifts and accurately pinpoint the magic wavelength. Moreover, we also want a laser which is able to generate intensities on the atoms of several Watts, both for normal clock operation, which supposes a trap depth between 50 and 100 recoil energies (corresponding to 20 W incident power on the atoms), and for lattice light-shift studies.

Finally, we want to operate the laser at the magic wavelength, whose value was measured to be close to 362.6 nm [120].

A natural choice to meet all those demands is a doubled Ti:Sa laser seeding a build-up cavity.
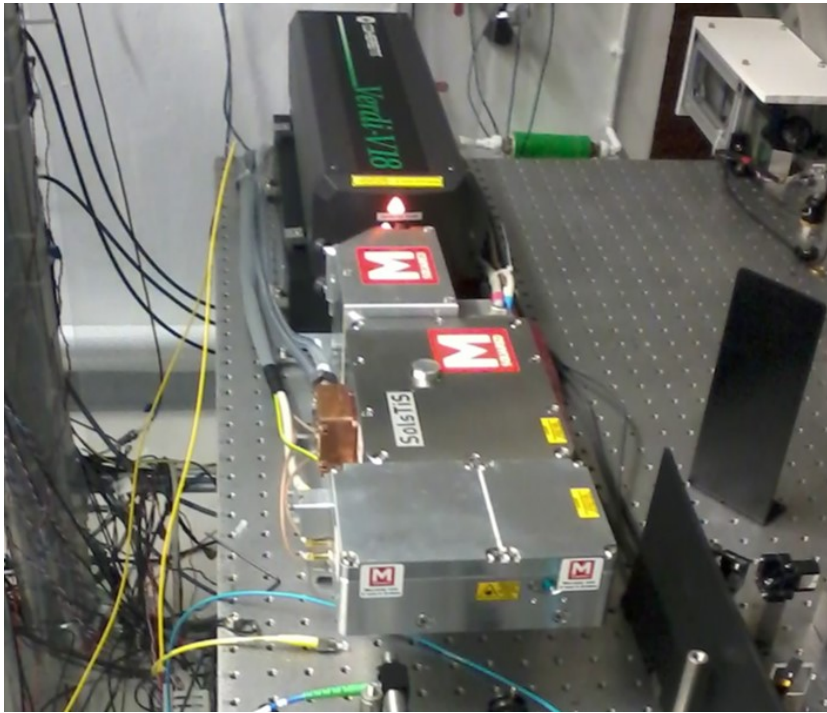
Figure 1.4. *Photo of the new commercial Ti:Sa laser pumped by a commercial system at 532 nm. This system produces the fundamental light for the lattice trap.*

We have installed and tested during the course of this thesis a new commercial Ti:Sa laser from Msquared (SolsTiS model, see Figure 1.4). This laser is pumped by 16 W of green light at 532 nm (Verdi V18) and

can output up to 5.5 W of light at 725 nm. Moreover, it is highly tunable in frequency, without mode-hop over several GHz. This laser allowed a gain of a factor 5 on the available trap depth for our experiment, greatly improving the lever-arm for the measurement of lattice related frequency shifts (see Section 5.3 for more details) as well as the number of atoms transferred from the MOT to the lattice.

This laser is fed into a home-built doubling bow-tie cavity containing a 15 mm LBO crystal and locked at resonance using the Hänsch-Couillaud locking technique. We have produced up to 800 mW of doubled light at 362.6 nm with this setup, but usually operate it with 200 mW of UV being produced out of the doubling cavity.

The SolsTiS laser has two frequency modulation inputs whose characteristics are detailed in Table 1.1.

Actuator	Voltage range	Freq. range	Sensitivity	Bandwidth
Slow PZT	$\pm$ 10 V	$\pm$ 15 GHz	1.5 GHz/V	50 Hz
Fast PZT	$\pm$ 10 V	$\pm$ 40 MHz	4 MHz/V	100 kHz

Table 1.1. *List of the different frequency actuators for the SolsTiS laser, along with their frequency ranges and sensitivities*

1.3.2 Locking scheme for the lattice light

Our prime focus is to lock the the Ti:Sa laser to (twice) the magic wavelength in order to minimize lattice light-shifts, and subsequently frequency double it to 362.5 nm. We will see in the next section (1.3.3) that in order to get a high trap depth, synonymous with many trapped atoms and potentially great lever arm on lattice light-shift measurements, a build-up cavity scheme has been implemented. Therefore, we also need to find a way to lock the Ti:Sa at resonance with the TEM$_{00}$ mode of the build-up cavity. A few constrains need to be emphasized at this point:

(i) In order to be able to control the lattice light shifts at or below the 10^{-16} level of accuracy, one needs to control the Ti:Sa frequency down to a few MHz. Indeed, since the linear lattice-shift coefficient has been measured to be $\frac{\partial \Delta \kappa^S}{\partial \nu}(\nu_{magic} = a = 1.17(6) \times 10^{-4}$ Hz/E_{rec}/MHz (see section 5.3), with an operating trap depth of 60 E_{rec}, we find easily that a detuning of only 15 MHz (10^{-8} for a car-

rier of 826 855 533 MHz) introduces a shift of 10^{-16} on the clock transition.

(ii) One of the lattice cavity mirrors is mounted on a PZT which allows for slow tuning of the cavity resonance. However, the bandwidth of the actuator is limited to a few Hz, therefore it is not fast enough to keep the cavity at resonance with the doubled Ti:Sa laser.

(iii) It is necessary, for lattice light-shift measurements as well as cold atoms manipulations in the lattice (see section 3.4) to be able to dynamically and programmatically vary the lattice depth.

This list of constraints, coupled with the available actuators on the Ti:Sa laser (see Table 1.1) shape the design of the frequency lock chain shown on Figure 1.5:
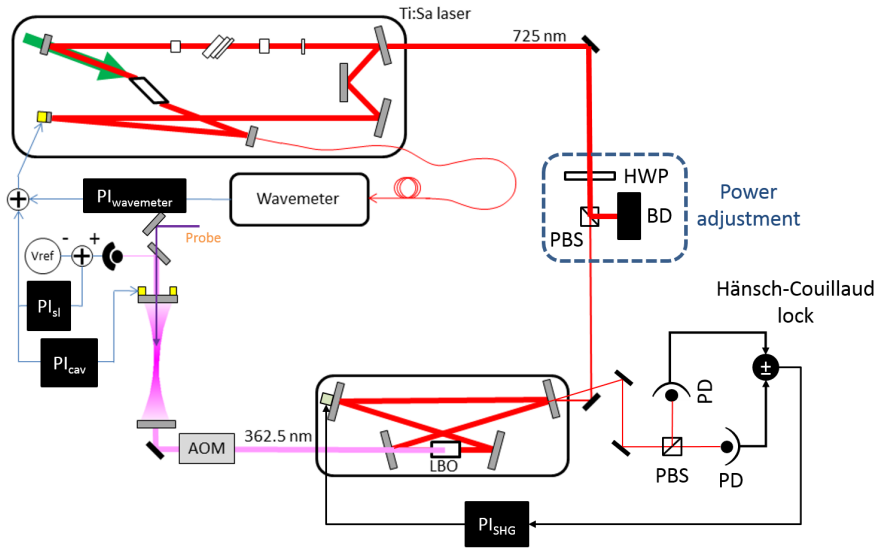
Figure 1.5. *Overall scheme of the lattice light setup. The power out of the Ti:Sa system is kept constant (5.5 W at a Verdi power of 16 W) while the power sent through the doubling cavity can be adjusted manually (Power adjustment part of the setup symbolized by the blue-dotted area). The light at 725 nm is then frequency doubled to the magic wavelength at 362 nm and coupled to the under-vacuum lattice cavity. V_{ref}, the voltage offset of the sidelock to the lattice cavity resonance, is digitally varied to change the lattice depth for different experiments. BD: Beam Dump, HWP: Half-Wave Plate, PD: Photo-Diode, AOM: Acousto-Optical Modulator.*

(i) We start by digitally locking the Ti:Sa laser to a commercial waveme-ter (PI$_{\text{wavemeter}}$ on the scheme), whose frequency accuracy is $\simeq 6$

MHz, using the slow PZT actuator. The typical timescale of the applied frequency corrections is 5s.

The doubling cavity is then kept at resonance with the light from the SolsTiS via a Hänsch-Couillaud lock reacting on one of the mirrors of the cavity (PI_{SHG} on the scheme).

(ii) We then sidelock the 362.6 nm light to the build-up cavity actuating on the fast PZT input of the laser (PI_{sl}, with a bandwidth of $\simeq$ 10 kHz. The remaining long term cavity drifts are compensated by feeding back onto the lattice cavity PZT actuator (PI_{cav} on the scheme), slowly enough (a few Hz bandwidth) so that it doesn't interfere with the sidelock.

(iii) The sidelock scheme allows us to dynamically change the lattice depth by digitally varying V_{ref}. For fast lattice modulation, an AOM, which is shown in gray on the scheme is used to modulate the build-up cavity input light intensity by "dumping" light into its 1st diffracted order.

We need to stress one potential issue with the sidelock scheme, which is that it creates an asymetric lattice light spectrum, yielding a potential frequency shift that needs to be tested when aiming for uncertainties below 10^{-17}.

We will now focus more specifically on the in-vacuum build-up cavity, a crucial part of the setup allowing us to reach the high trap depths ($<$ 100 E_{rec}) necessary for efficient estimation of lattice light-shifts.

1.3.3   A build-up cavity for a deeper trap

Mercury has a low polarizability at the magic wavelength and therefore requires high intensity light to create a lattice deep enough to trap atoms well in the Lamb-Dicke regime. For this reason, our trap is realized thanks to a build-up cavity scheme. This part of the setup was described in detials in [112] but we will quickly review the most important features.

The build-up cavity was designed to have a waist of 69 μm at the position of the atoms. To implement this, one possibility, which is the one that was chosen for our experiment is to form a cavity with two curved mirrors with radii of curvature 150 mm. The corresponding

finesse of the build-up cavity, which in first approximation is proportional to the equivalent circulating power enhancement $P_{eq} \simeq F/\pi$, was measured to be about 300.

At a constant optical power circulating in the build-up cavity set by the available laser power at the magic wavelength of 362.5 nm, one needs to find a compromise between increasing the intensity and limiting the long term damage to optics due to exposure to UV light. The depth of the lattice trap corresponding to the nominal circulating power of 5.5 W inside the build-up cavity was measured to be 60 E_{rec}. However, in order to accurately measure the lattice light-shift, we need to be able to vary the trap depth between two values with a lever arm as high as possible. Ideally we would like to explore trap depths above 200 E_{rec}, which could allow us to resolve non-linear lattice shifts.

We have therefore performed optical-damage tests of the lattice cavity mirrors and of the 362.5 nm doubling cavity optics. We estimate that operating the trap at 150 E_{rec} should pose not threat to the integrity of the lattice cavity mirrors.

1.3.4   Absolute frequency calibration with a frequency comb

In the near future, our express purpose is to control the frequency of the magic trap to the 10^{-18} level accuracy and below. With this goal in mind, we will need a better control over the lattice light-shift, and since this light-shift is proportional to the detuning of the trapping laser from the magic frequency (see section 5.3), we therefore need to control and measure this detuning better than the MHz level. As we have seen in Section 1.3.2, the commercial wavemeter which we used so far to reference the frequency of the lattice light has a frequency accuracy of 5 MHz if properly calibrated (at least every hour), and is therefore not suited for this purpose.

To resolve this issue, we have decided to reference our laser to the operational optical-frequency-comb of SYRTE. Unfortunately, the wavelength range in which the comb has a good enough signal to noise ratio to allow for a beatnote between the Ti:Sa and the comb to be realized doesn't reach below 800 nm, whereas as we have seen above, the Ti:Sa is operating at twice the magic wavelength, close to 725 nm. Therefore, in order to reference the laser to the comb, we have to divise a slightly more complicated scheme, which is shown schematically on
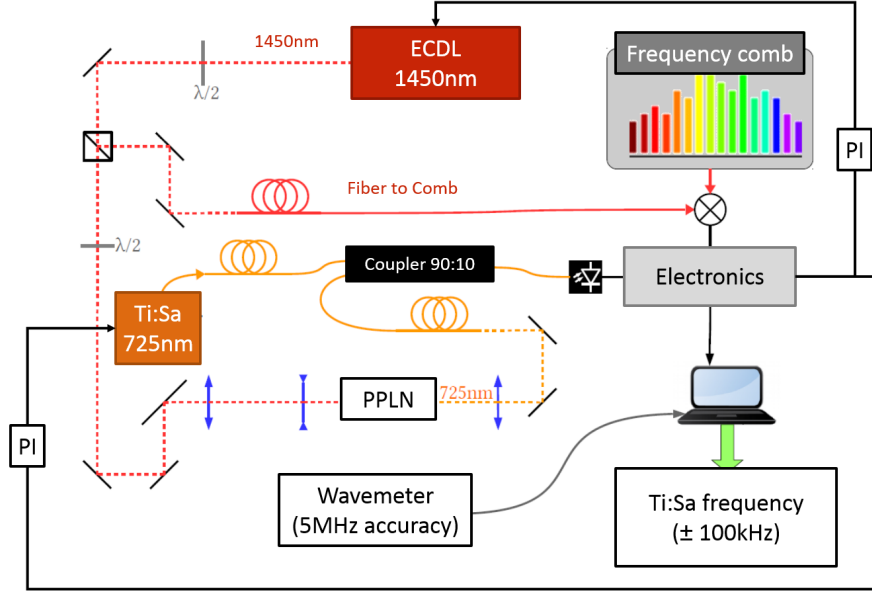
Figure 1.6. *Schematics of the setup used to lock the frequency of the Ti:Sa to the optical frequency comb using the 1450 nm ECDL as a transfer oscillator (see text).*

Figure 1.6.

We use a transfer oscillator scheme [110] to bridge the frequency gap using a ECDL laser outputting 100 mW (To check) at 1450 nm (Toptica DL100pro). A small fraction ($\simeq$ 1 mW) of the ECDL light is sent to the comb lab using an uncompensated optical fiber, and beat with a comb tooth close to 1450 nm. The resulting optical beatnote is mixed with a DDS at 34 MHz. In order to realize a digital frequency modulation lock, the DDS is frequency modulated at 1 MHz, to probe the mid-points of higher slope at the half-maxima of the beatnote. The electronics beatnote is then filtered in a 1 MHz bandwidth and subsequently demodulated providing and error signal to react on the PZT of the ECDL and lock the ECDL to the comb. In this scheme, the micro-controller is used as a digital lock-in amplifier.

The remainder of the ECDL light is frequency doubled in a single-pass configuration in a PPLN crystal to yield about 100 μW of light at 725 nm. We beat the Ti:Sa to the ECDL using the same digital lock-in modulation technique as the ECDL to the comb, using a second DDS at 70 MHz. The whole locking system and the laser fit in a standard 3U rack unit, and can stay locked for several hours without interruption.

With this, the frequency of the Ti:Sa is controlled below 100 kHz, which is good enough to control lattice-related light-shifts below the 10^{-17} level.

1.3.5   Lifetime of the atoms in the lattice

A crucial parameter for clock operation is the amount of time that the atoms stay trapped in the optical lattice before leaving the trap, because of collision with the background gas. Indeed, long trapping times allow for long interrogation with the clock laser, and therefore narrow spectroscopy signals and low clock instability.

Figure 1.7 shows the exponential decrease of the atom number in the lattice as a function of holding time for the most favorable case we have seen so far. To plot this curve, we trap the atoms in the optical lattice, and we hold them in the dark (all lasers and magnetic fields off) for a certain time before detecting. We do the experiment several time while sequentially increasing the holding time, and we plot the atomic fluorescence as a function of hold time. The experimental data are then fitted with a decreasing exponential and we extract from the fit the lifetime of the atoms in the lattice. At our nominal working point, the lifetime is $\simeq 300$ ms.
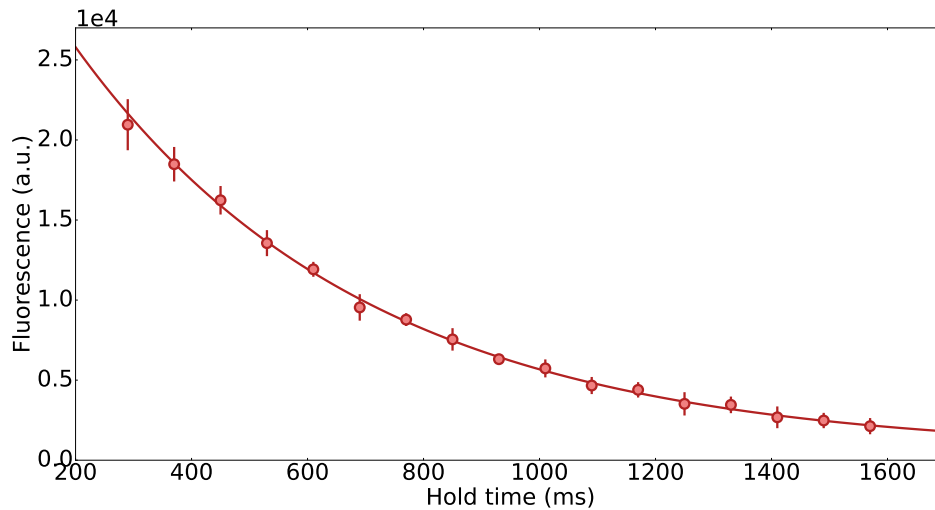
Figure 1.7.   *Curve of the lifetime of the atoms in the optical lattice. The detection fluorescence is plotted as a function of the holding time of the atoms in the lattice (see text for more details). The experimental points are fitted with a decreasing exponential with a time constant of 503 (48) ms.*

1.4 An Ultra-Stable Laser System for Coherent Atomic Interrogation

The last remaining part of the setup is the local oscillator (LO) of the clock, with which we interrogate the cooled and lattice-trapped atoms. In the case of optical clocks, this local oscillator is a laser, which has to be made ultra-stable in order to be able to resolve atomic transitions as narrow as a few Hz. We will now describe the interrogation laser of the mercury clock, starting with a few basic ideas about laser stabilization in general before describing the experimental setup fro the mercury ultrastable laser.

1.4.1 Fabry-Perot cavity for laser stabilization

In order to build a laser with an ultra-narrow frequency spectrum, two main solutions can be envisioned.

The first solution, which is currently being pursued in several groups around the world is to use a laser with a very narrow gain medium, such as the forbidden optical clock transition in alkaline-earth like atoms [67]. A first proof-of-principle was demonstrated in 2011 using Ramn transition in cold Rb atoms [8], and since then, several other experiments have been realized on ^{87}Sr atoms in a magic optical lattice [77] and on thermal untrapped ^{88}Sr atoms interrogated in an optical cavity [115]. This approach is often dubbed the "bad-cavity" approach, since the linewidth of the "bare" cavity (with no atoms inside) is much larger than the linewidth of the lasing atomic transition.

Another approach, which has been very successfully followed by most optical clock experiments worldwide in the past 20 years [48] is to use an ultra-stable cavity as an optical frequency reference and feedback onto a tunable laser (usually an ECDL or a fiber laser) using the Pound-Drever-Hall (PDH) technique. The general principle is that a cavity with length L and length fluctuations ΔL will introduce on a carrier of frequency ν_0 frequency fluctuation $\Delta\nu$ according to:

$$\frac{\Delta\nu}{\nu_0} \simeq \frac{\Delta L}{L} \tag{1.4}$$

From equation 1.4 we immediately see that if we can make $\frac{\Delta L}{L}$ very small, the cavity will act as a frequency reference for the coupled light, and we can use the signal resulting from the light/cavity interaction to

stabilize the initial laser. The ultra-stable cavity provides an excellent length reference, which is used to measure the frequency fluctuations of the laser, using the fact that the cavity is a Fabry-Perot interferometer with high-finesse, therefore providing a narrow frequency-filter around the center-frequency of the cavity mode, leading to a good frequency discriminator.
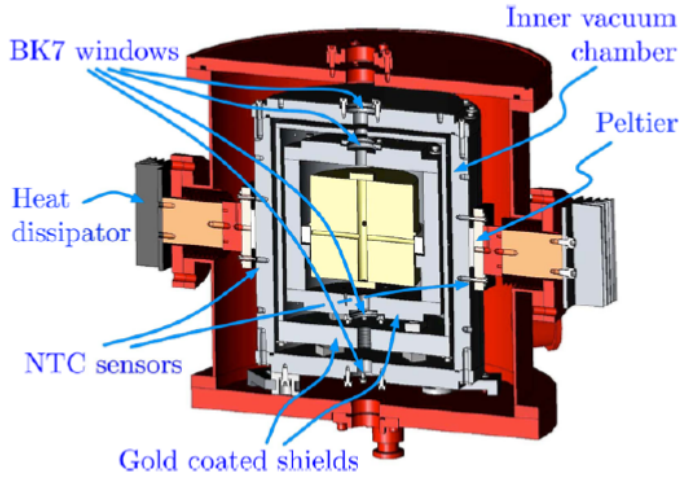
Figure 1.8. *Technical drawing of the USC taken from reference [17].*

This frequency discriminator provides an error signal to feedback on the original laser and suppress its frequency noise, down to the limit of the length fluctuations of the cavity (which usually comes from thermal noise on the cavity mirrors and coatings).

Our optical reference is a commercial fiber laser locked to a 850 000 finesse ultra-stable cavity (USC) via the PDH technique. The cavity is made of two high-finesse mirrors (one flat and one concave with a 500 mm radius of curvature) optically contacted to a 10 cm long ULE (Ultra-Low Expansion glass) spacer (chosen for its high insensitivity to temperature fluctuations) [17]. This cavity is then enclosed in three thermal shields whose temperature are stabilized and monitored continuously, and put under vacuum as shown on Figure 1.8. This system has demonstrated a flicker FM noise floor corresponding to a stability of less than 5×10^{-16}, verified by beating it with another similar system [71]. Table 1.2 summarizes the characteristics of the USC.

Length	10 cm
Finesse	850 000
Cavity linewidth	1.5 kHz
Flicker	5×10^{-16}
Locked-laser linewidth	< 1 Hz

Table 1.2. *Important parameters of the USC and probe laser system.*

1.4.2   Ultra-stable laser setup

Let us now describe the setup used to bring ultrastable light in the UV at 265.6 nm to the mercury atoms trapped in the optical lattice inside the vacuum chamber. The overall clock laser system is shown on Figure 1.9.
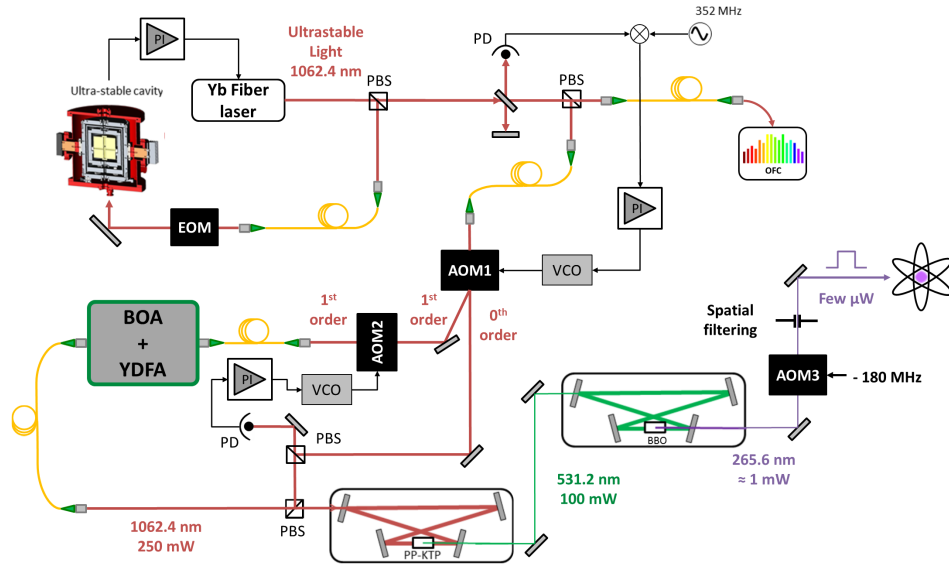
Figure 1.9. *Clock laser setup, generating tunable ultra-stable light at 265.6 nm for interrogating mercury atoms on the clock transition. AOM1 allows for active dedrift of the clock laser and phase-noise cancellation of the optical fiber link bringing the ultrastable light to the main table, AOM2 is used to phase-lock the YDFA to the input seed signal, and AOM3 produces the clock light pulses for atomic interrogation.*

We start with the 1062 nm commercial fiber laser (Koheras Boostik) which is PDH-locked to the USC as described in section 1.4.1 above. We then send the Ultra-stable Light (USL) via a fiber-noise canceled optical fiber to the main optical table, and amplify it in two stages. The first stage is a semiconductor amplifier, followed by a commercial Yb

doped Fiber-Amplifier[1] (YDFA) yielding up to 2 W of light at 1062 nm. This amplification step is necessary to provide us with enough power before frequency quadrupling to the clock wavelength close to 265.6 nm, but it can also introduce some unwanted phase-noise on the USL. We therefore implement a phase locked loop by beating the output of the amplifier with its input, and reacting on AOM1 (see scheme of Figure 1.9).

Finally, two stages of resonant frequency doubling are implemented with a PPsLT followed by a BBO crystal placed in two cascaded bow-tie optical cavities to reach 265.6 nm. AOM3, driven at 180 MHz, is used to produce the clock pulses with tunable power and durations as needed for the clock operations. The frequency of the clock laser can be tuned thanks to a Stanford SRDS35 digital synthesizer driving AOM2, while a second synthesizer provides a tunable dedrift removing the drift of the USC on the light seen by the atoms.

1.4.3   Laser noise and frequency doubling

We now want to estimate the laser noise added through the optical doubling process, to try to evaluate the laser noise imprinted onto the atoms in the UV. We first characterize the noise of the USL in the infrared looking at the error signal of the PDH lock. The FFT of the in-loop error signal is shown on Figure 1.10. A more detailed discussion of the noise level and impact on the stability of the clock can be found in Chapter 4.

We then characterize the added noise caused by the beam passing through the doubling cavities and the doubling process by looking at the RIN of the photodiodes used to lock the doubling cavities at resonance. The RIN curves are shown on Figure 1.11.

The assumption here is that the light intensity fluctuations inside the cavities are mainly caused by frequency noise, and therefore looking at the RIN of the locking photodiodes when the cavities are locked gives us an idea of the noise added to the laser. The RINs show an increase of 6 dB of white noise after the first frequency doubling stage, and another 6 dB after the second one, compatible with the expected added phase noise on the laser after frequency doubling of a factor of 4 (factor of 16 in total, 12 dB for two doubling stages).

---

[1]From Nufern
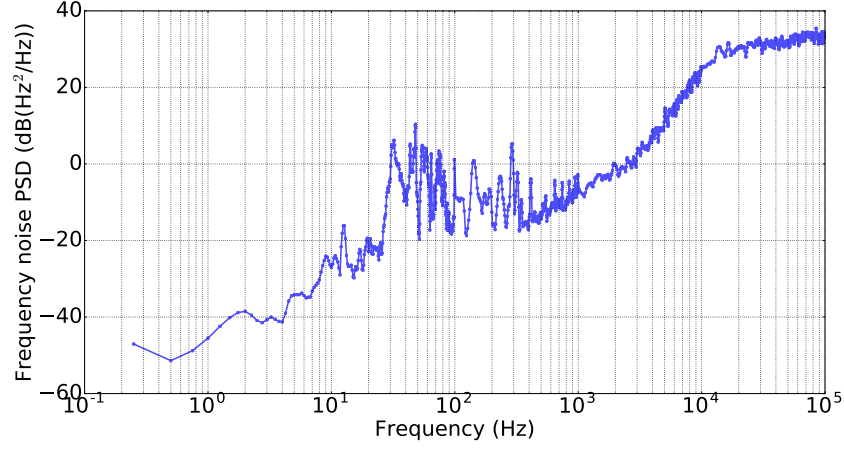
Figure 1.10. *Fast Fourier transform of the error signal of the PDH (Pound Drever Hall) lock to the ultra-stable cavity.*
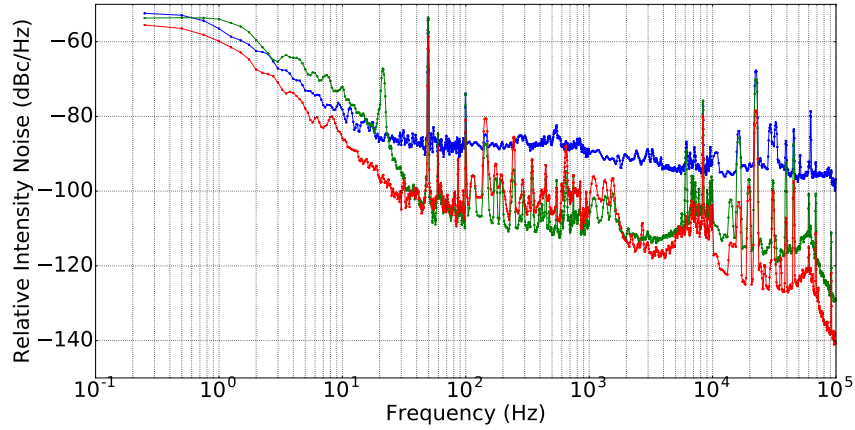
Figure 1.11. *Relative Intensity Noise (RIN) of the locking photodiodes of the doubling cavities for the probe beam. The red trace shows the infrared leakage from the fundamental signal of the first doubling cavity, the green trace show the doubled green light from the first doubling stage, and the blue trace shows the monitoring of the UV light generated after the second doubling stage.*

We can therefore assume that the atoms are probed in the UV with a clock laser which characteristics are the ones shown on Figure 1.10 with a factor of 16 added white phase noise.

This simple analysis leaves out the fact that there is a several tens of centimeter uncompensated path length between the second doubling cavity and the atoms, as well as the AOM used to shape the clock pulses (AOM3 of Figure 1.9) which is susceptible to add a phase chirp to the probe laser field creating an unwanted frequency shift when interrogating the atoms (more on that in Section 5.6).

1.5   Fluorescence Detection

Once the atoms have been trapped in the lattice and interrogated by the clock laser, their quantum state must be read-out by a suitable detection system to provide the useful clock output signal. The detection setup is shown on Figure 1.12. In the present scheme, we detect the atoms on the same path as one of the MOT arms [68], reducing the required optical access on the setup.

In order to do that, one has to take advantage of the fact that the MOT beam is collimated, while the atoms fluorescence is roughly emitted from a point source (the MOT, which has a radius of $\simeq 100\ \mu m$). Therefore, lens L can be used both to collimate the fluorescence from the atoms onto a half-mirror, (HM in the picture) and redirect it toward the detection arm at 90° from the MOT arm, and to focus the MOT arm in order to purposely miss the half-mirror and avoid sending parasitic light towards the CCD.

The magnification of the optical system used to image the MOT fluorescence is 100/90 = 1.1, and the EMCCD (Andor 897) is cooled down to -80 °C to reduce dark noise. A very important parameter of the clock is the number of atoms being probed and subsequently detected in the optical lattice. It is especially relevant to the study of the collisional frequency shift and needs to be estimated.

We therefore need to derive the link between the measured number of counts on the CCD, N_{counts}, and the effective number of atoms N_{atoms}.

$$N_{atoms} = \frac{\eta_e}{\eta_{ph} G F \gamma_p \tau_{exp}} \times N_{counts} \qquad (1.5)$$

Where η_e = 22.4 is the number of electrons per count, η_{ph} = 0.33 is
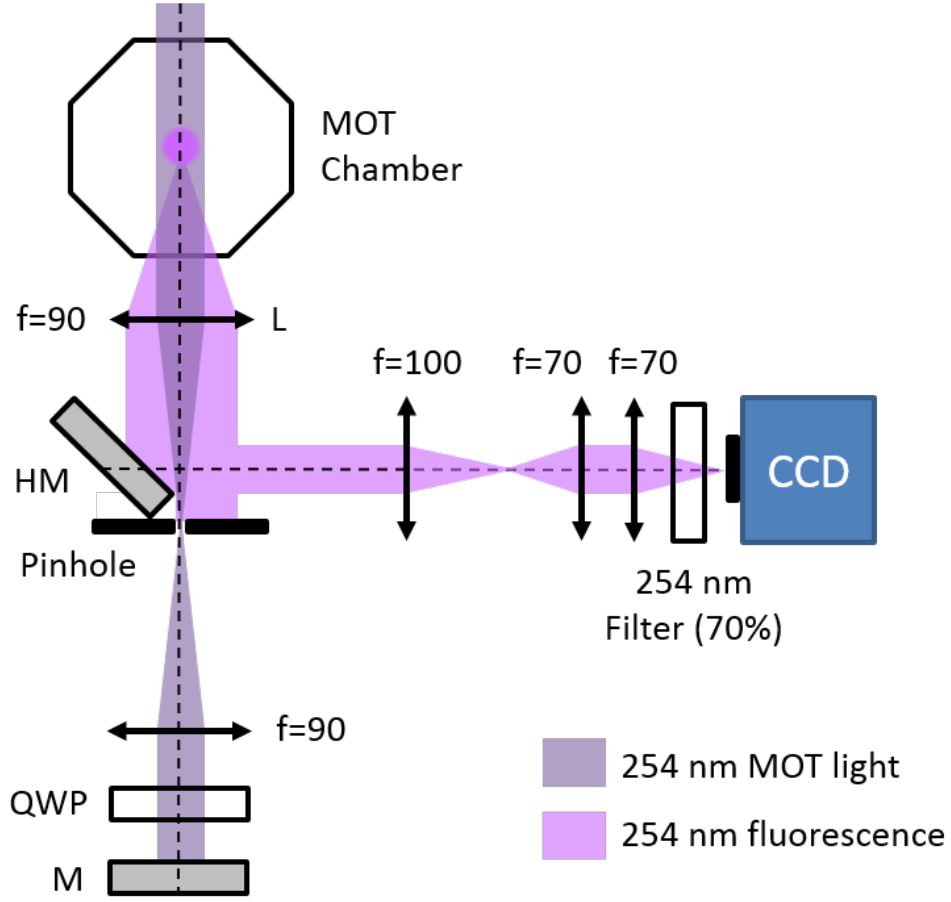
Figure 1.12. *Optical setup for the detection of the atoms along one of the MOT arms. The MOT light is focused by lens L and misses the HM, while the atomic fluorescence is collimated and sent to the detection system. QWP: Quarter-Wave Plate, HM: Half-Mirror, M: Mirror, f: focal length.*

the quantum efficiency (number of electrons generated per photon incident on the CCD), G is the electron multiplication gain, F is the collected fraction of fluorescence photons, which we will compute thanks to the aperture of the detection system, γ_p is the scattering rate of the atoms, and τ_{exp} is the exposure time. The scattering rate γ_p can be written:

$$\gamma_p = \frac{2s_0\Gamma}{1 + s_0 + (2\delta/\Gamma)^2} \tag{1.6}$$

Where $s_0 = I/I_{sat}$ is the 254 nm beam total intensity normalized by the saturation intensity. s_0 is also called the **saturation parameter**. Our detection is carried out at a constant detuning of -1.5 Γ from resonance. Moreover, we usually run the clock with 50 mW of light

at 254 nm collimated to a beam of $\simeq$ 15 mm diameter, yielding an intensity of 284 W/m^2 and an s_0 of 2.8. Therefore, we estimate γ_p to be 0.56×10^6 photons/s.

The only parameter left to estimate is the collected fraction of fluorescence photons F. We know that the solid angle in which are emitted the photons susceptible to reach the CCD is half the solid angle of the cône of apex $\alpha = \arctan(11.5/90)$ where 11.5 mm is the radius of the collimating lens and 90 mm is its focal length. We can write this solid angle as $\Omega = 1/2 \times 2\pi(1 - \cos(\alpha))$. Moreover, the solid angle of the total sphere in which the photons are emitted is 4π steradians. This yields a modest fraction of collected photons $F = \Omega/4\pi$ = 0.2 %. Moreover, we have installed an interference bandpass filter centered around 254 nm on the path to the CCD camera in order to filter-out potential sources of parasitic light from the useful fluorescence signal, which cuts out 70 % of the fluorescence light at 254 nm.

We can finally estimate the N_{atoms} corresponding to one CCD count thanks to equation 1.5 and for a usual CCD gain of 100 we obtain 0.09 atom per count or 1/0.09 counts per atom.

Chapter 2

A New Laser System for Cooling Mercury Atoms

Cooling neutral mercury atoms requires continuous wave laser light at 254 nm with relatively narrow linewidth (on the order of 10 kHz) and high enough power (on the order of 50 mW to well saturate the atomic transition). What is more, building an optical clock adds to the equation a constraint of robustness and reliability, for continuous operation over several hours, days or even months! I will describe in this chapter the technical solutions that I have found to meet these challenging requirements.

Historically, the development of SYRTE's mercury optical lattice clock has been hampered by recurrent problems with the cooling laser system. Prior to the beginning of this thesis, before commercial high-power and narrow linewidth Ytterbium-Doped Fiber-Amplifier (YDFA) technology was available, the cooling light was produced by a frequency quadrupled thin disk laser[1]. This laser was very difficult to operate, with a warm-up time of several hours and frequent mode hops, which prompted us to think about a better solution.

During the course of this thesis, I designed a laser architecture based on newly available commercial YDFA technology and two systems were built for cooling mercury ^{199}Hg atoms on the $^1S_0 \rightarrow {}^3P_1$ transition. One of these systems is used to power the 3D-MOT (see Section 1.2), while the second will be used to power the 2D-MOT, and it is frequency locked onto the first one (see Sections 1.2.4 and 2.3.1).

---

[1]Versadisk from ELS

2.1   Requirements

In this section, we study requirements for our cooling light system in order to efficiently cool down mercury atoms in a magneto-optical trap and perform atom counting by fluorescence detection. From these prerequisites, we will draw a set of specifications, which we will use to design a suitable architecture for our purpose.

2.1.1   Spectral purity

As seen in the Introduction, the linewidth of the cooling transition is about 1.3 MHz. Therefore, to cool efficiently the atoms (down to the Doppler temperature of 30 μK), we have to build a laser system in the UV at 254 nm, with a linewidth narrow with respect to 1.3 MHz. If we take a factor 10 of margin, we therefore need to build a system with linewidth smaller than 100 kHz in the deep UV.

To our knowledge, no CW laser source with this kind of linewidth is available at 254 nm, and a similar argument applies for a source at 2×254 nm = 508 nm. Consequently, we anticipate that we will start with a laser system working in the infrared (IR) around 1015 nm, which will be doubled twice to reach the desired wavelength.

Taking into account that frequency quadrupling an optical signal increases the linewidth (assuming that said linewidth is limited by white phase noise) by a factor 16, we conclude that we need a linewidth of the original IR laser below 6 kHz, which sets a significant technical constraint.

2.1.2   Laser power

The power requirements for cooling neutral atoms is usually set with respect to the saturation intensity [69]

$$I_{sat} = \frac{2\pi^2 hc\Gamma}{3\lambda^3}. \tag{2.1}$$

For mercury, the value of this parameter is 102 W/m^2. Since we have 3 MOT arms, we would ideally want $I \simeq I_{sat}$ for each of the MOT arms, we would therefore need to have $I_{tot} \simeq 306$ W/m^2. Assuming a beam area of 1 cm^2, we therefore need more than 30 mW of total laser power at 254 nm, reliably on a time scale of several hours to several days. We expect that more than 50 mW should be reachable with our setup.

2.2   Architecture of the Cooling Laser

Taking into account the specifications established above, I have devised the architecture presented on Figure 2.1. The laser light is generated by a home-built external cavity diode laser (ECDL) in the IR at 1015 nm, providing a narrow spectrum before quadrupling.
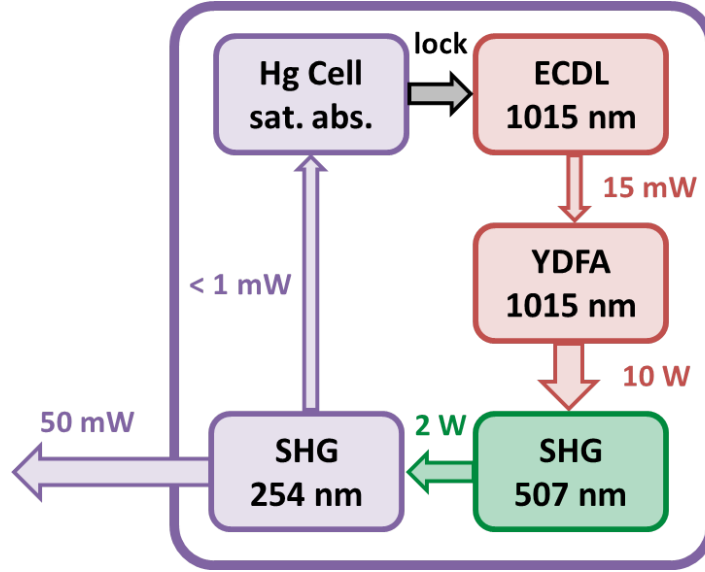
Figure 2.1. *Overall cooling laser architecture. The narrow linewidth ECDL at 1015 nm is amplified in an YDFA, and frequency doubled twice to 254 nm. The light at 254 nm is locked to the cooling transition via saturated absorption spectroscopy in a Hg cell (see text for more details).*

The light from this laser is injected into a Ytterbium doped fiber amplifier (YDFA), which allows us to get high enough power before frequency quadrupling while keeping the narrow linewidth properties of the ECDL.

The amplified light is then frequency doubled to 507 nm in a single pass configuration with a Periodically Poled Stoichiometric Lithium Tantalate (PPsLT) crystal, and subsequently doubled in a resonant doubling cavity containing a β-Barium Borate (BBO) crystal.

2.2.1   External-Cavity Diode Laser

The first stage of the system is designed to have a narrow linewidth of at most a few kHz, tunable frequency output and a high enough power to feed the subsequent amplifier. It is a home-built ECDL

mounted in Littrow configuration (recoupling of the 1st diffracted or-
der from the grating into the diode) that I designed and assembled at
the beginning of my PhD. A scheme of the ECDL can be seen on figure
2.2.

Figure 2.2. *Scheme of the ECDL seed laser for the cooling laser system. The home-
made aluminum enclosure is shown in blue. TEC: temperature controller, HV: high-
voltage, PZT: piezo-electric transducer.*

External-cavity diode lasers offer high frequency tunability over dif-
ferent ranges: coarse tunability on the nm scale with the grating angle
thanks to the spectral dispersion of the reflected light on the grating,
finer tunability by mounting the grating on a Piezo-Electric Transducer
(PZT), on the hundreds of MHz scale, with up to a few kHz bandwidth,
and finally fast tunability by reacting weakly on the current for high-
bandwidth locking of the laser. This makes it a very versatile and
tunable laser, with narrow linewidth, ideal as a seeder, provided we
can keep it single frequency [90].

Since we need a linewidth below 6 kHz, we have chosen a long
extended cavity architecture, with a distance between the diode chip
(TOPTICA single-frequency diode laser, specified linewidth ≥ 1 MHz)
and the grating (Edmund Optics) of 12 cm used in Littrow configura-
tion.

With such a long cavity, I needed to make sure that the seeder
would keep a single mode behavior over a wide enough range of fre-
quencies (several GHz ideally). To that end, the laser diode is mounted
with thermal glue on a copper piece and glued to a Peltier element

Figure 2.3. *Picture of the homemade ECDL seeder for the cooling laser system. The diode and the grating can be seen in the aluminum enclosure on the left of the picture. On the right, the setup for frequency-locking of the 2 seeds is visible, see Section 2.3.1 for more details.*

for active temperature stabilization and frequency tuning. The optical setup (diode plus grating) is contained in an aluminum enclosure (also home-built) which can also be temperature stabilized if needed. Care was taken to avoid mechanical resonances, by putting the grating on a brass piece, and by setting the whole aluminum enclosure on spring washers. Finally, I put the breadboard containing the aluminum box (see Figure 2.3) in yet another box that I assembled with aluminum profiles and PVC foam, and mounted on sorbothane pads for further vibration isolation from the rest of the environment.

The seed laser outputs close to 15 mW of light at 1015 nm, and by beating it with the previous cooling laser system (Versadisk), we have verified that its linewidth is below 1 kHz on short timescales.

2.2.2   Laser amplifier and single stage doubling to 507 nm

For amplification of the 1015 nm light prior to frequency doubling, I have designed and tested in a proof of principle setup a YDFA sys-

tem which was then manufactured in collaboration with an industrial partner[2].

The YDFA consists of two stages of optical amplification in a fiber gain-medium doped with Ytterbium (Yb^{3+}), pumped with light from diode lasers at 976 nm co-propagating with the seeder signal to be amplified.

The 2-stages amplifier yields an overall gain of 28 dB (from 15 mW to 10 W). Experimentally, I had to find a trade-off between a long active (Yb-doped) fiber of the amplifier, yielding a higher gain, and a low enough amount of ASE (Amplified Spontaneous Emission), performing successive fiber cutbacks while monitoring the output power and ASE spectrum.

Several stages of optical isolation have been installed in the final manufactured product to reduce the risk of damage to the pumps or the seeder, which might occur due to Q-switching in the fiber amplifier. In spite of these precautions, the amplifier had to be shipped back to the manufacturer several times during the course of the PhD because of damages to the fiber gain medium.

The resulting 10 W of 1015 nm light are focused onto a oven-stabilized PPsLT crystal for frequency doubling to 507 nm. The fundamental pump signal at ω is separated from the frequency doubled signal at 2ω by a dichroïc mirror and damped into a beam-dump. The overall architecture of the YDFA system is shown on figure 2.4.

Thanks to the fibered technology, this system necessitates almost no warm-up time, and can operate reliably for several months, after which we have found that the seed laser usually acquires a slightly multimode behavior and the recoupling into the diode needs to be adjusted via realignment of the grating.

Furthermore, it can be installed in a dedicated rack, freeing precious real-estate on the main optical table.

2.2.3   Frequency doubling to 254 nm

The final step of our cooling laser apparatus is frequency doubling to 254 nm to couple to the $^1S_0 \rightarrow {}^3P_1$ cooling transition.

For this, we use resonant doubling in a cavity in a BBO crystal. BBO was chosen for its high doubling conversion efficiency, trans-

---

[2]ALS, Talence
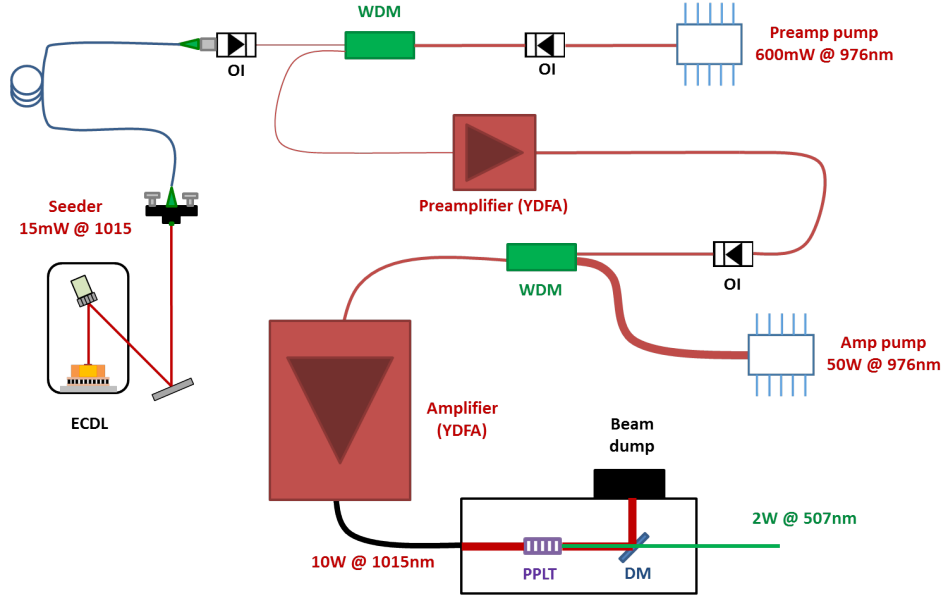
Figure 2.4. *Scheme of the two-stage Ytterbium fiber amplifier for amplification of the seed power to 10W and subsequent single-stage frequency doubling. ECDL: external-cavity diode laser, OI: optical isolator, WDM: wavelength division multiplexing, PPLT: Periodically Poled Stoichiometric Lithium Tantalate, DM: dichroic mirror.*

parency in the deep UV, and more importantly because it has a high damage threshold and durability in the UV, which are absolutely crucial features for our application. The cavity is realized in a bow-tie configuration, with a total length of 84.2 cm and a waist at the position of the crystal of 30 μm. The finesse is approximately 220.

A sidelock scheme is used to lock the cavity (reacting on one of the flat mirrors of the cavity glued to a piezo-elctric transducer) to the side of the optical resonance with a tunable offset which allows us to easily adjust the UV power sent to laser-cool the atoms. One of the drawback is that the sidelock scheme is intrinsically asymmetric (we lock to one side of the fringe), which creates and asymmetric spectrum of the generated UV light at the output of the cavity. However, since the cooling laser has been designed to have a linewidth much smaller than the decay rate of the cooling transition, we don't expect this to be an issue for the atomic cooling efficiency. Figure 2.5 (a) shows a plot of the optical power output from the doubling cavity at 254 nm as a function of the offset of the cavity sidelock. From an input 2 W of light at 507 nm, we get a peaked signal on the locking photodiode of the cavity of 2.5 V. If we take the graph of Figure 2.5 (a), fit it with a linear
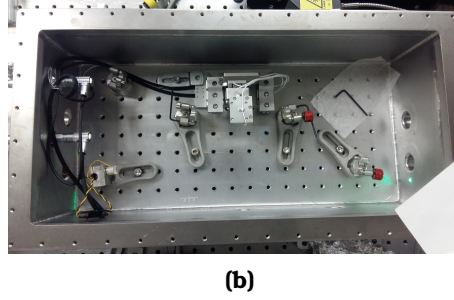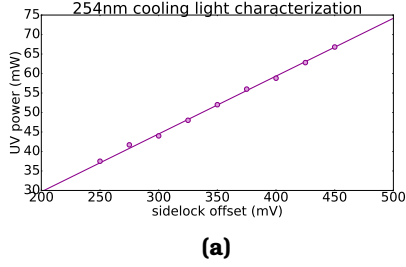
Figure 2.5. *(a) Characterization of the UV power at 254 nm from the doubling cavity as a function of the offset of the cavity sidelock and (b) Picture of the new 254 doubling cavity with the crystal positioner visible in the center.*

model and extrapolate to this value, we estimate that locking at 2.5 V on the sidelock would yield 370 mW of light at 254 nm, but at the risk of damaging the doubling crystal and UV optics in a matter of minutes. We therefore operate with a more reasonable sidelock offset between 300 and 350 mV, giving a usable $\simeq$ 50 mW of UV light, fulfilling the requirements set in Section 2.1.

Moreover, it has been empirically observed that operating in a pure oxygen environment reduces the risks of UV-damage to the BBO crystal as well as the optics of the doubling cavity. A airtight aluminum enclosure hooked to a medical-grade oxygen bottle has therefore been designed during the PhD thesis of R. Tyumenev and surrounds the cavity with a well-controlled quasi-pure O_2 environment. In the course of my PhD, this design has been improved to include a new crystal holder and positioner which can be controlled without having to open the aluminum enclosure, which was a source of contamination of the crystal environment in the previous system. The new doubling cavity is shown on Figure 2.5 (b).

2.2.4   Locking to the cooling transition via saturated-absorption spectroscopy

In order to tune the laser at a tunable frequency offset from the cooling transition, it needs to be offset-locked to the resonance via saturated absorption spectroscopy. Saturated-absorption is a technique used to obtain narrow-line optical lineshapes for locking or spectroscopy, free of 1st order Doppler effects.

A strong pump beam (with wave-vector $\overrightarrow{k_l}$) is sent through a thermal gas of atoms and saturates the transition of interest. Let us consider the particular case where this beam is slightly detuned with respect to the atomic resonance by a quantity $\delta = \nu - \nu_0$ where ν is the laser beam frequency and ν_0 the atomic transition frequency. Then atoms with a velocity $\vec{v}$ such that

$$\overrightarrow{k_l} \cdot \vec{v} = \delta \tag{2.2}$$

will be pumped to the excited state, thus creating a hole in the ground-state velocity distribution centered around $\vec{v}$.

If now a second laser beam with the same frequency but opposite propagation direction (with wave-vector $-\overrightarrow{k_l}$) interacts with the atoms, equation 2.2 becomes

$$(-\overrightarrow{k_l}) \cdot (-\vec{v}) = \delta \tag{2.3}$$

We see that in order to satisfy equation 2.3, atoms with a velocity $-\vec{v}$ will be pumped to the excited state, creating another hole in the atomic velocity distribution centered around $-\vec{v}$.

If the 2 counter-propagating laser beams are now at resonance with the atoms ($\delta = 0$), then the only way to satisfy both equation 2.2 and equation 2.3 is that both laser beams interact with atoms for which $\vec{v} = 0$, creating an absorption feature in the velocity distribution which is the sum of the contribution from both laser beams centered around $\vec{v} = 0$ and therefore free of 1st order Doppler effects (further details on saturated-absorption locking can be found in [92]).

Picture 2.6 (a) shows the overall locking setup of the cooling system. AOM1 is used to dynamically control the detuning of the light going to the Magneto-Optical Trap for the capture and compression phases, as discussed in Section 1.2.2. It works around 180 MHz, with a digitally tunable detuning Δ which varies between -1.5 Γ and -5.5 Γ. The detuned light is then sent to AOM2, which is also centered around 180 MHz and used to generate a modulation at 300 kHz for frequency-modulation locking of the ECDL to the Doppler-free saturated-absorption feature shown in blue on Figure 2.6 (b).

(a)

(b)
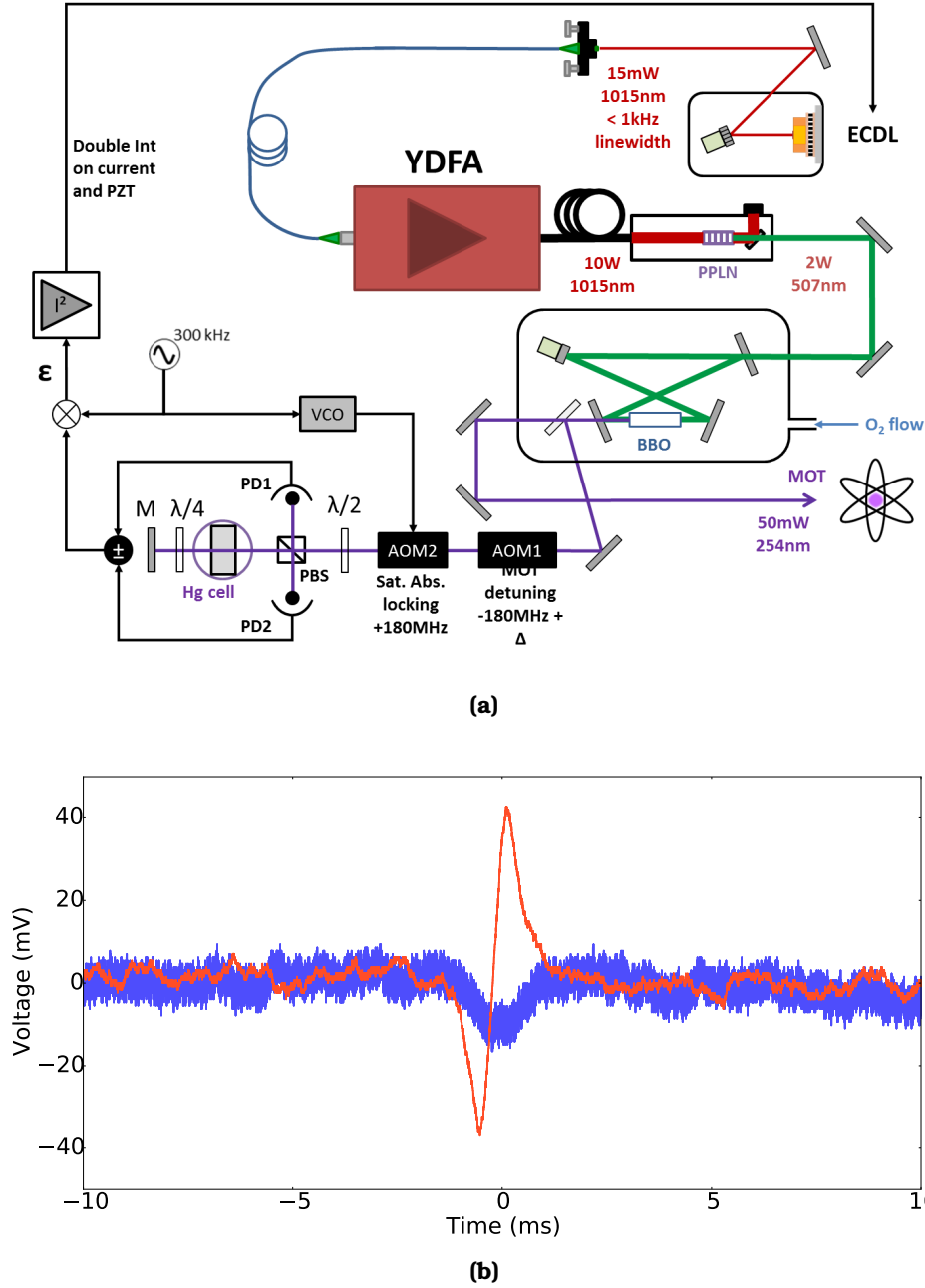
Figure 2.6. *(a) Scheme of the locking to the cooling transition via saturated absorption spectroscopy. and (b) Experimental signals. The blue trace is the Doppler-free saturated-absorption signal, and the red trace is the dispersive error signal generated by the modulation of the beam with AOM2. Both signals are observed by scanning the frequency of the laser across the atomic resonance.*

In order to generate this signal, the modulated light is sent through a 1-mm-long quartz cell containing Hg vapor at $\simeq 0.25$ Pa at room temperature surrounded by a magnetic field to resolve the fine structure of the $^3P_1$ level. The beam incoming on the cell is split by a PBS, and the reflected part is sent to a photodiode (PD1 on the scheme) to act as a reference signal for background noise suppression.

The transmitted beam goes once through the cell, is retro-reflected on mirror M, and goes through the cell again to generate the saturated absorption signal on photodiode PD2. Its polarization is controlled by a quarter wave-plate which is tuned experimentally to balance the two photodiodes and maximize the signal to noise ratio of the Doppler-free feature. The subtracted signal from the photodiodes is then mixed with the 300 kHz modulation and serves as the error signal for the lock (red curve of Figure 2.6 (b)).

As can be seen on Figure 2.6 (a), in order to lock the laser to the Hg signal, we use a double integrator to feedback onto both the current and the PZT of the grating of the ECDL. The current allows high-bandwidth locking, and the PZT increases the capture range of the lock.

2.3   A Second System for the 2D-MOT

The second system which we will use to run the 2D-MOT is an almost exact copy of the first one (including the ECDL seed laser), except for the slightly higher laser power (2 W instead of 1.5 W at 507 nm).

This laser doesn't need to be tuned in frequency, since the 2D-MOT works at a fixed detuning from the cooling transition, chosen experimentally to maximize the loading rate into the 3D-MOT. Therefore, we have decided to implement a simple offset frequency lock between the two seed lasers with a feed-forwarding system to keep the 2D-MOT laser at a fixed detuning from the cooling transition while moving the detuning of the 3D-MOT system for MOT compression as discussed in Chapter 1.

2.3.1   Frequency locking of the two seed lasers for 2D-MOT operation

Since optical coherence between the two lasers is not a requirement, we can devise a simple scheme to lock the 2D-MOT cooling laser to the atomic transition by frequency locking it to the 3D-MOT laser. The frequency lock between the two seed lasers follows the scheme of Figure 2.7.

Seed 1 is locked to the atomic transition via saturated absorption spectroscopy as described in section 2.2.3. An AOM is inserted after the second seed, to generate on the photodiode (PD) a heterodyne beatnote around 180 MHz between the two ECDLs. This beatnote is fed into a frequency to voltage converter (F to U), which delivers a voltage proportional to the frequency of the input signal. We then subtract a voltage offset from this signal to generate the error signal which we correct using a proportional-integrator gain and we feed this back onto the PZT of the second seed laser with a bandwidth of 5 kHz. The details of the locking electronics, that I designed and built during my thesis are shown on Figure 2.8. I have included a few offset inputs, one of which will allow us to tune the frequency of Seed 2 directly with the program that control the rest of the experiment.

Another input is used to feed forward to the Seed 2 the detuning applied to the Seed 1. Indeed, as the frequency of the Seed 1 is modulated during the MOT sequence, as described in Chapter 1.2 from $5.5 \, \Gamma$ to $1.5 \, \Gamma$, this will create a perturbation on the frequency of the 2D-MOT light, since Seed 2 will follow the frequency of Seed 1.

To get rid of this issue, we use a 2nd offset input to be able to realize a feed-forwarding scheme, which we will use to null the effect of the detuning of Seed 1.
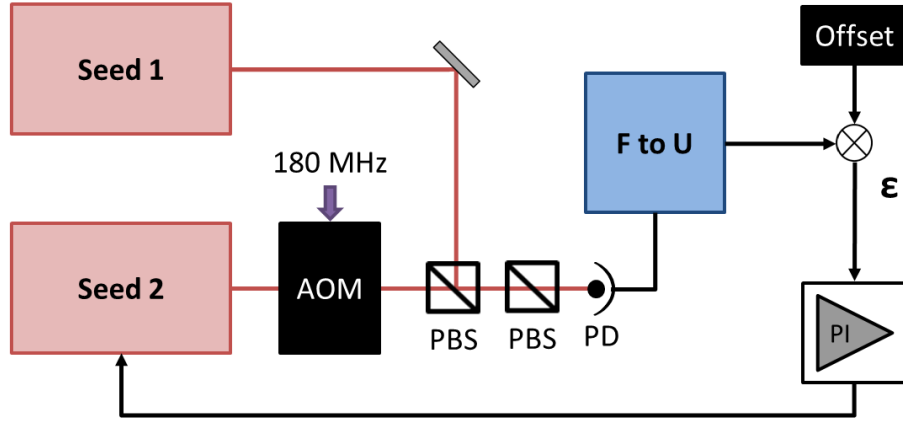
Figure 2.7. *Scheme of the frequency lock between the two seeds. The AOM is used to create a heterodyne beat between the two lasers on a photodiode. The frequency difference between the seeds is converted into a voltage by a frequency to voltage converter and compared to a reference, tunable offset which defines the lock point. PD: PhotoDiode, PBS: Polarizing Beam-Splitter, F to U: frequency to voltage converter, ε: error signal, PI: Proportional-Integral.*
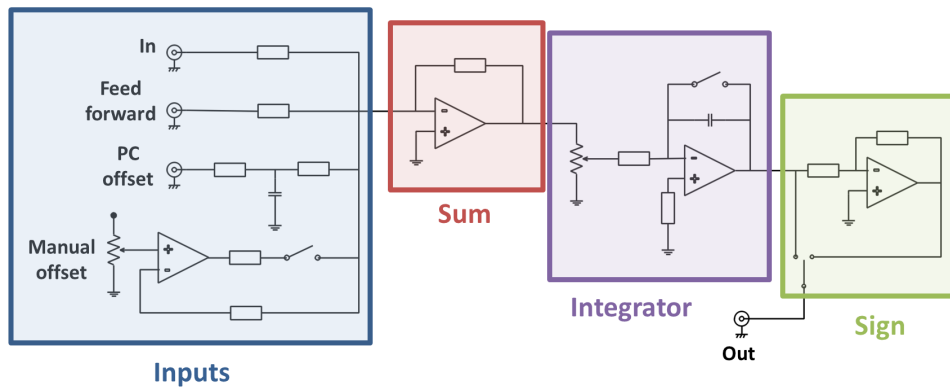
Figure 2.8. *Controller electronics scheme of the frequency lock between the two seeds.*

Chapter 3

High-Resolution Spectroscopy in an Optical Lattice Trap

In this chapter, we consider the coherent interrogation of our sample of cold atoms by the ultrastable clock laser. Scanning the frequency of the laser, we are able to resolve the strongly forbidden clock transition, which will provide the frequency discriminator for our clock. We will see that, using a weak probe laser well aligned with the optical lattice, we are able to probe the carrier transition free of any motional effects. In this configuration, we have recorded very high resolution spectra, and demonstrated the coherent manipulation of the internal quantum states of the atoms for probing times as long as several hundreds of milliseconds.

However, the effects of atomic motion in the lattice trap still need to be taken into account, as they can be a very serious issue for clock accuracy, creating motion-dependent lattice-related light-shifts and excitation inhomogeneities. Information on atomic motion and temperature can be extracted from clock spectroscopy by looking at the sideband structure around the motion-less carrier transition. In lattice clock experiments, longitudinal sidebands are usually probed using a high-power (enough to strongly saturate the carrier transition) probe beam, and fitted to obtain an accurate measurement of the lattice trap depth, as well as atomic temperature [6]. However, in our experiment, the lack of power in the UV prevents us from using this technique as

a diagnostic tool. However, if we introduce an angle between the probe and the lattice, transverse motional sidebands will be coupled to our interrogation laser even for relatively weak probe powers. We will use this fact to our advantage and extract useful information about the trapping potential from the frequency of the transverse sidebands.

To check the consistency of these information, we have also studied the effect of parametric heating of the atoms out of the lattice trap. We will see that this technique provides physical insight into the physics of the atoms in the trap, giving complementary information with respect to sideband spectroscopy.

3.1   Theory: Spectroscopy in a 1D Optical Lattice

In this first section, we introduce the basic concepts and parameters of the physics of the interrogation of neutral atoms trapped in an optical lattice, which is needed to interpret the experimental spectroscopic curves of Section 3.2.

3.1.1   Clock spectroscopy in the Lamb-Dicke regime

High-resolution spectroscopy of neutral atoms in a magic optical lattice trap has been the subject of intense research in the past ten years [6], drawing inspiration from spectroscopy of tightly trapped ions [116]. The lattice trap is mainly characterized by its depth, which is usually expressed in units of the lattice recoil energy E_{rec}, as mentioned in the Introduction (see Equation 12).

The potential experienced by the atoms close to the waist of the lattice build-up cavity can be written:

$$U(r, z) = U_0 \left(1 - e^{\frac{-r^2}{2w(z)}} \right) \times \cos \kappa z^2 + mgz \qquad (3.1)$$

where z is the coordinate along the axis of the lattice, $r = \sqrt{x^2 + y^2}$ is the radial coordinate, $w(z)$ is the lattice beam radius at the position z, g is the gravitational acceleration (g = 9.81 m/s^2) and U_0 is the trap depth.

We can expand this potential around the antinodes of the lattice, where the atoms are trapped, because at the high lattice depths explored in our work ($U_0 \ll 20$), tunneling between lattice sites is negligible and we can therefore neglect the effects due to the periodicity of

the optical lattice. The eigenstates of the atomic motion in the trap are those of a harmonic oscillator in the z and r directions with different spring constants which we note in the following $\nu_\parallel$ and $\nu_\perp$ respectively, and which we can relate to the trapping parameters [5]:

$$\nu_\parallel = 2\nu_{rec}\sqrt{\frac{U_0}{h\nu_{rec}}}$$
$$\nu_\perp = \sqrt{\frac{U_0}{m\pi^2 w_0^2}}$$

(3.2)

As we will see in Section 3.3, rewriting Equation 3.2 in a different way will allow us to derive the trap depth from the spectroscopic determination of the transverse sidebands frequency.

We now incorporate to our model the interaction of the probe laser with the harmonically confined atoms. The probe beam waist at the position of the atom is close to 200 μm, while the lattice beam waist is close to 69 μm, we therefore neglect interrogation homogeneities introduced by the gaussian intensity profile of the probe beam. This interaction couples the internal atomic levels with the incident probe laser field modeled as a plane wave, and the effective Rabi frequency characterizing the coupling from state $|n\rangle$ to $|n'\rangle$ is

$$\Omega_{nn'} = \Omega_0 \langle n | e^{ik_{clock} \cdot \hat{x}} | n' \rangle$$

(3.3)

Where k_{clock} is the clock laser k-vector, $\Omega_0 = -d.E\hbar$ is the free-space Rabi frequency describing the atom-light coupling strength, d is the atomic dipole moment and E the electric field strength. Re-writing the position operator $\hat{x}$ in terms of the annihilation and destruction operators, $x = x_0(\hat{a} + \hat{a}\dagger)$, and introducing the parameter $\eta = k_{clock}x_0\sqrt{2}$, we finally can re-write Equation 3.4 as

$$\Omega_{nn'} = \Omega_0 \langle n | e^{i\eta(\hat{a} + \hat{a}\dagger)} | n' \rangle$$

(3.4)

η is called the Lamb-Dicke parameter, and is the appropriate parameter to describe the effect of the external confinement on the atomic spectroscopy [53]. Along the axis i of the trap,

$$\eta_i = k_{clock}^{(i)}\sqrt{\frac{\hbar}{2m\omega_i}} = \sqrt{\frac{\omega_{rec}}{\omega_i}}$$

(3.5)

where $k_{clock}^{(i)}$ is the projection of the clock laser k-vector along the trap axis i (i = x,y or z). Operating in the Lamb-Dicke regime of atomic

confinement ($\eta \ll 1$) suppresses Doppler and recoil effects, which is crucial for high accuracy clock operation. This happens in two cases for a 1D lattice:

- In the transverse direction when the probe k-vector is well aligned on the lattice axis, the projection of k_{clock} along the transverse direction of the lattice is zero ($k_{clock}^{(x)} = k_{clock}^{(y)} = k_{clock}^{(\perp)} \simeq 0$), which means that $\eta_\perp \simeq 0$.

- When probing in the strong confinement axis of the lattice, we can manage to have $\omega_\perp \gg \omega_{rec}$, then we get $\eta_\| \simeq 0$.

In our case, $\nu_{rec}^{probe} \simeq 100$ Hz, and we generally operate with $U_0 \simeq 100\ E_{rec}$, which yields a longitudinal trapping frequency $\nu_\|^{trap} \simeq 100$ kHz in the direction of strong confinement, putting the mercury clock operation deep into the Lamb-Dicke regime. We will see later in this chapter the impact of the probe laser alignment on the spectroscopy curves.

3.1.2 Structure of the clock transition

In order to control the magnetic environment seen by the atoms, we perform spectroscopy in the presence of an external (quasi-) homogeneous magnetic bias field, which also lifts the degeneracy between the $m_F = \pm 1/2$ states. The procedure to verify that the magnetic field is well defined is described in Section 3.2.1 below. By aligning the polarization of the probe beam along the direction of the external field, we are able to selectively excite the so-called π components ($+1/2 \to +1/2$ and $-1/2 \to -1/2$) of the transition, for which $\Delta m_F = 0$, as shown schematically on Figure 3.1. We therefore expect a spectrum featuring two peaks, separated in frequency by $\Delta \nu = 2m_F \delta g_F \mu_B B_z$ where δg_F is the difference between the g-factor of the excited state and the g-factor of the ground state, μ_B is Bohr's magneton in frequency units and B_z is the projection of the bias magnetic field along the polarization of the probe beam.

Lifting the clock states degeneracy also allows us to perform a simple state selection procedure to spin-polarize the atomic sample. At the end of the MOT loading, we start with a sample of atoms in the $^1S_0$ clock ground state with an approximately equal population in both m_F states. We first apply a 15 ms Rabi π pulse resonant with the clock
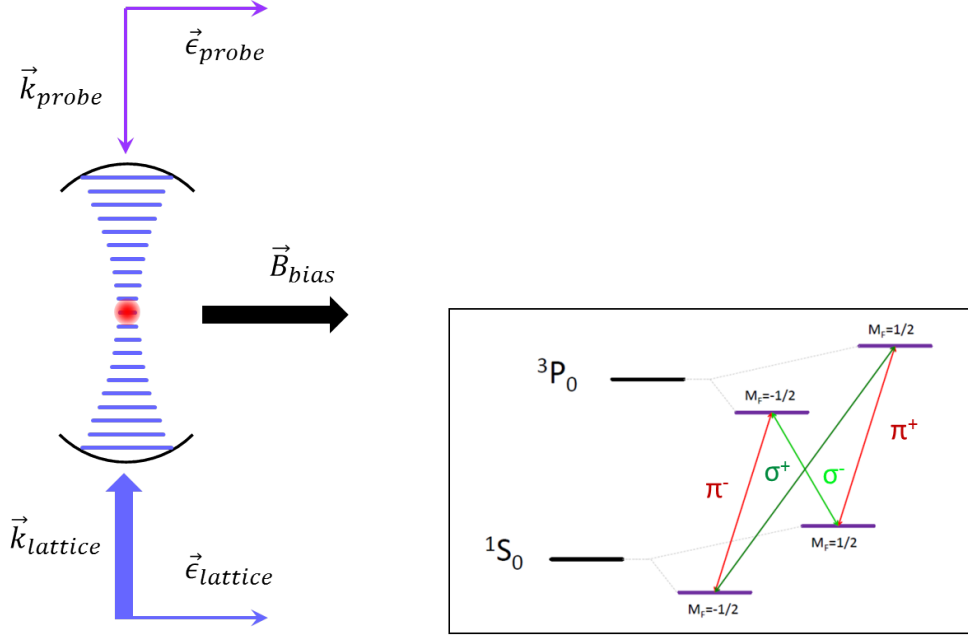
Figure 3.1. *Relative orientation of the lattice and probe wave-vectors, their polarizations and the bias magnetic field. In the current configuration, only the π transitions are excited (red on the right side of the figure).*

transition which transfers up to 80% of the atoms in one m_F state to the excited clock state, leaving the other $(-m_F)$ state atoms in the clock ground state. We then apply resonant light on the $^1S_0 \rightarrow {}^3P_1$, heating and pushing the atoms that are left in the ground state out of the lattice trap, and leaving us with a sample of spin-polarized atoms in the excited clock state. This procedure results in a spin-polarized atomic sample with a state purity exceeding 98% (we verified this by checking that no atoms are detected if we apply only the resonant pulse), with only 50 % atom loss, while being simple to implement and potentially very fast.

Working with a spin-polarized sample is highly desirable for the clock as collisional shifts mechanisms can be suppressed thanks to Pauli's exclusion principle (see Section 5.2). This is only partially true, mainly because motional effects contribute to probing inhomogeneities, which renders the atoms discernable and therefore susceptible to collide again, but it is however a good starting point. Moreover, it allows us to perform spectroscopy on a dark background. Indeed, as described in Section 1.5 we detect the atoms via fluorescence on the

$^1S_0 \rightarrow {}^3P_1$ transition, which is much broader than the Zeeman splitting between the two π components of the clock transition. When operating the clock, we selectively probe one of the Zeeman components, exciting a fraction of the atoms to the $^3P_0$ state which is dark for the fluorescence light. We then want to detect how many atoms have made the transition, by shining detection light onto the atoms that remain on the ground state. However, the atoms from the second Zeeman sublevel have not been excited to the $^3P_0$ state and are therefore still coupled to the detection light, contributing some parasitic fluorescence, and adding significant detection noise to the clock signal.

3.1.3 Rabi and Ramsey spectroscopy

By engineering the sequence of probe pulses sent to the atoms, different spectroscopic experiments can be performed. In clock experiments, two types of spectroscopy are most commonly performed:

- Rabi spectroscopy, where only one pulse of the clock light is applied to transfer atomic population and create the atomic resonance for frequency locking.

  The Rabi transition lineshape as a function of the probe laser detuning ν is given by:

  $$L_{Rabi}(\nu) = A\frac{\Omega_0{}^2}{\Omega^2}\sin^2\left(\frac{\pi\Omega}{2\Omega_0}\right) + B \qquad (3.6)$$

  where Ω_0 is the Rabi frequency, $\Omega = \sqrt{\Omega_0^2 + (2\pi\nu)^2}$. In the case of pure Rabi interrogation of a two level atom by a square pulse, $A = 1$ and $B = 0$. These two parameters are added to the model in an ad hoc way to fit the experimental data and account for experimental imperfection (i.e. residual background, atoms inhomogeneities reducing the contrast of the fringe, etc.). When performing Rabi spectroscopy, we apply a π pulse of the clock light (i.e. which transfers a maximum number of atoms from the initial $^3P_0$ state (see Section 3.1.2) to the $^1S_0$ ground state).

  In the case of Rabi spectroscopy ($A = 1$ and $B = 0$), the linewidth of the obtained spectroscopy curve is roughly

  $$\delta\nu_{Rabi} = 0.8/\tau_\pi \qquad (3.7)$$

where τ_π is the temporal length of the π pulse. However, experimental imperfections and noise sources are susceptible to broaden the line.

From Equation 3.7, we see that longer probe pulses will provide narrower spectra.

- Ramsey spectroscopy, which makes use of a pulse sequence comprising a first $\pi/2$ pulse to create a coherent quantum superposition of the ground and excited states, followed by a free evolution period during which the probe laser is turned off, and its phase and the atomic phase evolve independently. Finally, a second $\pi/2$ pulse is applied to close the atomic interferometer and creates a state superposition which depends on the free evolution period and the probe laser detuning with respect to the atomic resonance.

The Ramsey lineshape as a function of the probe laser detuning ν is given by the equation:

$$L_{Ramsey}(\nu) = A\frac{\Omega_0{}^2}{\Omega^4}\left[\Omega\cos\left(\frac{\omega\tau_{FE}}{2}\right)\sin\left(\frac{\pi\Omega}{2\Omega_0}\right) - 2\omega\sin\left(\frac{\omega\tau_{FE}}{2}\right)\sin^2\left(\frac{\pi\Omega}{4\Omega_0}\right)\right]^2 + B$$
(3.8)

where Ω_0 and Ω are the same quantities as those defined in the case of the Rabi lineshape, $\omega = 2\pi\nu$, and τ_{FE} is the Free-Evolution time. Again, A and B are ad hoc parameters accounting for experimental deviations from the ideal lineshape ($A = 1$ and $B = 0$).

In the case of Ramsey spectroscopy ($A = 1$ and $B = 0$), the linewidth of the obtained spectroscopy curve is

$$\delta\nu_{Ramsey} = 1/(2\tau_{FE})$$
(3.9)

3.2 Experimental Spectroscopic Signals and Their Interpretation

Let us now turn to experimental spectra obtained by scanning the clock laser frequency across the atomic resonance.

3.2.1 Magnetic field zeroing using clock spectroscopy measurements

The first step toward high resolution spectroscopy of the clock transition is to make sure that the magnetic field at the position of the atoms is well defined, and aligned with respect to the probe beam

To that end, we use compensation magnetic coils wrapped around the vacuum chamber to zero the magnetic field at the position of the atoms, and we then apply a well controlled quantization magnetic field with a small bias coil as can be seen on Figure 3.2. To make sure
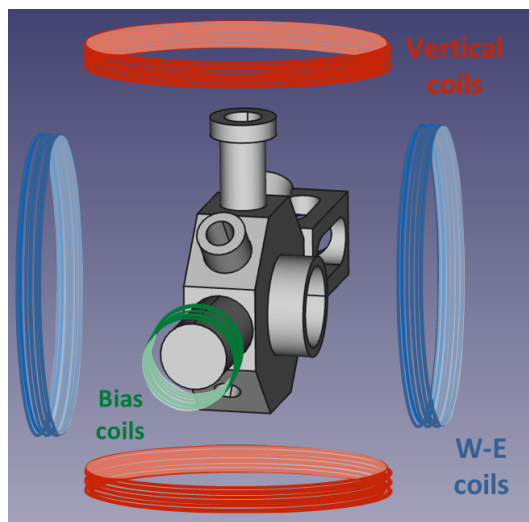
Figure 3.2. *Scheme of the compensation coils around the vacuum chamber. Two sets of coils (blue and red on the scheme) are used for cancellation of stray magnetic fields perpendicular to the quantization axis, which is formed by the Bias coil (green). The vertical direction on the picture is the direction of earth's gravity, which is also the direction of the lattice trapping.*

that the magnetic field coming from the environment is properly compensated, we use the atoms as a magnetometer, by monitoring the splitting of the π Zeeman transitions, and null this splitting by varying the current applied to the compensation coils in the directions of space orthogonal to the bias field. We can see on Figure 3.3 The result of two iterations of this procedure in both direction perpendicular to the bias field. Applying no bias field, if the stray magnetic fields at the position of the atoms are well compensated, we should only see two Zeeman peaks corresponding to the two π transitions, collapsed onto one another, since the splitting (linear part of equation 5.12) is proportional

(a)

(b)
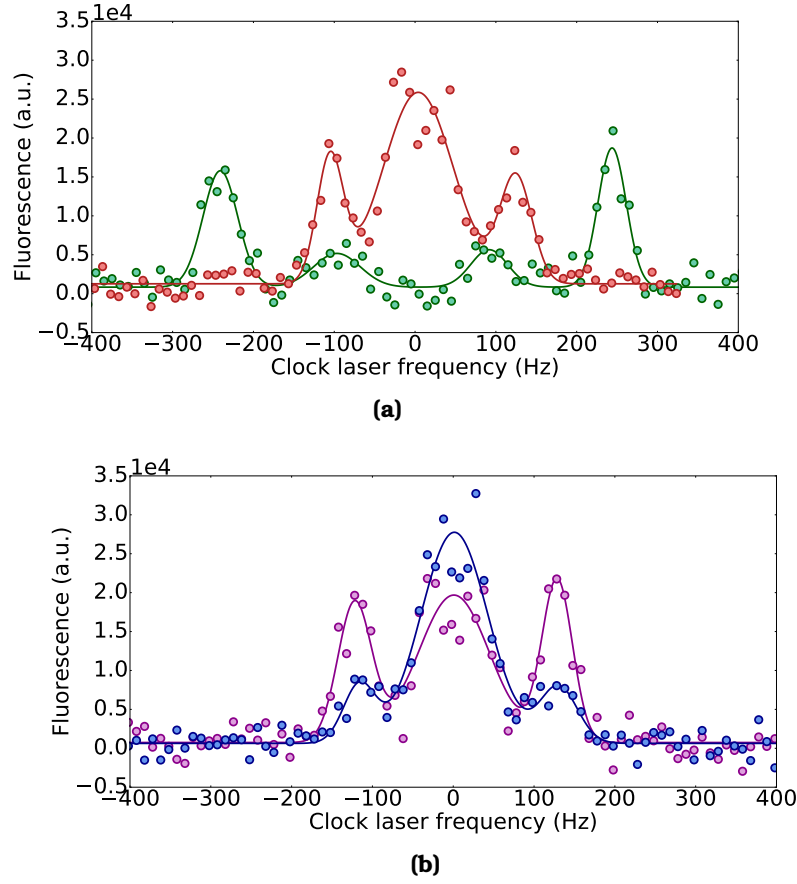
Figure 3.3. *Calibration curves of the environmental magnetic field (a) in the vertical direction and (b) in the West-East direction (the quantization axis is applied in the North-South direction).*

The extra peaks appearing on the spectra are σ transitions which start to appear when the bias magnetic field is no longer well defined and aligned with the polarization of the probe beam.

to the quantization field. However, the violet trace on plot (a) features 4 peaks corresponding to the two π transitions (small peaks in the middle) but also the two σ transitions, meaning that the magnetic field is poorly aligned. By varying the current feed to the compensation coils in the vertical direction, we end up with a spectroscopy looking like the red trace.

We then go on to optimize the West-East direction, applying the same procedure, starting from the blue trace, and we end up with a spectroscopy trace looking like the red one, where the σ components have almost disappeared and the π components are overlapped, meaning that our magnetic field is well aligned, to within the linewidth of

the transitions of 50 Hz on this particular trace.

By performing the operation with narrower linewidth scans (longer clock pulses) and using the first order Zeeman coefficient, we estimate that the magnetic field at the atoms is zeroed to within a resolution of 3 μT in the three directions.

3.2.2   Carrier spectroscopy of the two Zeeman sublevels

Applying the clock sequence depicted on Figure 3.4 (a), we indeed obtain the expected spectrum featuring the two π Zeeman components as discussed in Section 3.1.2. For a typical spectroscopy run with a 15 ms-long probe pulse, the result is shown on Figure 3.4 (b).

(a)

(b)

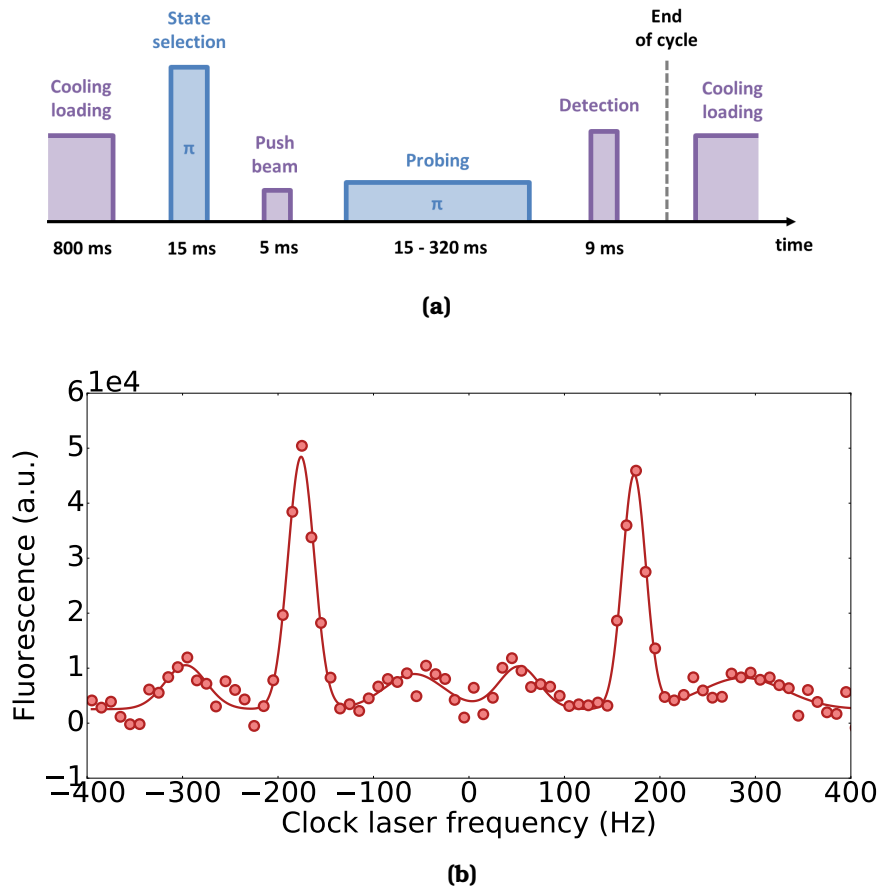**Figure 3.4.** *(a) Clock sequence for spectroscopy without normalization and (b) Spectroscopy on the two π Zeeman components with a 15 ms probe beam. We see two carriers, corresponding to the two Zeeman sublevels $+m_f \to +m_f$ and $-m_f \to -m_f$. The small sidebands visible on each side of the π transitions are residual probing of atomic motion along the transverse confinement (see 3.3.1).*

The Zeeman frequency splitting on this particular curve is 480 Hz, but can be adjusted by varying the strength of the bias magnetic field. The small sidebands on both sides of the π Zeeman components are residual transverse motional sidebands because of imperfect alignment of the probe beam on this particular data run (see Section 3.3.1).

3.2.3 Control of atomic noise: implementing a normalized detection

Transition probability and normalized spectra

The spectra shown in Section 3.2, allow us to lock to the atomic resonance and operate the clock with a stability close to the 10^{-15} level at one second, but they are nevertheless affected by atom number fluctuations. Indeed, from one cycle to the next, the number of loaded atoms into the MOT, and even more so the number of atoms trapped in the lattice can fluctuate, depending on the operating conditions by as much as 20%. If we want to approach the limits of the mercury clock, we have to get rid of these fluctuations.

The obvious way to do that is to apply the interrogation pulse, which will transfer to the ground state a certain fraction of the atoms. These atoms are detected and therefore lost from the trap, yielding a first detected signal that we note P_e. Subsequently, during the same clock cycle, the atoms that have not made the transition to the ground state are then transferred back to the ground state, and detected, yielding a second detected signal P_g. We call transition probability
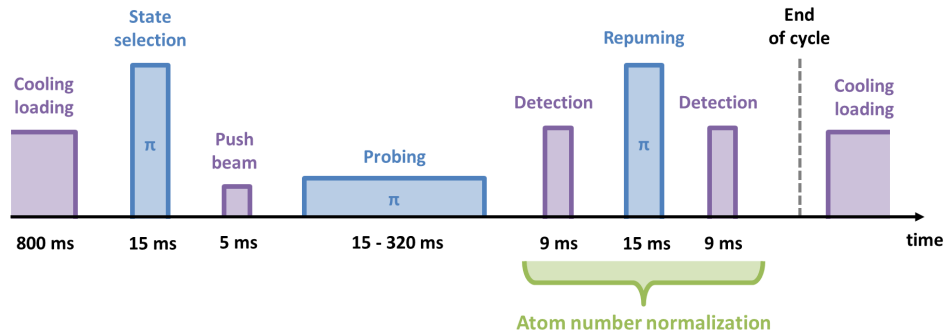
Figure 3.5. *Clock sequence for spectroscopy with normalization. We use a π pulse of the clock light to transfer the atoms back to the ground state and apply another detection pulse in order to obtain the clock transition probability.*

the quantity

$$P = \frac{P_e}{P_e + P_g} \qquad (3.10)$$

This ratio is naturally immune to atom number fluctuations, since these will be equal for P_e and P_g.

Since we do not yet have repumpers to recycle atoms from the $^3P_0$ state back to the ground state via the $^3S_1$ level, we resort to another method, which is to use a short and spectrally broad π pulse of the clock light to transfer the atoms (coherently). The whole sequence including normalization is shown on figure 3.5.

(a)

(b)
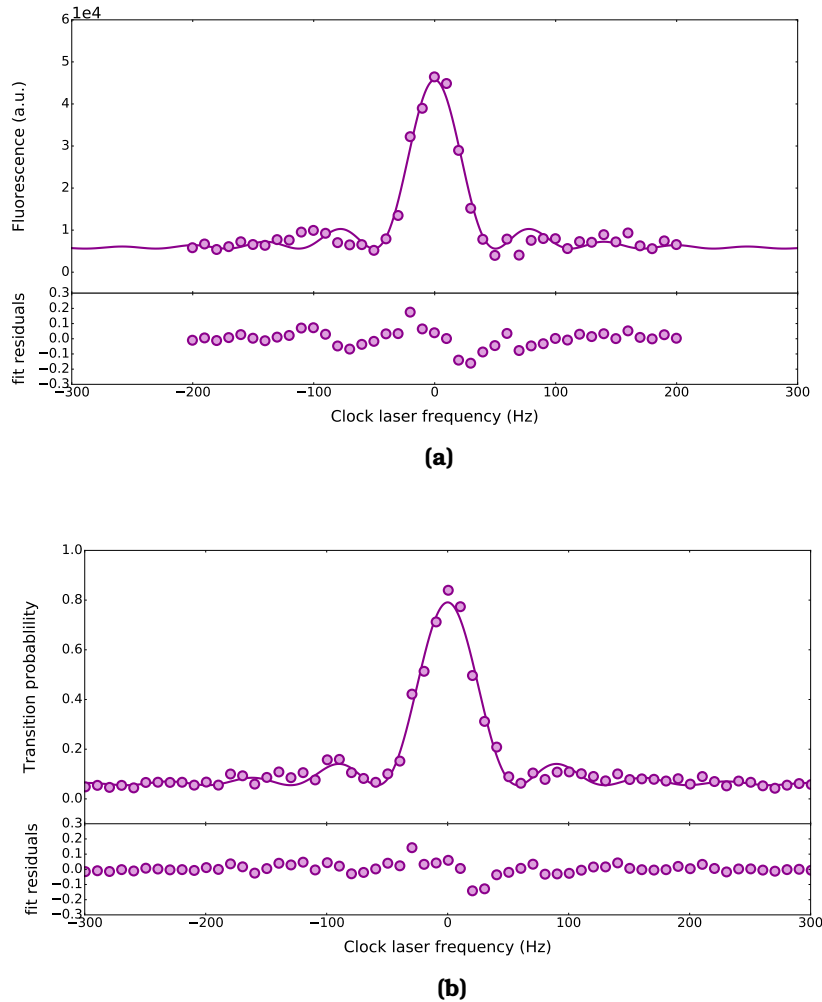
Figure 3.6. *Rabi spectroscopy with 15 ms π pulse (a) without atom number normalization and (b) with atom number normalization. Both curves are an average of 3 realizations of the experiment and are fit with Equation 3.6.*

Figure 3.6 shows the difference on a single 15 ms π pulse spectroscopy between a non-normalized and a normalized signal and taken in otherwise the same experimental conditions. We can see that the signal to noise ratio is improved, and looking at the residuals of both fits (normalized by the amplitude of the spectra to be able to compare them), we see that the normalized spectrum fits better with the expected Rabi lineshape of Equation 3.6.

3.2.4 Towards improved stability: high-resolution Rabi and Ramsey spectroscopy

We have demonstrated that we can use the clock laser to probe the atoms in the lattice in a configuration which is free from cycle-to-cycle atom number fluctuations. However, so far we have only used short pulses of the clock light which give "broad" ($\simeq 50$ Hz) lineshapes. When locking to the atomic resonance to operate a clock, one wants to maximize the slope of the frequency discriminator. To do that, the length of the clock pulses has to be increased, while still keeping a good signal to noise ratio of the atomic signal in order to servo the clock laser to the atomic resonance.
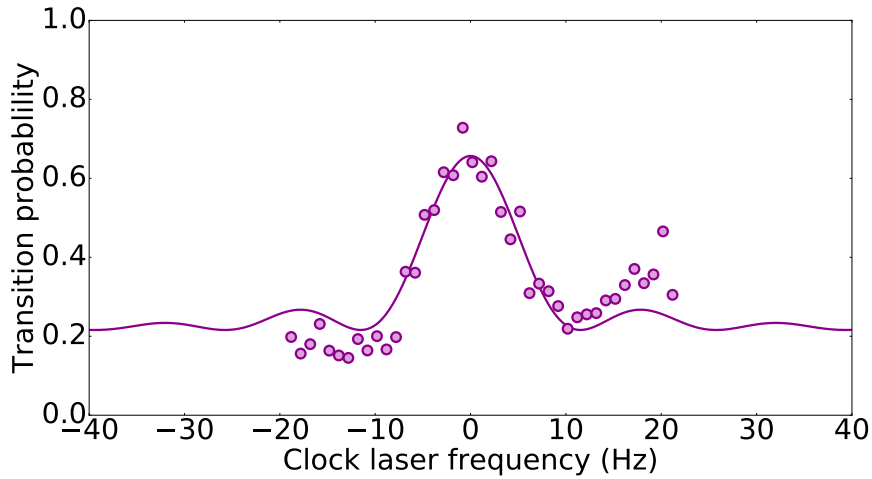
Figure 3.7. *Spectroscopy curve for robust frequency locking using Rabi spectroscopy with 80 ms (π) probe pulse. The fit with eq 3.6 gives the expected 10 Hz Fourier limited FWHM resonance.*

We have found that a good trade-off, using clock instability as a criterion (see Chapter 4 for more details) is obtained for probe pulses

of 80 ms, corresponding to a transition linewidth of 10 Hz. A spectroscopy curve taken in this configuration is shown on Figure 3.7.

Using a slightly more complicated pulse sequence, we can also perform Ramsey spectroscopy. In that case, as described in Section 3.1.3, the laser creates a coherent clock states superposition, after which the laser phase and the atomic phase are left free to evolve independently for a variable amount of time, and are finally recombined, creating a fringe pattern as a function of the clock laser detuning with respect to the atomic resonance which is shown on Figure 3.8. In that case when comparing with Figure 3.7 for which the interrogation time was 80 ms, 50 ms of free-evolution time yield the same central fringe width of 10 Hz, illustrating the favorable scaling of the transition linewidth for Ramsey free evolution time (Equation 3.9) versus Rabi time (Equation 3.7). Here we have used $\pi/2$ pulses of 7.5 ms to create the quantum superposition of the clock levels and to close the atomic interferometer. The favorable scaling of the transition linewidth seems to indicate that Ramsey interrogation is more beneficial for clock operation. However, the clock noise scales differently as a function of Fourier frequency for Rabi and Ramsey interrogation, and with our clocks duty cycle, we expect that it is still favorable (and simpler given our signal to noise ratio) to use the clock performing Rabi interrogation, and in the rest of the thesis all experiments are done using Rabi spectroscopy.

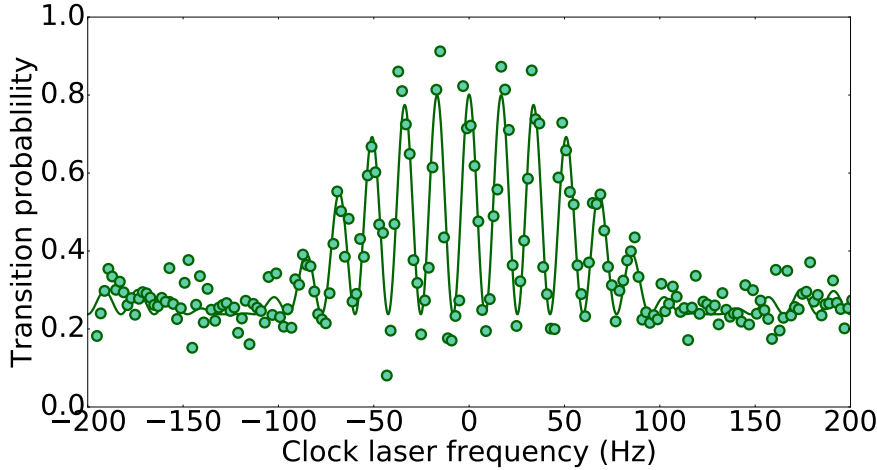**Figure 3.8.** *Spectroscopy curves for robust frequency locking using Ramsey spectroscopy with 7.5 ms ($\pi/2$) pulses and 50 ms free evolution time. The fit with eq 3.8 gives a 10 Hz full-width at half maximum (FWHM) central fringe as expected.*

Using clock spectroscopy, we can look for the limits in atom/probe coherence by increasing the length of the interrogation pulses, adjusting the power to still apply a π pulse to the atoms, and see how narrow we can make the clock transition lineshape. In order to perform these narrow spectra, the probe laser frequency drift must be thoroughly compensated since slow laser frequency excursions can create an (asymmetric) line broadening.

We expect that when increasing the interrogation time, several mechanisms can create line broadenings, such as loss of atom-laser coherence, density-related broadening and scattering of lattice photons.

As it turns out, the current status of the experiment doesn't allow us to probe these effects. Indeed, the limitation to the interrogation time does not come from a loss of coherence, but rather from a loss of atoms from the lattice, because of the limited atomic lifetime of $\simeq$ 300 ms in the trap, which degrades the signal to noise ratio of the spectroscopy for long interrogation pulses.

Indeed, we see on Figure 3.9 that increasing the Rabi pulse length by a factor of two to 160 ms, and another time up to a 320 ms long pulse, we keep a nice Fourier-limited lineshape, which testifies to the fact that atom laser coherence is still preserved at these long interrogation times. We observe however an increasingly degraded signal to noise ratio, mainly because of atoms loss from the lattice, presumably due to background gas collisions. In order to resolve narrower spectra, an increase in the lifetime of the atoms in the lattice trap will be needed, probably by improving the vacuum conditions. Nevertheless, using a 320 ms long pulse, we have been able to resolve a record (in the history of the mercury clock) transition linewidth of 2.5 Hz. The plot is shown on Figure 3.9 (b)). At the carrier frequency of 1.128 PHz, this corresponds to an atomic quality factor Q_{at} = 4.5 $\times$ 10^{14} in the deep UV.
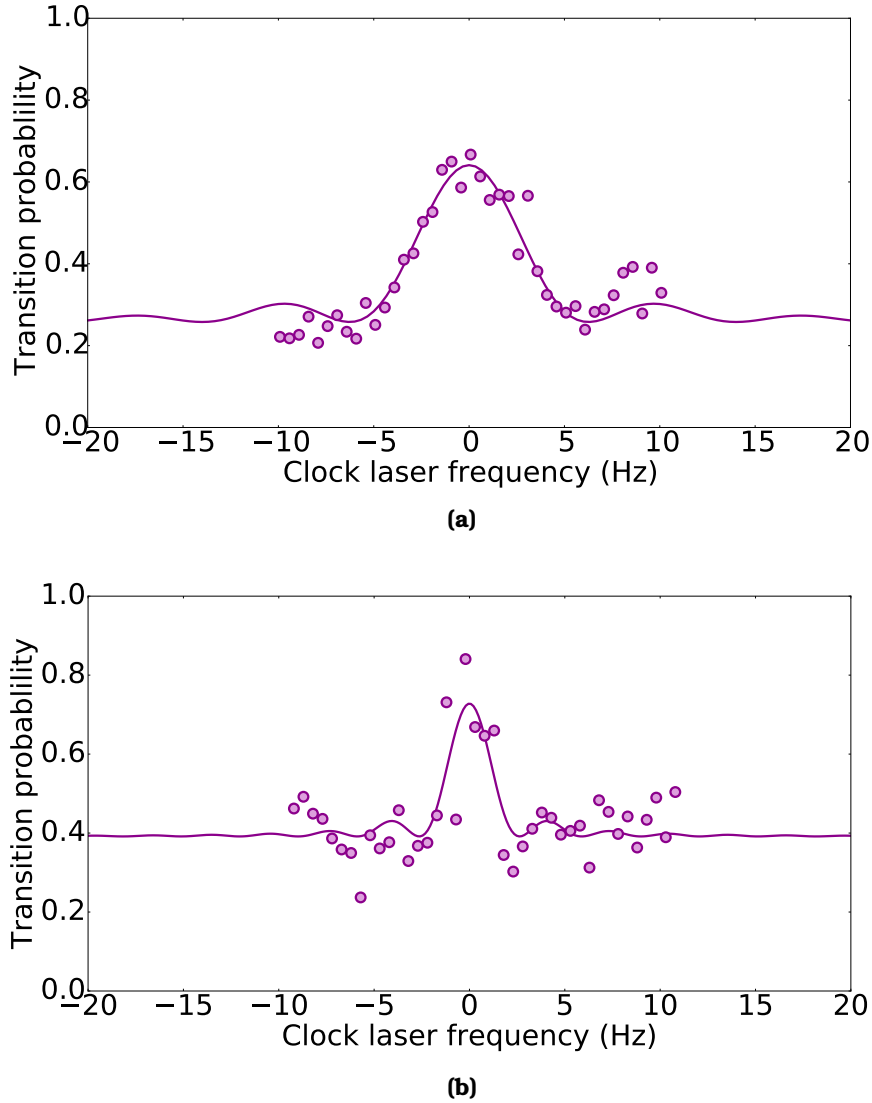
Figure 3.9. *Spectroscopy curves for long clock pulses (a) Rabi spectroscopy with 160 ms (π) probe pulse. The fit with eq 3.6 gives a FWHM of 4.6 Hz, close to the expected 5 Hz Fourier limited resonance. (b) Rabi spectroscopy with 320 ms (π) probe pulse. The fit with eq 3.6 gives the expected 2.5 Hz Fourier limited FWHM resonance.*

3.2.5   Rabi flopping and excitation inhomogeneities

Another way to characterize atom/probe coupling is to perform a Rabi flopping experiment. The clock laser is set at resonance with the $^1S_0 \rightarrow {}^3P_0$ and the area of the probe pulse is varied, either by varying the pulse length at constant power, or varying the probe power while keeping the Rabi time constant. Experimentally, by applying a probe pulse of variable duration and constant power, we observe a damped oscillation of the atomic populations between the ground and the excited state as a function of increasing pulse area. The damping yields information on the relative coupling of the probe laser and the atoms.

Such Rabi flopping curves have been observed on our experiment for the first time during the course of my PhD work, an improvement which was made possible by the implementation of the normalized detection and the improved reliability of the whole laser systems.
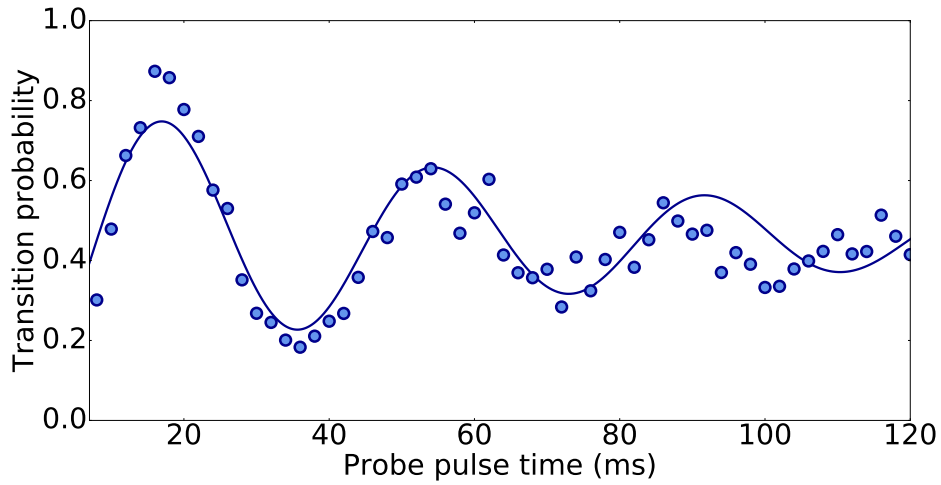
Figure 3.10. *Transition probability as a function of probe time for a given probe power. For this particular run, a clock π pulse corresponds to 18 ms.*

On Figure 3.10, I plot the transition probability for the -1/2 → -1/2 Zeeman component as a function of the probe pulse duration. The experimental data are fitted with a damped sinusoidal, yielding a Rabi frequency of $\Omega = 2\pi \times 27$ Hz, a contrast of 0.45 and a characteristic decay time of the oscillation $\gamma = 75$ ms. The damping of the oscillations is most certainly due to excitation inhomogeneities across the atomic sample. On our experiment, the atoms are not cooled inside

the lattice (e.g. via sideband cooling), which means that they populate several motionally excited states, leading to different atoms having different Rabi frequencies (see Section 3.1 for more details), leading to a dephasing of the Rabi oscillation. Hints of experimental evidence of behavior can be seen on the plot of Figure 3.17 where we perform Rabi oscillation experiments on atomic samples with different temperature distribution, see Section 3.4.2.

The period of the oscillating signal allows us to calibrate and engineer the probe pulse (power and length) to reach any desired atomic transition probability.

3.3 Estimation of the Trap Depth with Transverse Sideband Spectroscopy

3.3.1 Spectroscopy with a misaligned probe beam

All the curves shown above have been obtained by carefully overlapping the probe beam on the lattice, to ensure that we are probing the atoms in the direction of strong confinement of the trap. We estimate based on the geometry of the experiment, the alignment procedure (overlapping both beams before and after the lattice cavity) and the size of the beams that we can get the alignment correct to within $\simeq 10$ mrad. However, if we intentionally misalign the probe beam, we should see some sidebands appearing on either side of the carrier transition, which will reveal information about the transverse atomic motion in the quasi-harmonic confinement.

Indeed, figure 3.11 shows such a scan with a misalignment angle estimated to be $\simeq 20$ mrad. We can see clearly two narrow carriers, corresponding to both π transitions, as well as motional sidebands appearing on each sides (red and blue) of both carriers. Due to the weak power of our probe beam, and the very small coupling, only the first order sidebands, corresponding to the transition $|e; n_{trans}\rangle \to |e; n_{trans}+1\rangle$ (blue-shifted sideband) and $|e; n_{trans}\rangle \to |e; n_{trans}-1\rangle$ (red-shifted sideband) are visible on the plot.
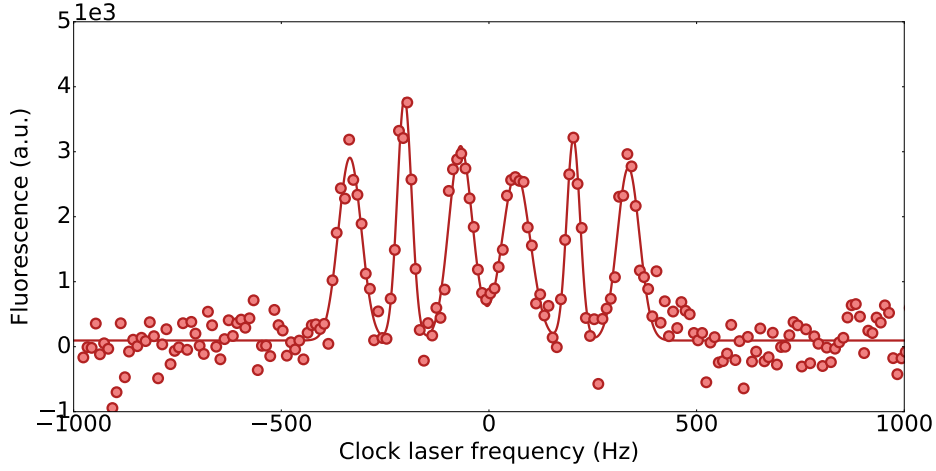
Figure 3.11. *Spectroscopy on the two π Zeeman components with a misaligned probe beam. We see appearing on each side of the 2 carrier π transitions motional sidebands due to the quantified transverse confinement in the optical lattice. The solid line is a fit with a sum of Gaussian lineshapes.*

3.3.2   Estimation of the trap depth

Even though detrimental from a metrological point of view, as they can create systematic shifts such as line pulling, the motional sidebands give us precious information about the lattice potential, and more specifically, knowing the waist of the lattice trap, we can directly extract the trap depth looking at the sidebands frequency.

Indeed, there is a simple relation between trap depth and (transverse) sideband frequency:

$$\omega_\perp = \frac{2\sqrt{2}E_{rec}}{\hbar k_{lat} w_0} \sqrt{\frac{U_0}{E_{rec}}} \tag{3.11}$$

where E_{rec} is the lattice recoil energy (equation 12), w_0 the lattice waist, in our case 69 μm, and U_0/E_{rec} is the trap depth in units of the lattice recoil energy.

If we assume a linear relationship between the total flux of the lattice light (and therefore U_0) and the signal detected by the photodiode monitoring the lattice cavity transmission S, in V units (see layout of the lattice optics and locking electronics in Section 1.3.2), we can rewrite Equation 3.11 as

$$\omega_\perp = A\omega_{rec}\sqrt{\frac{\kappa_{PD}S}{E_{rec}}} = A\hbar^{-1}\sqrt{E_{rec}}\sqrt{\kappa_{PD}S} \tag{3.12}$$

where $A = \frac{2\sqrt{2}}{k_{lat}w_0} = \frac{\sqrt{2}\lambda_{lat}}{\pi w_0}$ is a dimensionless scaling factor, $\omega_{rec} = 2\pi \times$ 7.5 kHz and κ_{PD} is a calibration factor with dimension of (E_{rec}/V). κ is of chief importance for clock operation, since S is our only way to monitor and vary the lattice depth, which is a crucial parameter for the estimation of lattice-related frequency shifts (see Section 5.3).

Investigating the sidebands frequency separation from the carrier for several lattice intensities, and using Equation 3.12, we are able to experimentally measure κ_{PD}, and therefore express the voltage offset of the sidelock of the lattice cavity in units of lattice recoils. Prior to my PhD, in order to do this calibration, we were using an estimation of the power coupled to the buildup cavity from the specification of the cavity mirrors and a measurement of the power before the cavity to determine the trap depth with a few percent uncertainty at best. We expect that the method using atomic sideband spectroscopy will yield a much more accurate result.
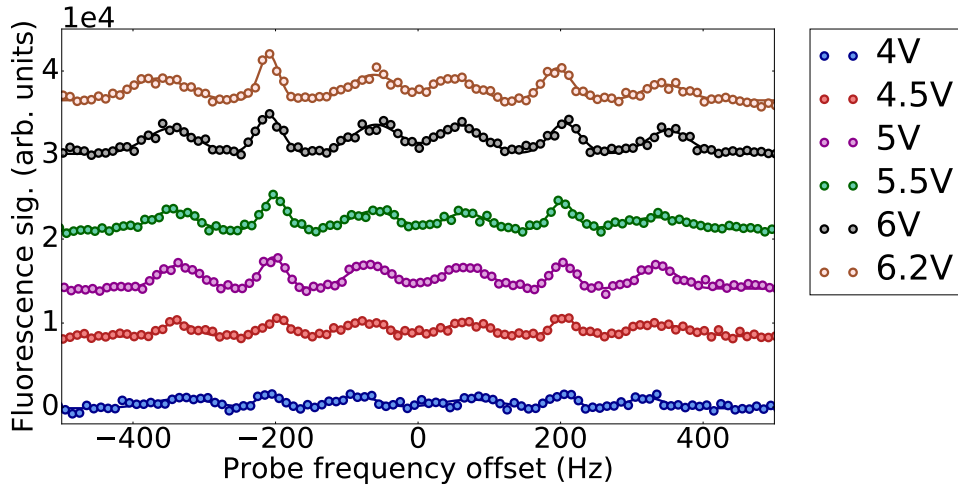
Figure 3.12. *Spectroscopy curves featuring the transverse sideband spectra at multiple lock point (or intensities) of the lattice. From a fit with multiple Gaussian functions, we extract the sideband frequencies with respect to the carriers (see main text). The curves are shifted vertically for visibility.*

Figure 3.12 shows the experimental sideband spectra for different trapping powers. We fit each spectrum with a sum of gaussian functions (Figure 3.11 shows an example of such a fit) and extract the center of each of the six gaussians. We then take the difference between the center of the carrier and the center of the two sidebands for both Zeeman carriers, which gives us four estimations of the sideband

frequency, $\omega_\perp^{red}(-1/2 \to -1/2)$, $\omega_\perp^{blue}(-1/2 \to -1/2)$, $\omega_\perp^{red}(+1/2 \to +1/2)$ and $\omega_\perp^{blue}(+1/2 \to +1/2)$. Under the assumption that the sidebands are symmetric around the carrier and that the red and blue sidebands have the same frequency (in absolute value), we finally compute the sideband frequency $\omega_\perp(mean)$ (which we will note $\omega_\perp$ in the following), taken as the average of the four frequencies mentioned above.
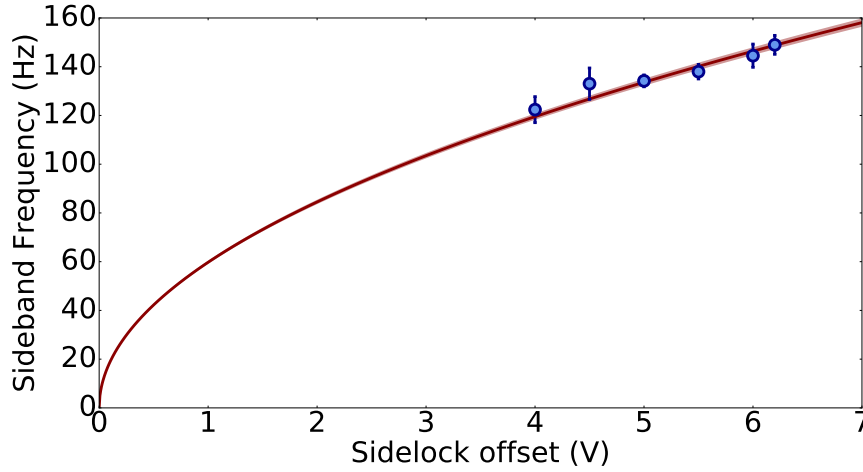
Figure 3.13. *Sideband frequencies as a function of sidelock offset. From a fit with the model of equation 3.13 we can deduce the conversion factor between V on the sidelock and trap depth in E_{rec} (red curve). The uncertainty on the fit is visualized by the shaded light red area.*

We then plot the sideband frequencies extracted from the spectra as a function of S, which is shown on Figure 3.13. We can see that as expected from Equation 3.12, $\omega_\perp$ increases with increasing lattice depth S with a square root dependence. A fit to the function

$$\omega_\perp = 2\pi B\sqrt{S} \tag{3.13}$$

gives us $B = 59.8(6)$ Hz/$\sqrt{\text{V}}$. By comparing Equations 3.12 and 3.13, we obtain

$$\kappa_{PD} = \left(\frac{B}{A\nu_{rec}}\right)^2 = 11.1(1)\frac{E_{rec}}{\text{V}} \tag{3.14}$$

Previously, we had estimated κ_{PD} to be close to 14 E_{rec}/V based on the specifications of the lattice mirrors, the expected beam waist of 69 μm inside the lattice cavity and crude parametric heating measurements.

In Section 3.4, we will check the consistency of our measurement by studying the dynamics of the atoms in the lattice through the process of resonant parametric excitation.

3.4   Studies of Parametric Excitation in the Trap

Parametric excitation is a physical phenomenon encountered in a wide range of situations and physical systems. It has been used to characterize trapping conditions and atom dynamics in optical lattice traps [41].

To perform parametric excitation in an oscillating physical system, one needs to modulate the natural frequency of the oscillator. When the modulation frequency, ω_m is twice the trapping frequency, energy is transferred from the modulation source to the atoms, which are then expelled from the trap.

Figure 3.14. *Scheme of the lattice parametric excitation setup. VCO: Voltage-Controlled Oscillator, SHG: Second Harmonic Generation.*

In our case, we modulate the intensity of the lattice laser using an AOM on the path to the lattice cavity (we are sending the 0th order to the cavity, and are dumping more or less light into the 1st order to modulate the intensity). By doing so, we are able to resonantly excite

the oscillating motion of the atoms in the harmonic wells of the lattice, and observe losses of atoms from the trap.

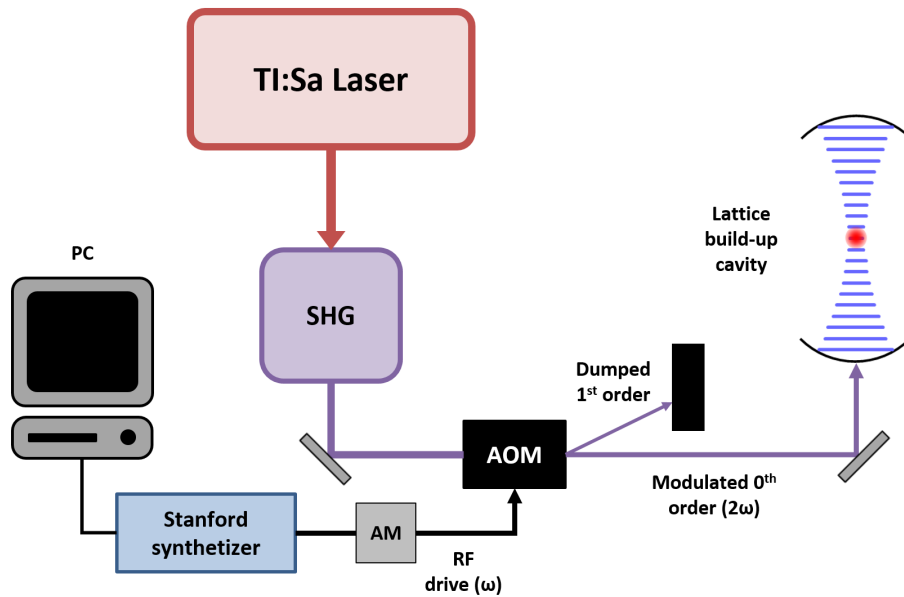One important issue arises due to the fact that the frequency response of the amplitude modulation of the AOM is non-linear. When modulating the amplitude of the AOM at frequency ω, we will generate an unwanted modulation at frequency 2ω, which will spoil the spectra of parametric excitation.

A good way to get rid of this issue is to actually work near zero offset amplitude, where the behavior is almost completely quadratic. In that case, we have checked on the spectrum of the light from the AOM that only the second harmonic of the modulation frequency is generated, with more than 30 dBm difference between the power at ω and the power at 2ω, provided that the modulation amplitude is small. The experimental setup is shown on Figure 3.14.

A Stanford digital synthesizer SRDS45, which is digitally controlled sends a voltage modulation onto the amplitude modulation port of the AOM driver, which drives the AOM at frequency ω. The laser beam going through the AOM get amplitude-modulated at frequency 2ω, and is sent to the lattice buildup cavity.

3.4.1   Trap depth estimation

We first study parametric excitation of the atomic motion along the transverse direction of the lattice, shaking the lattice at a frequency close to the transverse frequency of the lattice trap ($\simeq 100$ Hz), since this provides us with a direct comparison with the lattice sideband spectra of section 3.3.1. The parametric excitation curves shown on Figure 3.15 (a) have been taken with a 20 ms long modulation, with an amplitude of 1.2 V (modulation depth of $\simeq 30$ %).

We clearly see the resonance occurring for a driving frequency close to twice the transverse motional sideband frequency in the lattice trap, with the exact frequency depending on the offset of the lattice sidelock (or equivalently the trap depth). We have checked that the scaling goes roughly as a square root law, as was the case for the sideband frequency in the spectra of section 3.3.1.

(a)

(b)

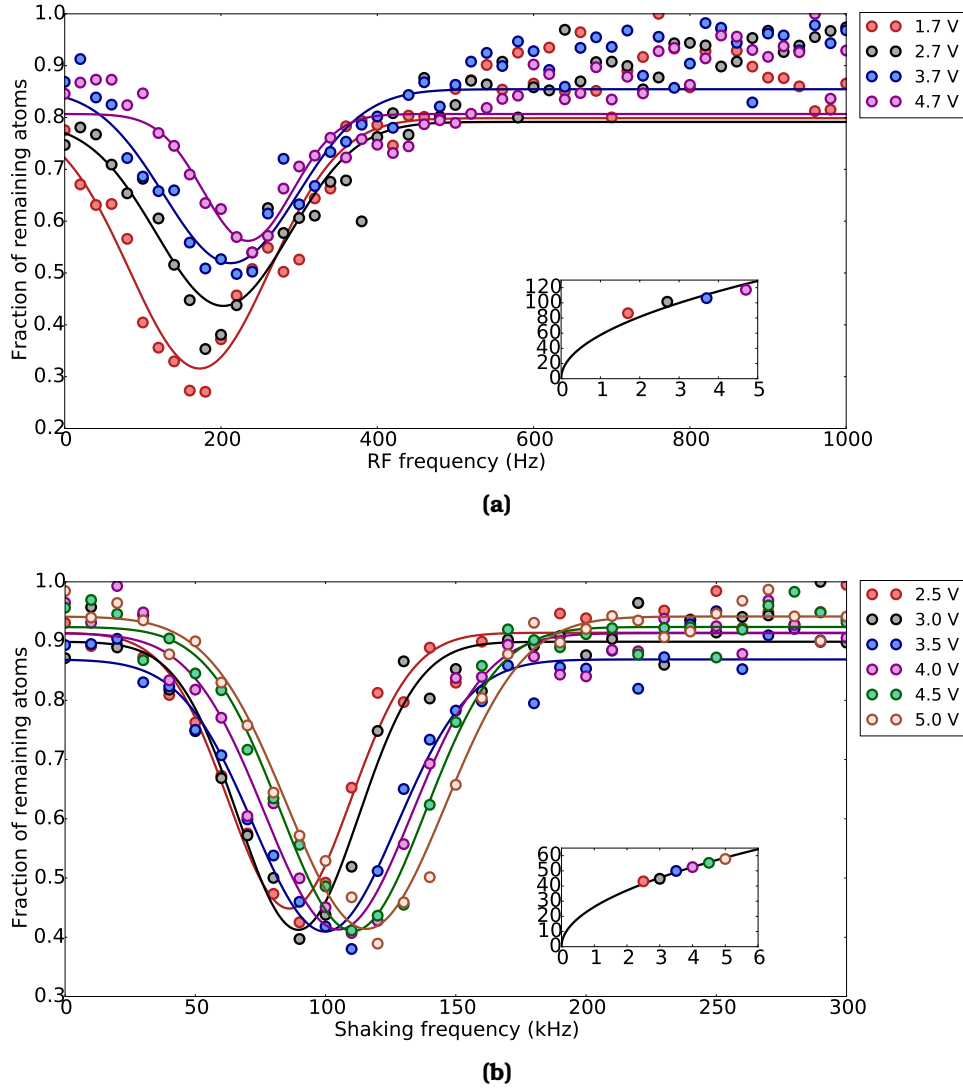**Figure 3.15.** *Lattice shaking spectra, taken for different trap depth. The frequency shown on the x-axis is the frequency at which the lattice trap is modulated. (a) Transverse lattice shaking spectra and (b) Longitudinal lattice shaking spectra. The inset shows the square root dependence of the resonance frequency as a function of lattice depth, obtained by fitting the resonance spectra with a gaussian lineshape.*

The coefficient extracted from a fit with Equation 3.13 gives B = 57(3) E_{rec}/V, in perfect agreement with the result obtained in Section 3.3.2 by fitting the transverse sidebands. This good agreement gives us confidence that we know the trap depth down to the few-% level. We have also checked that we can parametrically excite the atoms out of the trap by shaking it at a frequency close to twice the longitudinal trapping frequency ($\simeq$ 100 kHz).

A few spectra are shown on Figure 3.15 (b) for different trap depth. All the parametric excitation curves shown on the figure have been taken with a 200 ms modulation, with a modulation amplitude of 0.1 V (that is a modulation depth of 2 to 4 %). In that case, the scaling also goes as a square root law, as expected from studies of longitudinal sideband spectra (see inset of Figure 3.15 (b)) realized by several groups on other atoms [6]. Since we cannot excite the longitudinal sidebands in the lattice trap with the clock laser due to a lack of laser power, these spectra provide us with a way to evaluate the trapping conditions in the longitudinal direction. There are however limits to the validity of this picture, for example the dynamics of the expulsion of atoms from the trap which is hard to model, and the anharmonicity of the trapping potential which is not taken into account.

3.4.2   Atomic temperature filtering

We have seen that parametric oscillation of atoms in the lattice trap gives information about the spring constant of the trap itself, but it turns out that the width of the parametric spectrum also provides us with qualitative information about the atoms dynamics in the trap.

Indeed, we apply a procedure which consists in lowering the lattice depth by a controlled amount (expressed in V on the lattice sidelock offset on Figure 3.16), to filter-out the hotter atoms and let them leave the lattice trap. We characterize the effect of the filtering by looking at lattice shaking spectra. By varying the amplitude of the lattice ramp-down we are able to modify the atomic velocity distribution in a controlled way, as shown on the curves of Figure 3.16. All the parametric excitation curves shown above have been taken by first ramping down the lattice depth in 5 ms, waiting for the hot atoms to escape during 20 ms, and then ramping the lattice depth back up in 5 ms. This fil-

(a)

(b)
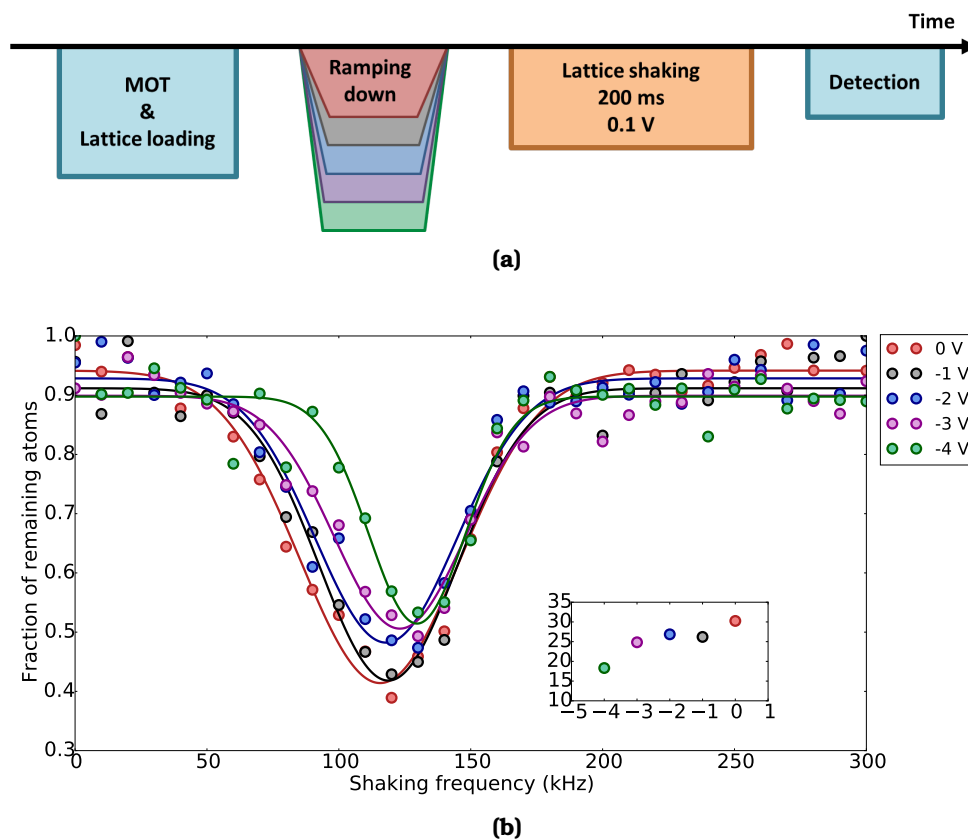
Figure 3.16. *(a) Hot atom filtering sequence and (b) Parametric excitation spectra obtained by ramping down the lattice depth to get rid of the hotter atoms according to the experimental sequence above (colored dots). We fit the curves with a gaussian lineshape (full lines). The linewidth (in kHz) extracted from the fits is plotted in the inset as a function of the lattice ramp-down.*

tering period is then followed by the parametric excitation diagnostic, applying a 200 ms long modulation with a modulation depth of 0.1 V.

The filtering procedure has a significant impact on the width of the parametric excitation spectra. We have tried to quantify this statement by fitting the width of the parametric resonances with a gaussian lineshape, and plotting the width as a function of the amplitude of the lattice ramp-down. This is shown on the inset of Figure 3.16.

We are able to reduce the width of the sideband spectrum by almost factor of two, at the price of a decrease in the number of atoms. In our current experimental conditions, this decrease is too important for robust clock operation. However, when the 2D-MOT is operational, yielding increased atom numbers, this simple and fast proce-

dure might be a very efficient way to modify the atomic temperature distribution, which is expected to have an impact on clock accuracy (see Section 5.3.3 for more details).

One interesting thing to note is that the filtering reduces the width of the distribution in a clearly asymmetric fashion. Indeed, the blue edge (at higher frequencies) of the spectra is fixed, only the red edge of the resonance gets shifted when the resonance narrows as a consequence of the lattice ramp-down. This asymmetric narrowing is reminiscent of longitudinal blue-sideband spectra, which also feature an asymmetry where the slope of the curve is much steeper on the blue side of the resonance than on the red. In this regard, a simple model of the lattice shaking dynamics would be valuable, in order to be able to fit the spectra with parameters related to the thermal distribution of atoms in the trap, and the trapping potential.
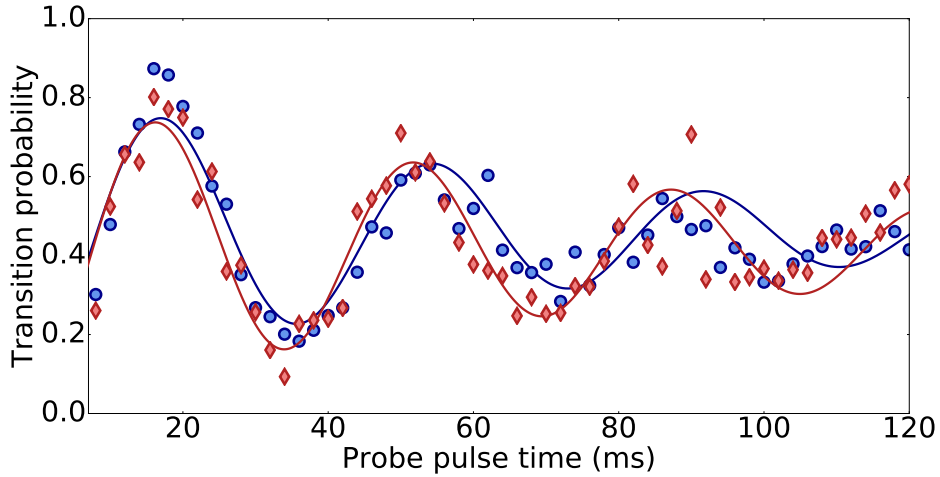
Figure 3.17. *Carrier Rabi flopping curves without (blue dots) and with (red diamonds) atom filtering. The full lines are fit with a damped sinusoidal function.*

We can also visualize the impact of hot atoms filtering by looking at Rabi flopping curves. Since due to imperfections in the experimental setup, the probe is not perfectly aligned with the lattice axis. Therefore, the Rabi frequency of the carrier transition is impacted by the transverse atomic motion, and modifying the transverse atomic temperature distribution by ramping down the lattice depth should have an impact on the Rabi flopping experiments.

Figure 3.17 shows the Rabi flopping curves obtained when applying the filtering procedure (red diamonds) and without any filtering (blue

dots).

The parameters extracted from the fit (see Section 3.2.5) to the filtered curve are Ω_{filt} = $2\pi \times 28$ Hz (Ω = $2\pi \times 27$ Hz), C_{filt} = 0.4 (C = 0.4), and γ_{filt} = 91 ms (γ = 75 ms) for the filtered (unfiltered) data respectively, showing the slightly improved coupling of the clock laser to the atoms when operating with the filtered atomic distribution.

Chapter 4

Clock Operation and Short-Term Stability Optimization

In this chapter, we turn to the characterization of the frequency instability of the mercury optical lattice clock, which is to say the ultrastable clock laser referenced to the $^1S_0 \to {}^3P_0$ atomic transition.

Frequency instability is a key figure of merit for clocks, as it is a measure of the clock frequency noise. As we shall see in the following sections, a proper analysis of this noise provides physical insight into the **nature** of the different noise processes affecting the clock transition frequency, and the experimental levers which can be used to eliminate or reduce them.

From a metrology standpoint, the frequency instability is also the **statistical uncertainty** affecting a given clock frequency measurement. If the clock frequency is averaging as $1/\sqrt{\tau}$ (dominated by white frequency noise) as is often the case for atomic clocks, starting from 10^{-15} at 1 second averaging time, we will need 100 seconds to reach the 10^{-16} level of statistical accuracy.

Therefore, instability is also a crucial parameter for frequency ratio measurements and clock systematics evaluation, which will be the topic of the last two chapters of this thesis.

As mentioned in the Introduction, in the community of frequency metrology, clock instability is most commonly computed and visualized thanks to the Allan standard deviation (ADEV) or the Overlapping

Allan standard deviation [2].

The subject of this chapter is to first investigate the different sources of frequency (in)stability of our clock, and quantify and characterize them thanks to the Allan standards deviation, and second to find ways to improve the stability of the clock for frequency-ratio measurements. Our goal is to reach a clock stability of 10^{-15} at one second, giving access to measurement resolutions at the level of 10^{-17} after approximately half an hour of averaging, in order to characterize systematic frequency shifts in a reasonable amount of time.

4.1   Locking to the Atomic Resonance

The apparatus works as a clock when the clock laser is servo-locked to the atomic transition creating a composite system clock laser + atoms. I will give a few details about how this atomic servo is implemented on our experiment. In order to servo the clock laser to the atomic transition, we use a square-wave frequency modulation locking scheme [63]: we probe the atomic population using a π pulse of the clock light alternatively detuned by $+\delta$ and $-\delta$ from the expected center of the resonance $\nu(t)$, where δ is the Half-Width at Half Maximum (HWHM) of the transition lineshape, which for Rabi spectroscopy is

$$\delta \simeq \frac{1}{2} \times \frac{0.8}{T_\pi} \tag{4.1}$$

This alternative probing yields the measured populations (or transition probability on the case of normalized detection, see Section 3.2.3) $p_+(t)$ and $p_-(t)$. We then derive the error signal of the clock $\epsilon_{sig}(t) = p_+(t) - p_-(t)$ and we use an integral servo to correct the frequency of the laser and keep the error ϵ_{sig} close to zero:

$$y_n = y_{n-1} + (-1)^{n-1} K_i \epsilon_n \tag{4.2}$$

Where K_i is the integral gain which we adjust empirically. An example is shown on Figure 4.1. If the populations $p_+(t)$ and $p_-(t)$ are unbalanced (violet dots on the blue atomic resonance) then we apply a correction to the laser frequency through a frequency shifter (a synthesizer feeding and AOM on the beam path) to keep it locked to the atomic transition.
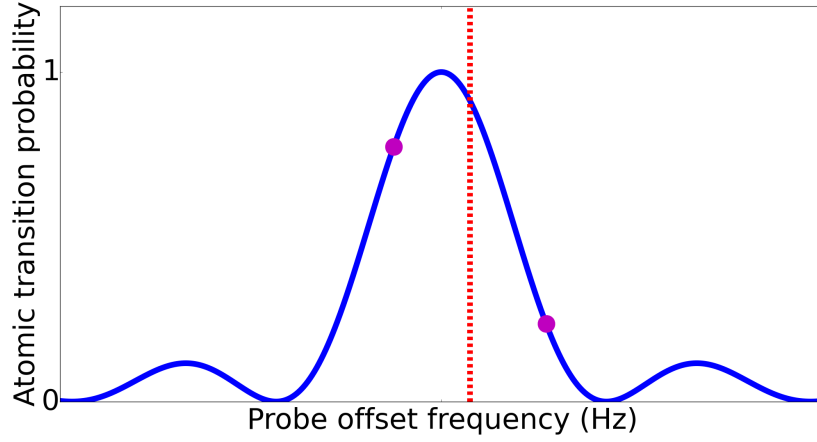
Figure 4.1. *Principle of laser-locking to the atomic resonance: The dashed red line represents the expected resonance frequency at time t. The laser is detuned by +δ then -δ, and the corresponding atomic populations are measured (violet dots). The imbalance between the two population measurements is used to determine the frequency correction which needs to be applied to the laser to keep it at resonance with the atoms (in this particular instance, the probe laser frequency has to be steered towards the negative frequencies.*

This scheme is quite simple and robust, however a major frequency bias arises due to the quantization magnetic field which creates a linear Zeeman effect and splits the atomic transition into two Zeeman lines (see Chapter 3 for more details). This means that by locking the clock laser to one of the Zeeman lines, we introduce a shift with respect to the unperturbed clock frequency of $\delta\nu_{Zeeman} = \mu_B \delta g m_F B/h$ where B is the magnetic field, and this shift is as large as 200 Hz in normal configuration, which means that in order to keep the clock uncertainty at the level of 10^{-18}, we would have to know the magnetic field down to an uncertainty of 10^{-5} (see Chapter 5 for more details). Moreover, magnetic field fluctuations will impact the in-loop stability of the clock to first order.

To mitigate these issues, a commonly used technique is to implement a stretched-state servo loop on the two Zeeman components [105].

The servo loop works as follows: we first interrogate the left side of the $^1S_0(m_F = -1/2) \rightarrow {}^3P_0(m_F = -1/2)$ which we denote $p_-^{-1/2}(t)$ (left red dot on the left peak of Figure 4.2). We then interrogate the left side of the $^1S_0(m_F = +1/2) \rightarrow {}^3P_0(m_F = +1/2)$ which we denote
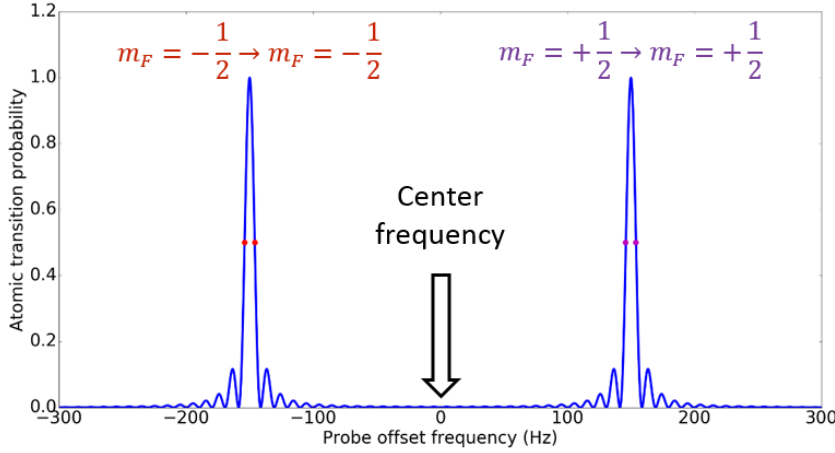
Figure 4.2. *Theoretical stretched Zeeman state spectroscopy curve (blue trace). By alternatively probing the two atomic resonances, we effectively lock the clock laser to the unperturbed center-frequency, visualized by the vertical arrow. The splitting between the two Zeeman components is on the order of a few hundred Hz in typical clock operation.*

$p_-^{+1/2}(t)$ (left violet dot on the right peak of Figure 4.2). We follow by interrogating the right sides of the $^1S_0(m_F = -1/2) \to {}^3P_0(m_F = -1/2)$ and $^1S_0(m_F = +1/2) \to {}^3P_0(m_F = +1/2)$, denoted respectively $p_+^{-1/2}(t)$ (right red dot on the left peak of Figure 4.2) and $p_+^{+1/2}(t)$ (right violet dot on the right peak of Figure 4.2).

We construct the error signals:

$$\epsilon_{sig}^{+1/2} = p_+^{+1/2} - p_-^{+1/2}$$
$$\epsilon_{sig}^{-1/2} = p_+^{-1/2} - p_-^{-1/2}$$

(4.3)

and we have two servo independent but interleaved loops such as the one described above in the single Zeeman component case running in parallel, keeping both errors signals close to zero, and thereby tracking line centers of the two Zeeman components.

A typical data run looks like the graph shown on Figure 4.3. The frequency data are extracted from the correction applied to the AOM frequency shifter, and the interleaved signals are demodulated. As can be seen on Figure 4.3, even though each integrator is updates every two clock cycles, the fully interleaved frequency correction is extracted every clock cycle.
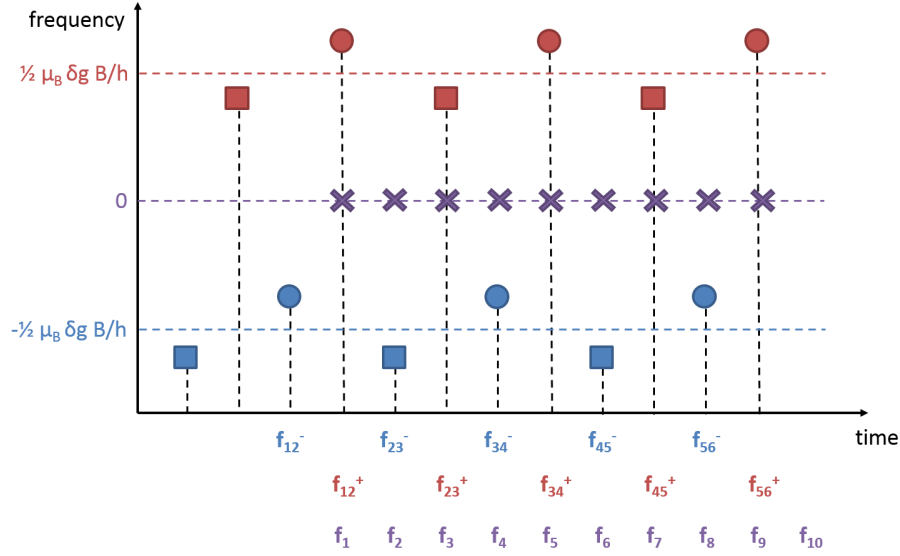
Figure 4.3. *Typical frequency locking data as a function of time. Squares on the figure represent probing of the right side of the transition, while the circles represent probing on the left side. Blue data points are used for m_F = -1/2 and red data points for m_F = +1/2. Finally, the violet crosses show the extracted center frequency from both servos after demodulation. For each servo, an error is computed every 2 clock cycle, however making use of the full interleaving of the data, we can derive the error signal of the clock every cycle (frequencies represented in violet below the time axis).*

4.2 Allan Deviation and Clock Stability

In the frequency metrology community, the Allan standard deviation is a commonly used to characterize the noise of oscillators and clocks, and it is the purpose of this section to introduce this notion in the context of this thesis. The generic expression for the frequency of an oscillator as a function of time is given by Equation 2.

Since we are only interested in the frequency stability, or in other words the frequency noise affecting the oscillator, we can for the moment assume that the frequency offset ϵ is 0. We can then rewrite Equation 2:

$$y(t) = \frac{\nu_{Hg}(t) - \nu_0}{\nu_0} \tag{4.4}$$

We calculate the Allan variance [2] of y defined as :

$$\sigma_y^2(\tau) = \langle \frac{(\overline{y_{n+1}} - \overline{y_n})^2}{2} \rangle \tag{4.5}$$

and we define from this variance what we call clock (or oscillator) fractional frequency instability, often abbreviated **stability** in the literature, which is simply the square-root of the Allan variance of frequency fluctuations.

Experimentally, there are several sources of noise which will degrade the stability of our frequency standard, and the Allan standard deviation of clock frequency fluctuations is usually found to be for Rabi spectroscopy:

$$\sigma_y(\tau) \simeq \frac{1}{3.03 Q_{at}} \sqrt{\frac{\tau_{cycle}}{\tau}} \sqrt{\frac{1}{N_{atoms}} + \frac{1}{N_{atoms} n_{ph}} + \frac{2\sigma_{\delta N}^2}{N_{atoms}^2} + \sigma_{tech}^2} \quad (4.6)$$

Where τ_{cycle} is the duration of a clock cycle, τ is the integration time, N_{atoms} is then number of probed atoms in the lattice, n_{ph} is the number of photons detected per atom (in our case $n_{ph} \sim 40$), $\sigma_{\delta N}$ is the uncorrelated rms fluctuations of the atom number, and σ_{tech}^2 is the contribution of the frequency noise of the local oscillator and

$$Q_{at} = \frac{\nu_0}{\Delta \nu_{\text{Rabi}}} \quad (4.7)$$

is the atomic quality factor of the Rabi-lineshape to which the clock is locked.

We see that the clock stability is the sum of several noise contributions, which we will now examine one by one.

4.3 Fundamental Sources of Noise

We will first focus on types of noises which we call "fundamental" noise processes, i.e. processes which are inherent to the cyclic operation of an atomic frequency standard using the detection of uncorrelated atoms via a protective quantum measurement.

These include cycle-synchronous local oscillator frequency fluctuations, which are unavoidable when looking at the stability of a single frequency standard operated in a cyclic fashion, but which we will be able to suppress when comparing two clocks as we will see later on (see Section 4.6), and noise coming from the quantum, probabilistic nature of our frequency discriminator, namely the detected fluorescence which randomly projects the atoms in a particular quantum state.

Even with a 100 % efficiency of the detection scheme, these types of noise will impact the frequency stability of our clock.

4.3.1 Quantum projection noise

The first noise contribution comes from the random nature of the process involved in detecting the quantum state of the clock atoms. Ideally, this fundamental quantum noise limit should be the dominant noise contribution to our frequency standard.

Let us imagine for simplicity that we are probing a single two-level atom, which is fine for modeling the mercury clock as long as interactions between probed atoms or entanglement are negligible. This atom can be in its ground state $|g\rangle$ or in its excited state $|e\rangle$.

Excitation by the clock laser creates a quantum superposition of ground and excited states $|\phi\rangle = c_g|g\rangle + c_e|e\rangle$.

We then detect the atoms, which has the effect of projecting the superposition into one of the eigenstates $|g\rangle$ or $|e\rangle$ and the probability of finding the system in $|g\rangle$ or $|e\rangle$ is respectively $|c_g|^2$ and $|c_e|^2$. However, even though $|c_g|^2$ and $|c_e|^2$ follow a deterministic evolution, the projective measurement is intrinsically probabilistic and therefore the result of the measurement cannot be determined a priori.

We will now see that from this indeterminacy arises a source of noise on the clock signal, which is called in the literature Quantum Projection Noise (QPN in short) [40]. For clock operation, we usually excite a group of N atoms to a given excited state population fraction $p = |c_e|^2/\big(|c_e|^2 + |c_g|^2\big)$ (in general the clock is operated with $p = 1/2$, which gives the best sensitivity for the frequency discriminator of the clock).

For one atom, the variance of the measurement of the atomic state population fraction due to the QPN reads [40]:

$$\sigma_p^2 = p(1 - p) \tag{4.8}$$

In the case of N uncorrelated atoms, this expression scales as $1/N$ for the variance, and $1/\sqrt{N}$ for the standard deviation, yielding the fluctuations in atomic state population fraction

$$\sigma_p(N) = \sqrt{\frac{p(1 - p)}{N}} \tag{4.9}$$

Since these fluctuations are indistinguishable from probe laser frequency noise, they degrade the clock stability. Cold atom frequency standards limited by QPN have already been demonstrated [100] in the microwave domain, and it is the regime in which ion clocks usually operate [42]. For optical lattice clocks QPN-limited operation is within reach, but local-oscillator induced instabilities (see Section 4.3.2) still prevents the routine operation of QPN-limited frequency standards [1].
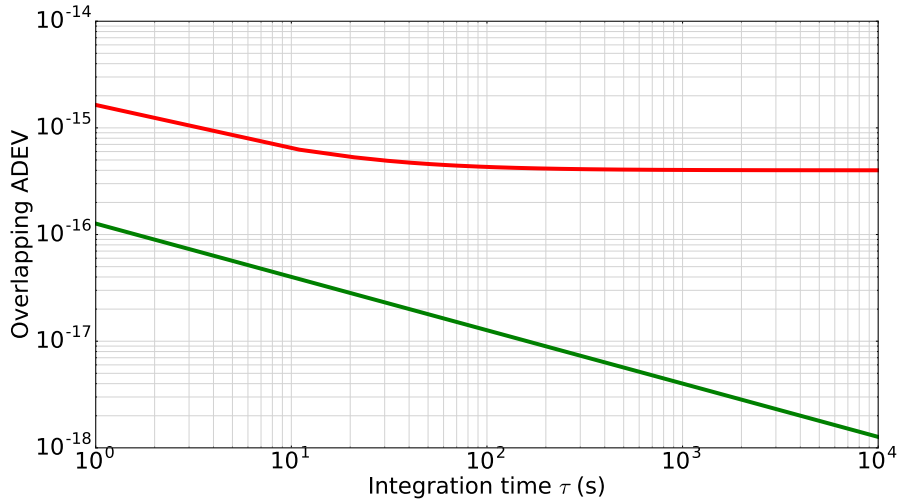
Figure 4.4. *Overlapping Allan standard deviation model of the typical clock frequency noise assuming a short term stability of 1.5×10^{-15} at 1 second and a flicker floor of 4×10^{-16} (red trace). Overlapping Allan standard deviation for QPN alone (green trace) assuming a 1s cycle time, 100ms probe time and 500 atoms probed in the lattice.*

In the case of Rabi spectroscopy, the link between the fluctuations of transition probability and the frequency fluctuations is the slope of the Rabi line shape at the point of locking . From this, we can obtain an approximate formula for the frequency instability due to quantum projection noise [1]:

$$\sigma_y(\tau) = \frac{1}{3.03 Q_{at}} \frac{1}{\sqrt{N_{atoms}}} \sqrt{\frac{\tau_{cycle}}{\tau}} \qquad (4.10)$$

Where Q_{at} is the atomic quality factor of the Rabi lineshape (see eq 4.7), N_{atoms} is the number of atoms, τ_{cycle} is the cycle time and τ the integration time.

In the case of Rabi spectroscopy, Q_{at} can be simply evaluated, since $\Delta\nu \simeq 0.8/T_\pi$ where T_π is the length of the π pulse used for interrogation. This noise contribution scales as white noise, going down as $1/\sqrt{\tau}$, as can be seen on figure 4.4.

We see that QPN is not a limitation at our nominal interrogation time of 100 ms, contributing 1.1×10^{-16} fractional frequency instability for a realistic 500 atoms detected in the lattice.

4.3.2 The Dick effect

As previously mentioned, the clock is operated in a cyclic fashion, because of the destructive nature of the detection method employed, and therefore the need to reload atoms into the lattice after each successful detection period.

Consequently, during this "dead-time" needed to cool the new sample of atoms and load it into the optical lattice (approximately 90%, 900 ms dedicated to atomic sample preparation out of a 1 s cycle), the clock laser is not compared against the atoms and its noise is not corrected. The noise of the clock laser is sampled by the atoms with a sampling rate equal to the inverse of the cycle time of the clock.

This sampling introduces a phenomenon well know in signal processing, the down-conversion of high-frequency noise from the local oscillator through aliasing into the bandwidth of the lock to the atomic transition [88]. This process degrades the stability of the clock, and depending on the experimental conditions can even be the limiting factor to the stability of the clock. This effect depends on the **sensitivity function** $g(t)$ of the atomic sample to local oscillator noise and is defined by [21], [98]:

$$\delta f = \frac{1}{2} \int_0^{T_c} \Delta(t) g(t) dt \tag{4.11}$$

where $\Delta(t)$ is the frequency noise on the laser and T_c is the cycle time. In the case of Rabi spectroscopy, we can write an analytic formula for the sensitivity function, and for its Fourier transform which is the relevant parameter entering into the calculation of the instability introduced by the Dick effect [62]:

$$g(t) = -\left(\frac{\Delta \Omega_0^2}{\Omega^2} \right) \left[\sin(\Omega t) - \sin\left(\pi \frac{\Omega}{\Omega_0} \right) + \sin\left[\frac{\Omega}{\Omega_0} (\pi - t\Omega_0) \right] \right] \tag{4.12}$$

$$\tilde{g}(\nu) = \frac{\Delta \Omega_0^2}{\Omega^2 (\pi \nu \Omega^2 - 4\pi^3 \nu^3)} \left[\Omega \sin\left(\frac{\pi^2 \nu}{\Omega_0} \right) \sin\left(\frac{\pi \Omega}{\Omega_0} \right) - 4\pi\nu \cos\left(\frac{\pi^2 \nu}{\Omega_0} \right) \sin^2\left(\frac{\pi \Omega}{2\Omega_0} \right) \right] \tag{4.13}$$

where Ω_0 is the bare Rabi frequency, and Ω is the generalized Rabi frequency defined as $\Omega = \sqrt{\Omega_0^2 + \Delta^2}$. As the side-note, in Equation

(a)

(b)
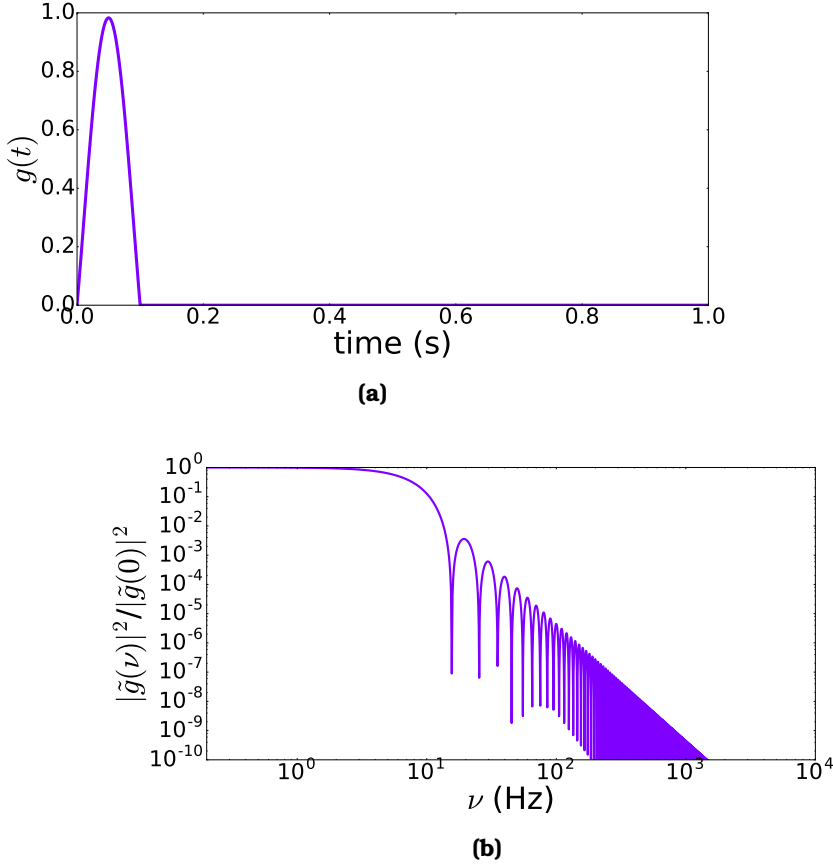
Figure 4.5. *(a) Plot of the spectroscopic sensitivity function as a function of time in one cycle and (b) Plot of the normalized Fourier coefficients of the sensitivity function as a function of frequency.*

4.12 the origin of time is taken at the beginning of the clock pulse interrogation.

Both functions are plotted on Figure 4.5. We can see that the atomic response acts as a low pass filter for the laser noise through the sensitivity function, but nevertheless through the aliasing process, some high-frequency noise will still contribute to the instability.

The resulting contribution of the Dick effect to the clock instability can be written:

$$\sigma_y^2(\tau) = \frac{1}{\tau} \sum_{n=1}^{\infty} \frac{S_\nu(n/\tau_{cycle})}{\nu_0^2} \frac{|\tilde{g}(n/\tau_{cycle})|^2}{|\tilde{g}(0)|^2} \qquad (4.14)$$

In the above expression, $S_\nu(f)$ is the free-running probe laser frequency noise power spectral density, which is therefore a crucial parameter in the estimation of the Dick effect. Based on a beating be-
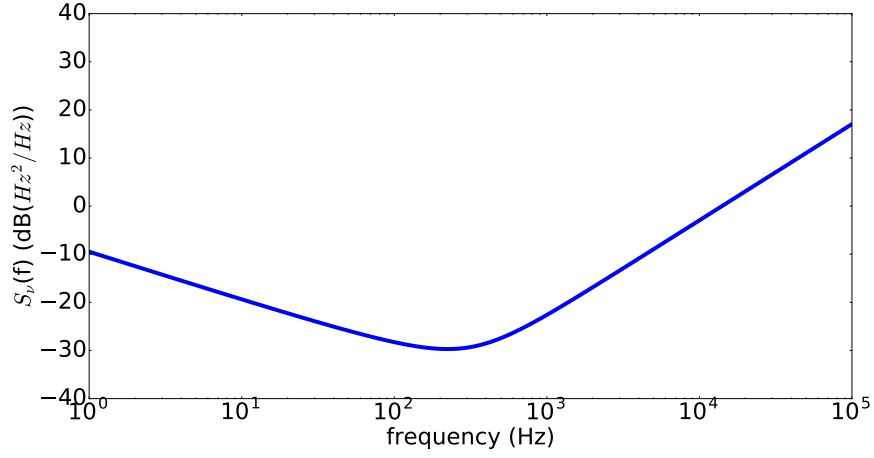
Figure 4.6. *Laser frequency noise power spectral density expressed in dB(Hz^2/Hz as a function of the frequency. Our model assumes a frequency flicker noise floor of 4.10^{-16} with white phase and frequency noise.*

tween our ultrastable laser and a similar system [71], we can build a model for the noise of our laser:

$$S_\nu(f) = \frac{h_{-1}}{f} + h_0 + h_2 f^2 \tag{4.15}$$

This model, which is plotted on Figure 4.6 assumes 3 contributions:

- Flicker frequency noise, scaling as $1/f$ with a coefficient h_{-1} = 0.11 Hz^2.

- A white frequency noise floor with coefficient h_0 = 3.2 × 10^{-4} Hz^2/Hz.

- White phase noise with a coefficient h_2 = 5.1 × 10^{-9} (Hz^2/Hz)^2.

We can finally plot the contribution of the Dick effect to the clock stability as a function of integration time (equation 4.14) for our nominal clock interrogation time of 100 ms (Figure 4.7).

We can see that if it is not yet the limiting factor for our clock stability, it lies only a factor of 2 below our currently estimated clock stability at short timescales.

4.3.3   Optimization of clock stability

In operating the mercury clock, our goal is quite plainly to have a fractional clock frequency instability compatible with the study of
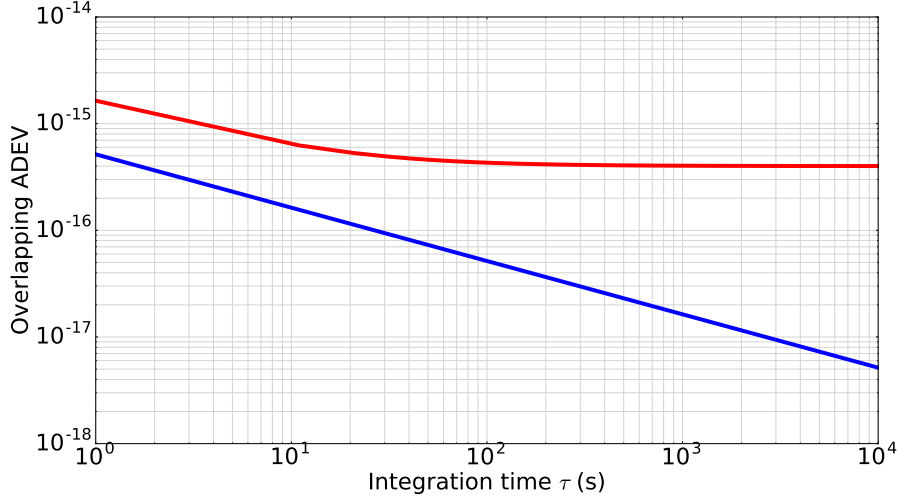
Figure 4.7. *Overlapping Allan standard deviation model of the typical (atoms + clock laser) frequency noise assuming a short term stability of 1.5×10^{-15} at 1 second and a laser flicker floor of 4×10^{-16} (red trace). Overlapping Allan standard deviation for Dick effect alone (blue trace) assuming a 1s cycle time and 100 ms probe time.*

clock systematics with a resolution of 10^{-17} 1000 seconds of integration time. This corresponds to a clock instability of 1×10^{-15} at one second. In this section, taking into account the typical experimental conditions, we estimate the smallest attainable frequency instability in our setup based on the sum of the contributions from QPN and Dick effect. Figure 4.8 shows the calculated clock instability due to the combined contributions of the Dick effect and QPN. Shown on the plot is the clock instability at one second of averaging time as a function of the probing time, which is the most experimentally relevant parameter, impacting both QPN and Dick effect. Several parameters enter into play:

If a longer probe time is desirable both to reduce quantum projection noise and the Dick effect, our model takes into account the fact that in our present operating conditions, we measure an atom number which is decreasing over time because of losses of atoms from the lattice, with a time constant of 300 ms. Moreover, lengthening the probing time also increases the clock cycle time, which in turn degrades the stability.

We indeed observe that in the limit of our model, there is a trade-off between long interrogation times, high atom numbers and short cycle times, which yields an expected optimum for the combined stability
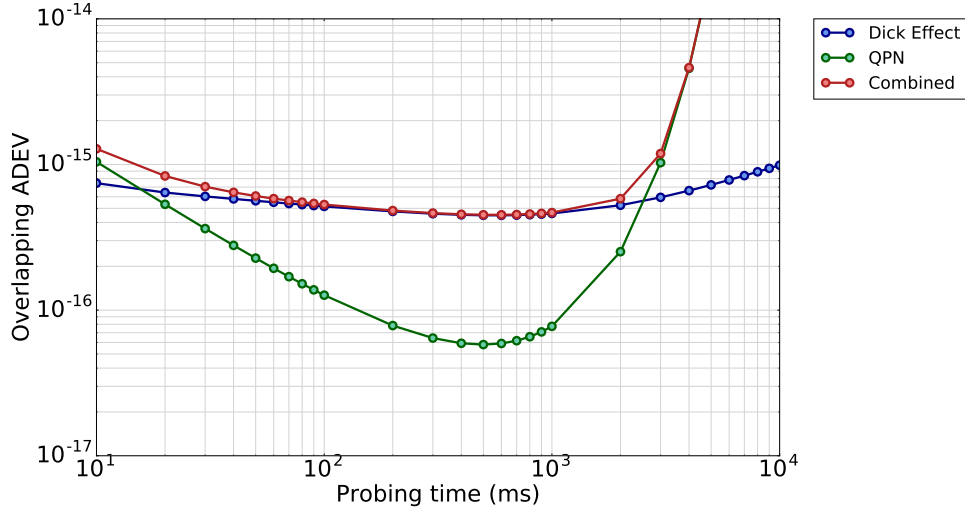
Figure 4.8. *Calculated clock stability at 1 second as a function of interrogation time (colored dots). The filled lines are just guides for the eyes.*

with a probe time of 300 ms. Unfortunately, when operating with such long probe pulses, the lock to the clock transition becomes unstable, because of the degraded signal to noise ratio due to the lowering atom number (see Section 3.2.4). However, with the implementation of the 2D-MOT, this regime should be attainable, and clock stabilities below 5×10^{-16} at one second should be well within reach.

4.4   Study of the Detection Noise

In practice, the stability of the clock may not be limited by one of the sources of noise discussed before, but rather by technical noise, either impacting the atoms themselves (for example, magnetic field noise impacting the clock frequency noise via the Zeeman effect), or most commonly through the detection process. In this section, we want to characterize the noise coming from the detection, and gauge how far we are from operating in a regime where the detection noise is quantum-projection-noise limited. A preliminary discussion of the detection and the atom number calibration was done in Chapter 1 from geometrical and ray optics considerations. However, using the atomic signal, and more specifically by relating the detected atom number to the noise affecting the transition probability, it is possible to realize an absolute characterization of the signal to noise ratio of the clock as a
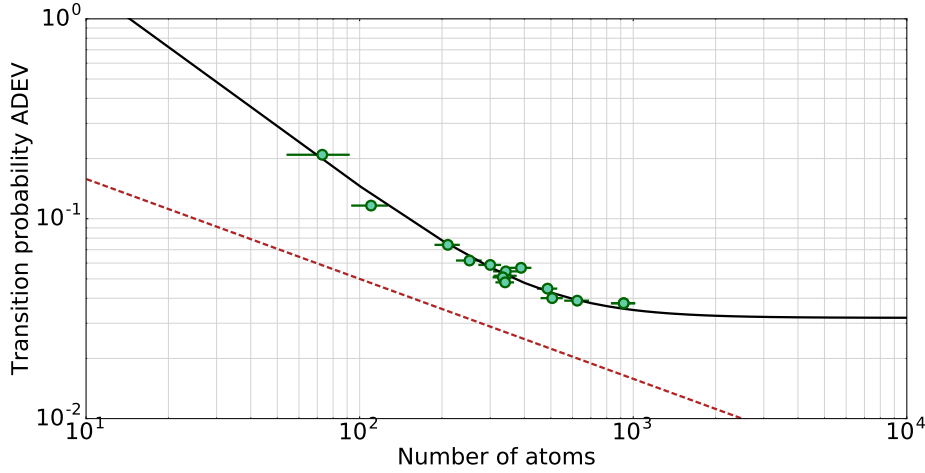
Figure 4.9. *Allan deviation at one second of the transition probability as a function of the detected number of CCD counts (green dots). The horizontal error bars are the standard deviation of the atom number for each measurement run. This measurement uses the normalized detection scheme described in Section 3.2.3. The dashed red line is the expected scaling of the quantum projection noise, and the black line is a fit to the model of Equation 4.6.*

function of the atom number. The advantage of this characterization is twofold:

- It allows us to devise the best working point for the clock using as a criterion the signal to noise ratio of the detected atomic signal and as a tuning parameter the number of atoms loaded into the MOT, which directly impacts the clock cycle time and therefore the clock stability.

- Provided that the technical detection noise is low enough, if we can identify a region in which the fluctuations of the transition probability as a function of atom number is limited by the quantum projection noise, then the scaling is exactly $1/\sqrt{N}$ where N is the number of atoms, which provides us with the calibration coefficient relating the detected signal (fluorescence CCD counts) to the number of atoms. This calibration is very relevant in view of the estimation of the density shift affecting the clock transition.

One such measurement is shown on Figure 4.9. We use the calibration factor found in Section 1.5 of 0.09 atoms/CCD count with a modified EM gain of the CCD of 1500 for this particular measurement yielding

a conversion factor of 0.0063 atoms/CCD count. This gives us a starting point to estimate the number of detected atoms. In order to do the measurement, the clock sequence is run on one of the two Zeeman components by applying a resonant $\pi/2$ pulse of the clock light, and gather statistics on the transition probability by staying at resonance. This allows us to be sensitive to the impact of atom number fluctuations on the transition probability, while being free of frequency noise (both LO and atom related), at least to first order. Indeed, at resonance the derivative of the transition lineshape as a function of frequency is zero (see lineshapes in Chapter 3). The number of atoms is varied by changing the duration of the MOT loading (for the curve shown above, the loading was varied between 0.15 and 1.0 seconds).

The experimental points (in green) are fitted with the model of Equation 4.6 (black full line). The portion going down as $\sqrt{N_{counts}}$ (red dashed line on the graph) is the expected quantum projection noise. We see that around 5×10^3 detected atoms, we lie close to a factor of 2 above the QPN because of noise coming from the detection. From the fit parameters, we estimate that the background noise of our detection system without atoms corresponds to 14 atoms.

This measurement suffers from two potential limitations:

- Long term drifts of the ultra-stable laser can bring the laser out of resonance from the atomic transition in the course of the measurement. We have therefore carefully updated the drift rate of the dedrifting DDS of the clock laser before each measurement run in order to mitigate this effect.

- Intensity fluctuations of the probe laser light are indistinguishable from atom number fluctuations, and can bias the interpretation of the results.

4.5   Estimating the Mercury Clock Stability Without Referencing to a Second Optical Clock

In this section, we will discuss the experimental evaluation of the stability of the mercury clock. The only way to evaluate the stability of an oscillator is usually to compare it to another more stable reference. However, in our case this second reference might not be available

as it would mean either building a second mercury clock, or using a complicated infrastructure to compare the mercury clock with another optical clock, which we will do later. Nevertheless, several measurements can be performed to evaluate the stability of the clock without the need for a second clock (see Section 5.1.1). We will also show how this short-term stability can be optimized with respect to the clock cycle parameters, as outlined in the previous sections.

4.5.1 The atoms against the ultrastable cavity

As the ultra-stable cavity employed to stabilize the clock laser has a frequency flicker noise limit of 4×10^{-16} (see Section 1.4.1), the short-term instability of the frequency of the lattice-trapped atoms clock transition can be determined by comparing the frequencies of the clock laser and that of the clock transition (as long as it higher than the instability of the laser, which is still the case for the mercury clock below $\simeq 10$ seconds of averaging time). The frequency difference between the two is given by the frequency correction applied to the AOM to keep the clock laser at resonance with the atomic transition

Therefore, if we look at the Allan deviation of the frequency fluctuations of the correction, we obtain a curve which carries information about the combined frequency instability of the ultra-stable cavity, and the atoms used as a frequency discriminator.

This stability is shown of Figure 4.10: After removing the linear drift from the ultrastable cavity, we observe a stability at one second of 1.3×10^{-15} (blue curve) [101], which is representative of the clock (i.e. the atoms) stability, a factor of two above the expected fundamental limit (combination of Dick effect and QPN), meaning that we still have some remaining technical noise, probably coming from the detection. This stability is a factor of 4 better than the previous record of our experiment [63].

This measurement also provides a characterization of the noise of the ultrastable cavity, since the instability goes down as $1/\sqrt{\tau}$ before hitting the laser flicker frequency noise floor of 4×10^{-16}, very close to the value expected from the beating of our laser with a similar system [71].

On last piece of information can be extracted by looking at the splitting of the two Zeeman components, shown in red on the plot, which
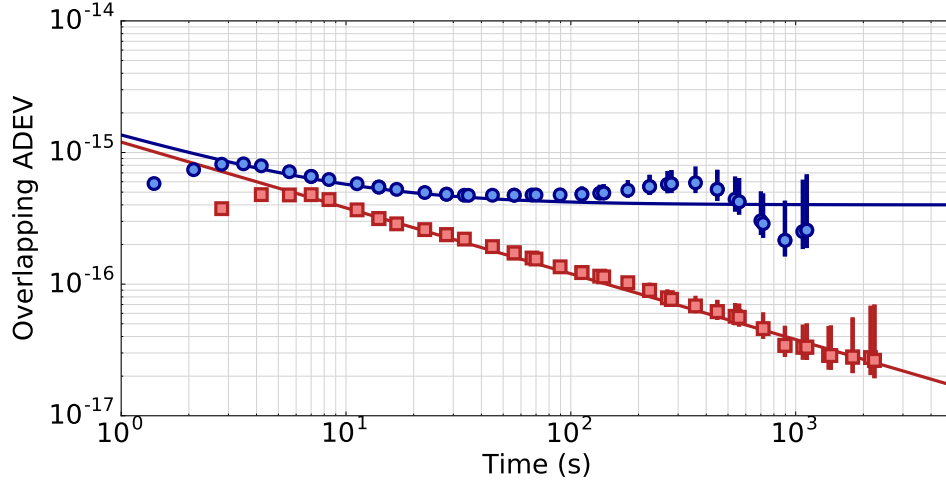
Figure 4.10. *Overlapping Allan deviation of the in loop correction signal sent to the probe laser AOM to keep it at resonance with the atoms. The blue curve shows the dedrifted data (linear drift removed), and the red curve is the deviation of the frequency splitting between the two Zeeman components. The blue line shows a model corresponding to a short term stability of 1.3×10^{-15} at 1 second, going down as $1/\sqrt{\tau}$ and flickering at 4×10^{-16}, consistent with the laser noise model of Equation 4.15.*

averages down as $1/\sqrt{\tau}$ below the flicker of the cavity, since the laser noise is in common mode for both Zeeman transitions. As we have seen in Section 3.2.1 the measurement of the Zeeman splitting provides us with an in-situ calibration of the magnetic field at the position of the atoms. With a statistical uncertainty of 5×10^{-17} in 1000 seconds (red trace), we can infer a potential resolution of 18 nT for the magnetic field, knowing the linear Zeeman coefficient 3.1(2) Hz/μT. In reality, in order to reach such a resolution the vector shift due to the lattice light laser field on the atoms would need to be taken into account and corrected.

4.5.2   Stability for systematics evaluation

When performing differential measurement, two independent servo loops are run in an interleaved fashion on a time scale of 5 to 10 seconds, and the quantity of interest is the difference between the corrections of the two integrators. Since we spend twice less time interrogating each loop, the stability on the difference should degraded by a factor $2\sqrt{2}$. This is an important factor that needs to be taken into account and characterized for the study of systematic frequency shifts,

since we want to reach a statistical resolution of 10^{-16} below on the measurements of the clock frequency shifts, which means that the averaging time of the measurements must be set accordingly.
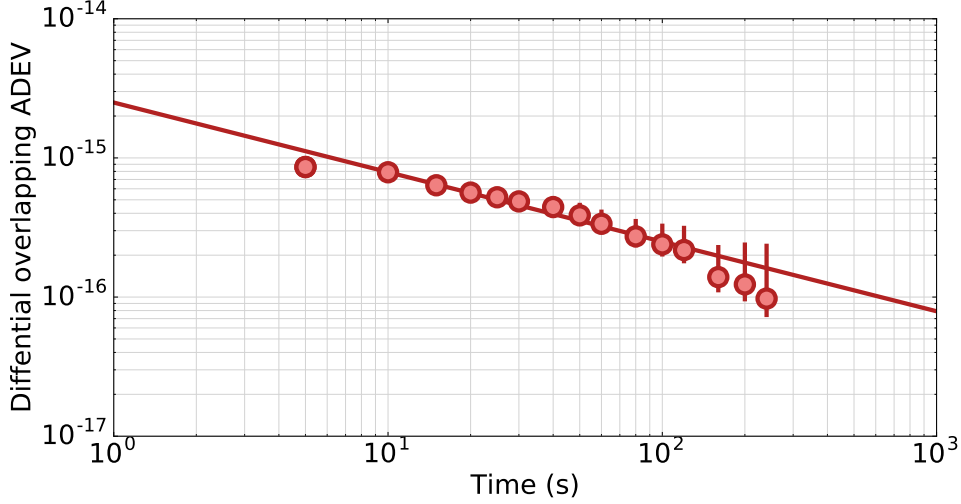
Figure 4.11. *Overlapping Allan deviation of the frequency difference of the correction for the two integrators. The red line starts at 2.5×10^{-15} and goes down as $1/\sqrt{\tau}$.*

A typical stability curve when performing differential measurements of lattice light-shift with a 5 cycles interleaving is shown on Figure 4.11. We see that the stability goes down starting from 2.5×10^{-15} at one second of averaging time, which is roughly a factor $\sqrt{2}$ higher than the single-integrator stability, and averages as $1/\sqrt{\tau}$ where τ is the integration time. The difference between the observed factor $\sqrt{2}$ increase in instability for the differential measurement and the predicted factor $2\sqrt{2}$ is attributed to improved experimental conditions for Figure 4.11 with respect to Figure 4.10. We therefore prove here that we can reach a statistical uncertainty below 10^{-16} in 1000 seconds of averaging time ($\simeq$ 20 minutes), which makes measurements of systematics at the 10^{-17} level within reach with reasonably long averaging times of a few hours.

4.6   Stability of a Two-Clocks Comparison: Correlated Interrogation

Atomic clock comparisons are essential tools of frequency metrology (see Chapter 6). When comparing two clocks, the same diagnostic

tools that we have developed in the previous sections for one clock still hold, and the instability of the ratio of the clock frequencies, which is the quantity that we want to measure is an important parameter of the comparison, which we want to optimize. In this Section, we study a technique to reduce the noise of atomic clock comparisons, which is the synchronous operations of both (or more) clocks being compared using a shared interrogation laser. In this regime, all sources of common mode noise, including Dick noise are greatly suppressed.

4.6.1 Principle of correlated interrogation

Interrogation between two clocks is most commonly performed when comparing two clocks based on the same atomic species [102].

In that case, one can use the same local oscillator to interrogate both clocks. Therefore, all sources of noise related to the clock laser will be common mode for both servos, and will drop out in the comparison, except for the Dick effect, if the two clocks are interrogated with random synchronization. However, if it is possible to operate the two clocks in a synchronous fashion (both clock cycles are of equal duration and both atomic ensembles are probed and detected at the same time), then the Dick effect also becomes common mode to the ratio measurement and is greatly suppressed [74].

The degree of correlation is conveniently visualized by plotting the transition probability for one clock as a function of the transition probability for the other. For two perfectly uncorrelated clocks, this plot will show a disk, while for two correlated clocks, it will show an ellipse, whose ellipticity is a measure of the degree of correlation.

In our case, we want to perform correlated interrogation between the mercury clock and the strontium clock, which is a much more difficult task since both clocks work at very different and incommensurable wavelengths (the ratio of the frequencies is close to 2.6, see Chapter 6). A very elegant solution to tackle this problem is to use a frequency comb to bridge the frequency gap and provide a nearly perfect transfer oscillator to copy the noise of one clock laser onto the other, to reproduce a situation in which a single laser is used to probe both clocks.

4.6.2 Transfer of spectral purity via the optical frequency comb

Transfer of spectral purity using an optical frequency comb (OFC) was demonstrated by Nicolodi et al. [76] in 2014, and is a very powerful technique, which allows one to share the frequency stability of any lasers whose carrier frequency lies inside the comb locking bandwidth and transfer it to one or several other lasers operating at any desired frequency inside the bandwidth of the frequency comb.

The original goal is to transfer the good spectral properties of a laser A working at frequency ν_A to a laser B working at frequency ν_B, such that the difference between ν_A and ν_B makes it impossible to do so by beating the two systems.
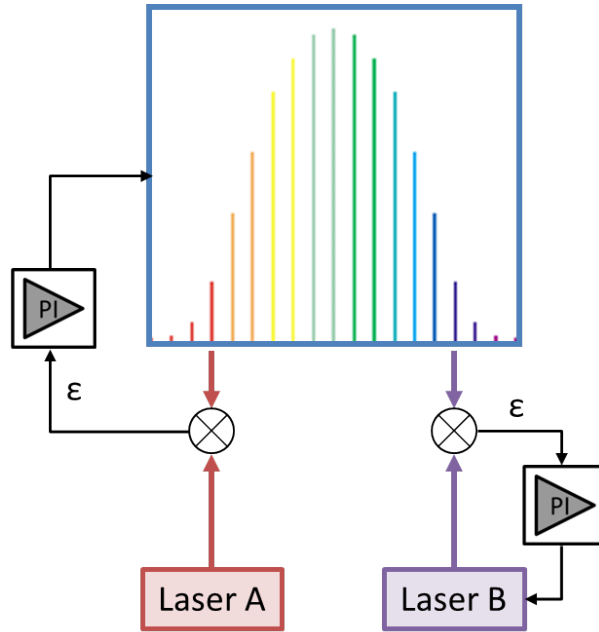
Figure 4.12. *Principle of the transfer of spectral purity via an optical frequency comb. PI: Proportional Integrator, ϵ: error signals.*

One possible implementation, as shown on Figure 4.12, is to phase-lock tightly the frequency comb onto laser A, and then beat laser B with the comb and use the beatnote to phase-lock laser B to the comb.

One great advantage of the frequency comb is that the relative frequency fluctuations between different comb teeth lies well below the 10^{-17} level, which means that the spectral purity transfer can work with any currently existing state-of-the-art ultrastable lasers.

In our case, the locking scheme is a bit different: The comb is
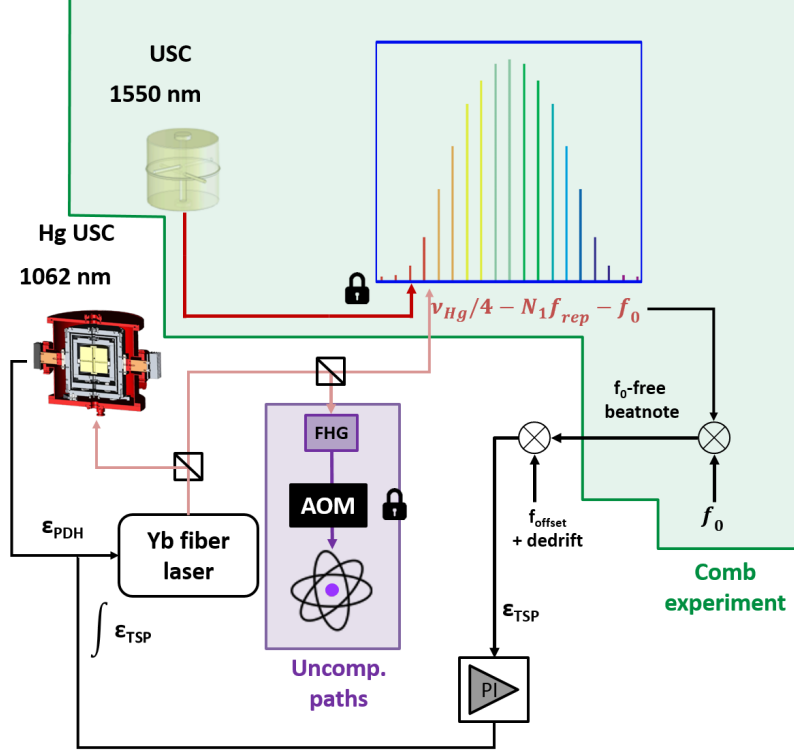
Figure 4.13. *Experimental setup for transfer of spectral purity via the optical frequency comb. ϵ_{PDH}: error signal for PDH locking, ϵ_{TSP}: error signal for the transfer of spectral purity, FHG: Fourth Harmonic Generation. The uncompensated path is shown in violet.*

tightly locked onto an ultra-stable cavity which we will call "CUS" (french for Ultra Stable Cavity), which has a flicker frequency noise floor of 10^{-15} and a central wavelength of 1.5 μm, and we transfer the spectral purity of this laser via the OFC to the mercury laser and to the strontium laser. The reason behind this choice is related to the requirements of the measurement chain that is used, among other things, for sending the optical fiber link to Strasbourg and London (see Chapter 6), and it is therefore beyond our control.

One might argue that using a clock laser with higher noise should degrade the performance of the two optical clocks. However, since performing transfer of spectral purity in this way we end-up copying the noise of the CUS onto both lasers, when measuring the frequency ratio between the two clocks, this LO noise will be common mode, and therefore will not affect the differential stability of the clocks.

A general scheme of the experimental setup is shown in Figure 4.13. On the mercury side we have decided to react on the already existing PDH (Pound Drever Hall) lock to the mercury cavity to lock the mercury laser onto the comb. The light from the mercury clock laser at frequency ν_{Hg} is sent to the comb lab, and beat with a small amount of comb light onto a photodiode. The resulting beatnote at frequency $\nu_{Hg}/4 - Nf_{rep} - f_0$ is first mixed with f_0 to get rid of possible f_0 fluctuations, and then mixed with a synthesizer whose (fixed) frequency is matched to the f_0-free beatnote frequency. We then get a phase signal, which is fed to a PI (proportional-integral) and summed to the error signal of the PDH.

We expect that this noise cancellation will be effective and that the relative instability of the two clocks in this configuration will mainly be set by the contribution to the Hg clock laser noise of the two frequency-doubling stages and the residual uncompensated path going to the atoms of approximately 2 meters (Shown in violet on the scheme of Figure 4.13).

I have chosen the bandwidth of the lock to be close to 10 Hz, small with respect to the available frequency range of the PDH lock, but big with respect to the clock cycle time, in order to be sure to copy the CUS noise relevant for short timescales ($\simeq$ 1 second) stability.

4.6.3   Correlated interrogation - experiments

We now look at preliminary results of frequency ratio measurements ν_{Hg}/ν_{Sr} using the scheme presented in the previous sections. In this section, we will overlook clock accuracy, which will be the focus of the last two chapters, and focus solely on the clock stability.

In order to make sure that the measurement is indeed synchronous, we send to the Sr lab the clocking signal of the National Instrument board that is used to control the experimental sequence, as well as the physical clock laser pulse recorded with a photodiode located after the lattice build-up cavity and a trigger pulse corresponding to the beginning of each cycle of the clock. Care is taken to temporally match the clock laser pulses and keep them synchronized during the measurement.

We can first look at the stability of the in loop frequency correction applied to the clock AOM in order to keep it at resonance with the

atoms, when the mercury laser is locked to the CUS. The overlapping Allan deviation of the frequency correction is shown on Figure 4.14 (a) as a function of the cycle time of the clock.

We see that even though the CUS is actively dedrifted by comparing the microwave from the frequency comb to the H-maser drift, the drift of the CUS is dominating the instability of the clock, even at very short timescales of $\simeq 1$ second, preventing us from seeing the impact of the servo-locking to the atomic transition.

In order to extract the stability of the correlated interrogation, we need to correlate the transition probabilities p_{Hg} and p_{Sr}. Indeed, physically this is where the correlation lies since fluctuations of the clock laser will induce fluctuations of the transition probability scaled by the sensitivity function [107]:

$$\delta p = \pi \int_0^{T_C} \delta f(t) g(t) dt \tag{4.16}$$

Using the transfer of spectral purity as explained in Section 4.6.2, both clock laser will have the same fluctuations (within the bandwidth of the locks, and scaled by the ratio of the clock frequencies) and the noise on the transition probabilities will become correlated.

Figure 4.14 (b) shows the Overlapping ADEV of the transition probability for the mercury clock when the transfer is active. We again see that without adding the information of the Sr clock, the CUS noise dominates completely. The inset shows the corresponding time-trace of the frequency excursion.

We can now look at the measurement of the frequency ratio when both atomic samples are referencing the same LO, and use the information of the correlation to improve the stability of the measurement. The time-traces are shown on Figure 4.15 (a). We observe a clear correlation between the blue trace (Hg clock) and the orange trace (Sr clock), meaning that the transfer of spectral purity is working as expected. In order to be able to compare the trace one-to-one, the frequency correction to the Sr laser has been rescaled to account for the frequency ratio between the two clocks.
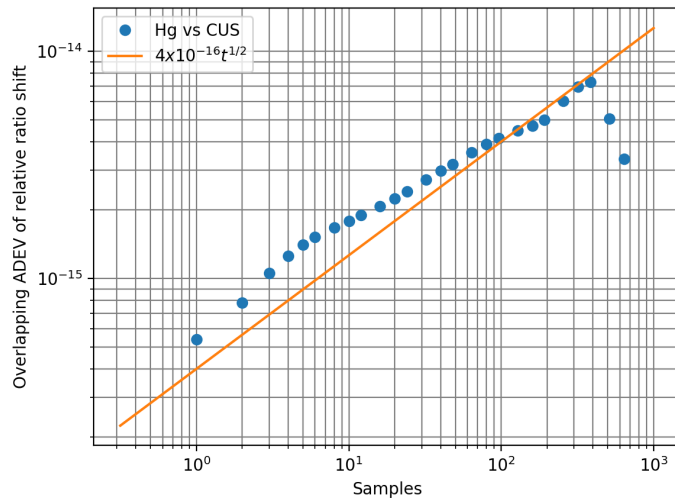
(a)
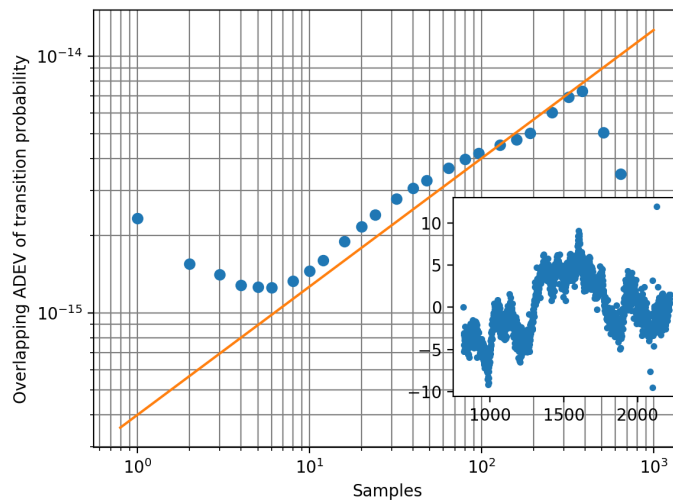
(b)

Figure 4.14. *(a) Overlapping Allan deviation (ADEV) of the clock frequency correction using the CUS as LO and (b) the corresponding Overlapping ADEV of the extracted transition probability.*

The impact of the synchronous operation on the stability of the frequency ratio measurement is shown on Figure 4.15 (b). At short timescales, the noise of the LO dominates and cannot be perfectly rejected by the correlated interrogation. However, after 100 seconds, the atomic servo lock has relaxed and the Overlapping ADEV is consistent with white noise going down as $3 \times 10^{-15}/\sqrt{t}$.

The stability of the ratio measurement is marginally better than the stability obtained when performing uncorrelated measurements locking each clock laser on its own LO (see Section 6.4), while the CUS noise is much worse than either the mercury or the strontium cavities.

The conclusion of this first experiment is therefore that the transfer of spectral purity does significantly improve the stability of the ratio measurement, but the CUS instability is too high to be completely eliminated by the spectral purity transfer scheme.

To improve on this measurement, the first step would be to lock the Comb on the mercury or strontium ultra-stable cavities which have better noise properties than the CUS, and do the purity transfer as described here. Thanks to the study and experimental proof of principle described here, this measurement is already possible and planned in the near future.

On the long term, it is planned to replace the CUS by a long cavity with flicker floor at the 10^{-16} level or below, which would automatically improve the frequency ratio measurement stability below the 10^{-16}, allowing optical-to-optical clock comparison at the 10^{-18} level in only three hours of averaging time.
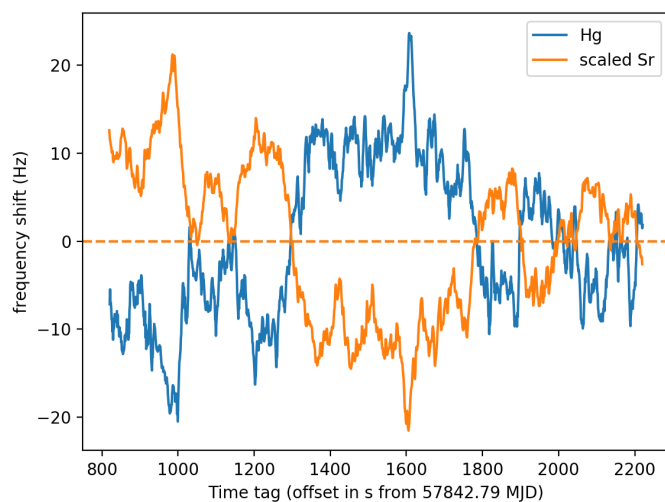
(a)
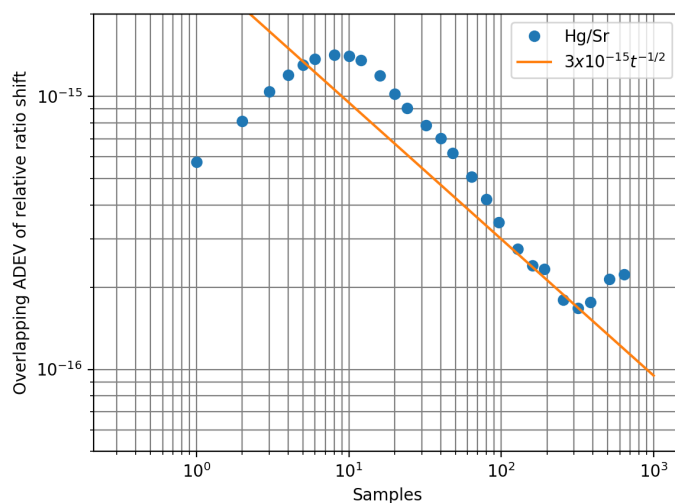
(b)

Figure 4.15. *(a) Time-trace of the frequency corrections applied to the clock AOMs during synchronized measurement and (b) Stability of the synchronous frequency ratio measurement.*

Chapter 5

Ascertaining the Mercury Clock Uncertainty Beyond the SI Second Accuracy

The definition of an atomic frequency standard always refers to an isolated unperturbed atom in its own rest frame.

In practice, even in a laboratory environment, there are many physical mechanisms which can perturb the frequency of an atomic transition, comprising thermal radiation, electromagnetic fields, atomic interactions.

In this chapter, I will describe how these perturbations can be measured, evaluated and reduced. For some perturbations, we can find experimental protocols to reduce the impact on clock accuracy. Whenever the complete cancellation of a perturbation is impossible, it needs to be evaluated in terms of clock frequency shifts, and the corresponding frequency correction applied when comparing with another frequency reference.

5.1 Clock Accuracy

Frequency standards are chosen among elements possessing at least one transition which is very weakly coupled to these external perturbations, such as the $^1S_0 \rightarrow {}^3P_0$ transition in ^{199}Hg.

However, this insensitivity to external fields must be experimentally investigated and quantified in order to build an accurate and repro-

ducible frequency standard. In more mathematical terms, we want to evaluate the parameter ϵ of Equation 2, called the accuracy of our clock, which we have neglected up to this point.

This is important, firstly because well characterized frequency standards periodically steering flywheel oscillators such as H-masers are the basis for our current timescale [86], [97].

Also, a well characterized and accurate standard can act as a secondary representation of the SI second [32], [52], and therefore participate to the realization of TAI (International Atomic Time). Thanks (in part) to the work presented in this thesis, in 2017, the Consultative Committee for Time and Frequency (CCTF) has recognized the ^{199}Hg $^1S_0 \rightarrow ^3P_0$ clock transition as a Secondary Representation of the Second (SRS).

Finally, assessing the frequency of the mercury clock and carefully estimating the associated uncertainty is a necessary step for future frequency comparisons with other optical clocks and measurements of frequency ratios beyond the realization of the SI second.

During my PhD work, we have conducted two measurement campaigns, in 2015 and 2017 to establish the accuracy of the mercury clock.

5.1.1 Digital lock-in technique for studying systematics

In order to study the physical effects affecting the clock transition, we use a technique akin to Digital Lock-In detection. We run several independent integrators in an interleaved fashion, and for each integrator we set a different value for a clock parameter, and then analyze the frequency difference between the corrections applied to each integrator to extract useful information about the impact of this parameter on the clock transition frequency. Let us see how this work if we take the example of collisional shift: we want to see how a change in the atomic density affects the clock frequency.

We run two interleaved integrators in parallel, one for which the atomic density is higher, as obtained by increasing the loading time of the atoms in the lattice, and the other one for which the atomic density is lower. Aside from the modulated atomic density, the atomic servos operate in the same conditions. Each integrator is run for a few cycles of loading/probing/detection, and then the other one is run for a few
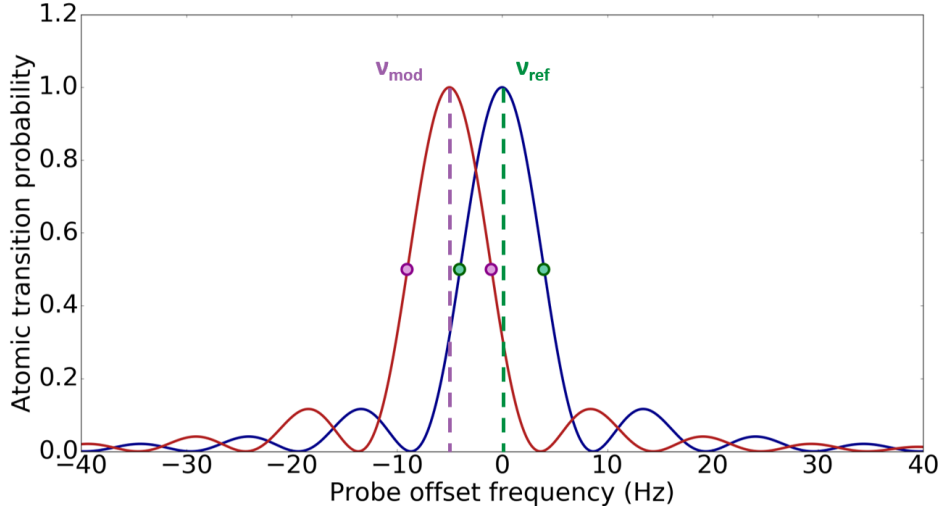
Figure 5.1. *Principle of interleaved systematics measurements: we want to measure the frequency difference between the clock transition for a reference configuration ν_{ref} (blue spectrum), and a configuration with a modulated parameter ν_{mod} which shifts the atomic resonance by a small amount $\delta\nu = \nu_{\mathrm{ref}} - \nu_{\mathrm{mod}}$ (red spectrum), and study this difference as a function of the modulation strength.*

cycles, and the procedure is repeated.

Interleaving in a sufficiently fast manner the integrators allows for common mode rejection of long term stationary noise processes, such as local oscillator linear drift or atom number fluctuations, and allows us to extract information about the specific physical effect that we wish to study provided that the quantity that we are interested in asymptotically converges towards its average value at long timescales.

However, we need to leave time for the servo loops to relax, so each integrator must stay on for several cycles. In the end, we find that interleaving every 10 clock cycles yields a good compromise.

Looking at the correction applied to the frequency shifter (AOM) used to keep the laser at resonance with the atoms, and more specifically the difference in the correction for both integrators, we are able to extract the frequency shift associated with the modulation of the atomic density, and doing so for several different atomic densities, we are able to do a systematic study of this effect.

This technique is very general and was used for the majority of frequency shift measurements featured in this thesis. However, it becomes useless when the physical effects we want to measure cannot

be changed rapidly with respect to the duration of a clock cycle, as is the case of the BBR shift for example. For those effects, we will see that other schemes have to be devised to estimate and control the frequency shifts (see e.g. Section 5.6.2).

5.2   Collisional Shift

Collisional shift or density shift arises due to interactions between cold atoms in the lattice trap. It is the main limitation to the accuracy of the best Cs and Rb [33] microwave frequency standards and has been observed in both Sr [9] and Yb [55] optical lattice clocks.

5.2.1   Theoretical introduction

In quantum mechanics, the collision between two particles is treated as a problem of scattering of the incoming particle's wavepacket $\phi(r)$, usually modeled as a plane wave, on the potential $V(r)$ created by the interaction with the other particle. The Hamiltonian describing such and interaction for two cold atoms is:

$$H_{coll} = \frac{p_1^2}{2m} + \frac{p_2^2}{2m} + V(r_1 - r_2) \tag{5.1}$$

where r_i and p_i are the position and momentum operators of the particles and V is the potential associated with Van der Waals interaction, characterized by a $1/r^6$ dependence.

The approach commonly followed for low energy scattering events, such as cold atoms collisions in a dilute gas, is the partial angular-momentum wave expansion. The scattered wavefunction is first decomposed into two components: the first component is the incident unscattered plane wave, and the second is a sum of scattered, outgoing spherical waves with different angular momenta l:

$$\phi(r) = e^{ik.r} + \sum_l^\infty f_l(k, \theta, \phi) \frac{e^{ikr}}{r} \tag{5.2}$$

where the angular dependence of $f_l(k, \theta, \phi)$ depends on the exact shape of the potential $V(r)$.

In the case of fermions cooled to tens of μK level temperatures, we will only consider the lowest angular momentum waves, namely even s-wave collisions ($l = 0$), and odd p-wave collisions ($l = 1$), since higher

angular momenta processes are "frozen-out" by the centrifugal barrier [51].

We now want to make the link between Equation 5.2 and the frequency shift associated with atomic collisions. The effect of the potential is to introduce a dephasing of the out-going partial wave with respect to a spherical wave. This dephasing, in the limit of low energy collisions is characterized by a single constant real parameter, the scattering length a_{ij} which depends on the internal states of the two colliding atoms $|i\rangle$ and $|j\rangle$. In that case, the interatomic interactions modify the total energy of the cold-atoms cloud by an amount [16]

$$E_{int} = \frac{4\pi\hbar^2}{m_{\mathrm{Hg}}} \times a_{ij} \times n \times N_{at} \tag{5.3}$$

where n is the atomic density and N_{at} the number of atoms. When operating the clock, we apply a pulse of light which transfers the total atomic population from $|e\rangle$ to $|g\rangle$ (see Section 3.1.2 for more details), corresponding to the absorption of N_{at} UV photons of energy $\hbar\omega_{at}$. The difference in energy between these two situations is then

$$\Delta E_{int} = \frac{4\pi\hbar^2}{m_{\mathrm{Hg}}} \times (a_{gg} - a_{ee}) \times n \times N_{at} \tag{5.4}$$

and by energy conservation considerations, this difference must be equal to $N_{at} \times \hbar(\omega_{at} - \omega_{ge})$ where ωge is the energy corresponding to having the atoms in the excited state with no interaction. We can then finally write the frequency shift associated with atomic interactions in our simple picture

$$\Delta\nu_{int} = \nu_{at} - \nu_{ge} = \frac{2\hbar}{m_{\mathrm{Hg}}} \times (a_{gg} - a_{ee}) \times n \tag{5.5}$$

In the general case, the shifts associated with s and p-waves collisions can be written in the mean field approximation by respectively [36]:

$$\Delta\nu_{eg}{}^{s-wave} = \frac{2\hbar n}{m_{\mathrm{Hg}}} g[a_{gg}\rho_{gg} - a_{ee}\rho_{ee} + (\rho_{ee} - \rho_{gg})a_{eg}] \tag{5.6}$$

and

$$\Delta\nu_{eg}{}^{p-wave} = \frac{\pi\hbar n}{m_{\mathrm{Hg}}} \langle k_T{}^2\rangle[v_{gg}\rho_{gg} - v_{ee}\rho_{ee} + (\rho_{ee} - \rho_{gg})v_{eg}] \tag{5.7}$$

where ρ_g (ρ_e) is the ground (excited) state population fraction, n is the atomic density, m_{Hg} is the atomic mass of mercury, a_{ij} (v_{ij}) is the scattering length (volume) parametrizing collisions between 2 particles in

the $|i\rangle$ and $|j\rangle$ internal states, $\hbar^2\langle k_T^2\rangle/m_{\mathrm{Hg}}$ is the average collision energy and g is the two-particle correlation function at zero separation, which is simply a constant in the case of coherent transfer of population conserving spatial correlations such as is the problem under study.

In order to control this shift, several techniques have been implemented. The first method makes use of transfer of population between the two clock states by adiabatic passage to prepare samples of cold atoms with precisely defined ratios of atomic density and atom number [82] in order to very accurately (at the 10^{-3} level) measure the cold collision shift. Another method has been to use higher dimensional lattice such as a 2D lattice to increase the interactions between cold atoms, resulting in a interaction-induced reduction of the frequency shift [104] analogous to dipole blockade in cold Rydberg gasses [60]. Fortunately, in our particular case, several factors should contribute to the suppression of atomic collisions:

- We are working with low densities (as compared to a typical optical lattice clock experiment) corresponding to less than three atom per site on average.

- We are working with a very pure nuclear spin polarized sample of **fermionic atoms**, therefore Pauli's exclusion principle should forbid s-wave collisions from taking place.

- Low atomic temperatures freeze-out odd-wave collisions

However, s-wave collisions have been observed in atomic samples of spin polarized fermions [9], when interrogation inhomogeneities render the fermions mutually distinguishable, in which case Pauli's exclusion principle doesn't hold anymore [26].

We have decided to start with the study of the collision shift because this effect scales with atomic density, and can therefore impact and bias the measurement of other systematics. For example, measuring the lattice light-shift implies varying the trap depth, which can modify the atomic density in the trap. We therefore want to make sure that atomic density shift is not a problem at our highest operating atomic density.

5.2.2 Experimental results

Experimentally, it is difficult to measure accurately, and therefore precisely control the atomic density, and we have to estimate it based on the atom number. However, given the MOT density and the lattice temperature, we estimate that the density scales linearly with the number of atoms in the lattice. We have used two different methods to modulate the probed atom number between what we call a high density (HD) and a low density (LD) configuration in order to evaluate the collisional shift.

In a first series of measurements, we modulated the duration of the clock laser state selection pulse duration (see section 2.4), while keeping the power constant, thereby changing the fraction of atoms excited to the $^3P_0$ state. We then try to fit the data with a linear model. The results are presented on figure 5.2 (a).

In order to check for the presence of a bias in this technique such as a phase transient in the AOM used to shape the state selection pulses or a nonlinear change in the density distribution with the atom number, we performed a second series of measurement by varying the loading time of the MOT. The results are shown in figure 5.2 (b).

Table 5.1 shows the results for the two methods, extrapolating the shifts to our nominal operating atom number of $\simeq$900 atoms probed in the lattice.

Method:	Loading	State sel. pulse	Combined
Slope (10^{-20}/atom)	-2.6	-20	-6.5
1σ uncert. (10^{-20}/atom)	8.8	16	7.8
Correction (10^{-17})	-2.1	-16.2	5.2
1σ uncert. (10^{-17})	7.1	14.0	6.4

Table 5.1. *Results of collisional shift measurements for the two methods used to vary the atomic density: the MOT loading time, and the state-selection efficiency. We extract the slopes (collisional shift coefficients expressed for one atom) for both methods and the combined data from the fits of Figure 5.2 with the quoted uncertainty coming from the fit uncertainty. The frequency clock correction for both methods and the combined data is determined by using the collisional shifts coefficients and extrapolating to our operating atom number. The table is meant to be read horizontally.*

(a)

(b)
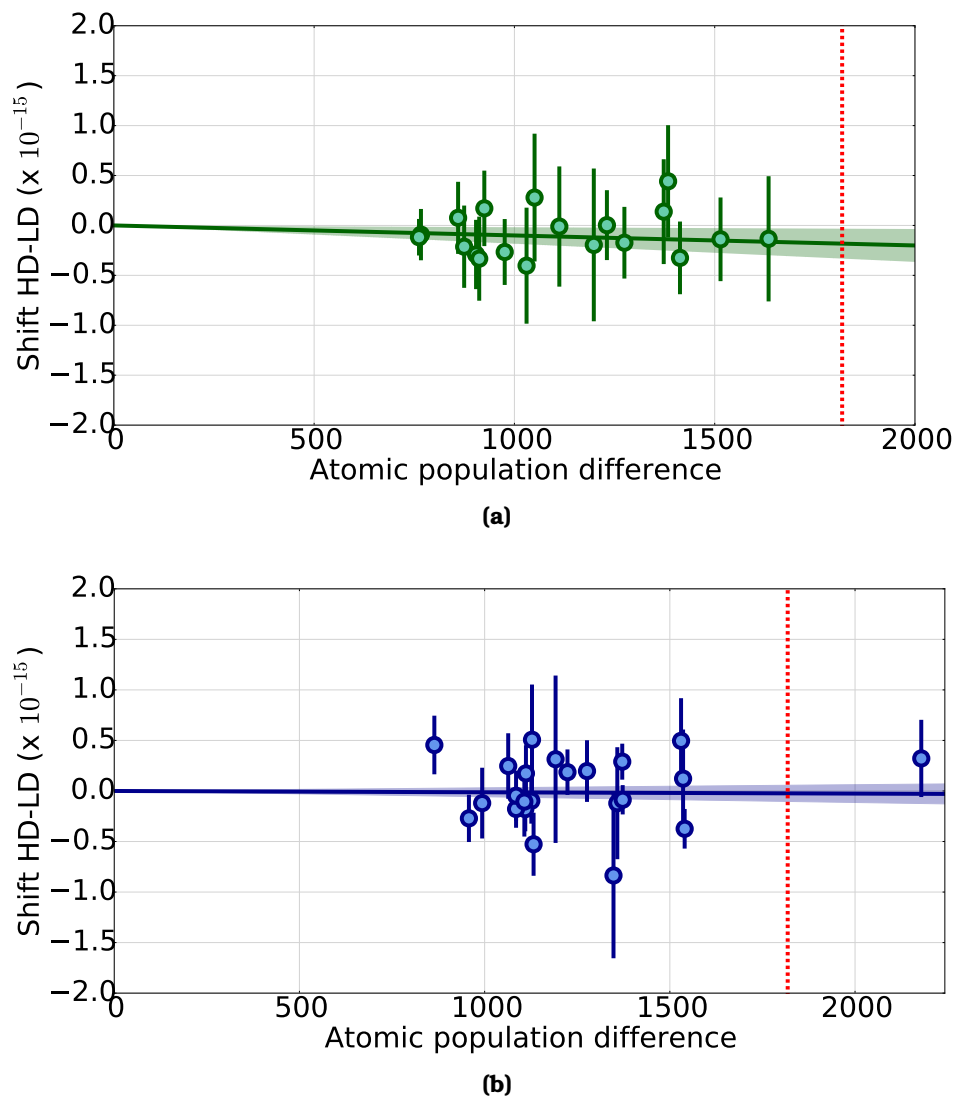
Figure 5.2. *Differential collisional shift shown in relative units as a function of the population difference for (a) the state selection time variation method and (b) the MOT loading time variation method. The data sets are fitted with straight lines with no offset, since the differential method must give zero shift at zero modulation of the parameters. The 1σ confidence interval is given by the shaded area on each curve. The vertical red dashed line corresponds to the number of atoms probed during typical clock operation, and allows for a graphical estimation of the residual shift in nominal configuration.*

We see that the extrapolated shift for the MOT loading time atom number variation method at our operating point is $-16.2(14) \times 10^{-17}$, and it is $-2(7) \times 10^{-17}$ for the state selection pulse length variation method, both compatible with zero at the level of uncertainty. Since we have no physical argument to favor one method over the other, we combine both datasets treating them as a single one. Fitting with a linear function, we find a frequency shift of $-5.2(6.4) \times 10^{-17}$ (or alternatively a clock correction of $5.2(6.4) \times 10^{-17}$), compatible with zero within a 1σ uncertainty. The results of this procedure are shown in the third column of Table 5.1.

Based on the results presented here, we conclude that collision shift is controlled at the mid 10^{-17} level even for the highest atom number that we can produce in our trap.

5.3   Lattice AC Stark-Shift

We will now consider the effect of the trapping light on the frequency of the clock transition, including a short discussion about high-order non-linear lattice shifts.

5.3.1   Linear shift

Trapping the atoms in a lattice allows for cancellation of Doppler and other motional effects, but it has the consequence of introducing an AC Stark shift on the clock levels, and in turn a frequency shift of the clock transition.

As first pointed out in [45], tuning the frequency of the trapping light to the so-called "magic frequency" ν_{magic} for which the scalar polarizabilities of the clock states are equal allows for a cancellation to first order of this frequency shift. Furthermore as ^{199}Hg has spin 1/2, the tensor component of differential polarizabilities are zero by symmetry.

Given the relatively small trap depth available in our experiment and the predicted value of nonlinear terms for mercury [44], we expect that nonlinear lattice shifts will not appear at our present resolution. We therefore first analyzed the data according to a linear model of the

lattice light shift (see [44]).

$$\Delta\nu_{LLS} = \frac{1}{h\alpha^S_{^1S_0}} \frac{\partial\Delta\alpha^S}{\partial\nu}\Big|_{\nu_{MOD}} (\nu_{lat} - \nu_{magic})U_{lat} = \frac{\partial\Delta\kappa^S}{\partial\nu}\Big|_{\nu_{lat}} (\nu_{lat} - \nu_{magic})U_{lat}$$

(5.8)

where $\Delta\alpha^S(\nu) = \alpha^S_{^3P_0}(\nu) - \alpha^S_{^1S_0}(\nu)$ is the difference between the values of scalar polarizabilities of the ground and excited states of the clock at the operating frequency of the lattice ν_{lat}, and U_{lat} is the operating depth of the lattice.

We study this effect using digital lock-in detection having two integrators running on each one of the π components of the clock transition at the nominal depth U_{REF} and a second pair of integrators running at a different depth U_{MOD}. Experimentally, U is estimated by monitoring the offset of the lattice sidelock to the buildup cavity, using the coefficient derived in Section 3.3.

Figure 5.3. *Lattice AC stark shift (Hz) as a function of the differential lattice depth in recoil energy. The detuning (in MHz) from 826 855 533 MHz corresponding to each curve is shown on the plot with matching color. The full lines show the result of a fit of the whole dataset with a linear model.*

During the first measurement campaign at the beginning of this thesis, we were working with U_{REF} = 56 E_{rec}, with U_{MOD} being varied between 50 and 25 E_{rec}.

By repeating these integrations for different lattice frequencies, we obtain the dataset plotted on Figure 5.3 as a function of the difference U_{REF} - U_{MOD}. In the figure we also plot a fit of the whole dataset with the function: $\Delta\nu = a(\nu_{lat} - \nu_{magic})(U_{REF} - U_{MOD})$ with free parameters

a and ν_{magic}.

From the fit, we extract the coefficient $a = \frac{\partial \Delta \kappa^S}{\partial \nu}(\nu_{magic}) = 1.25(7) \times 10^{-4}$ Hz/E_{rec}/MHz and an estimation of the magic frequency $\nu_{magic} = 826\ 855\ 539\ (21)$ MHz, an improvement by more than two orders of magnitude with respect to our previous determination [120] and in agreement with the measurement from [118].

We have then made a second measurement campaign with a gain of a factor of two on the lever arm thanks to the new Ti:Sa laser (see Section 1.3.1) by operating the clock with higher trap depths, calibrating the wavemeter every hour.

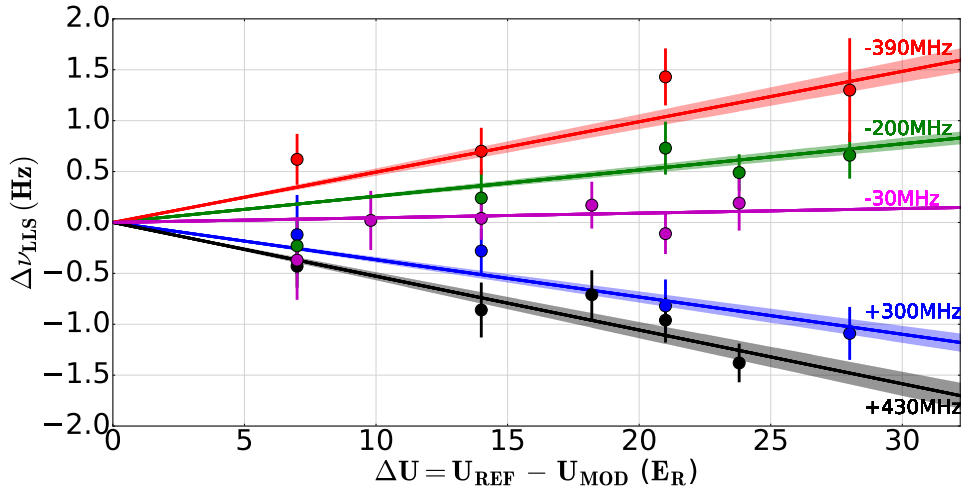The results are presented on Figure 5.4. We can note a signifi-

Figure 5.4. *Lattice AC stark shift (Hz) as a function of the differential lattice depth in recoil energy. The detuning (in MHz) from 826 855 533 MHz corresponding to each curve is shown on the plot with matching color. The full lines show the result of a fit of the whole dataset with a linear model.*

cant dispersion of the data-points confirmed with a χ^2 test yielding a 0.1 probability on the global fit to the data, which we attribute to frequency excursions of the wavemeter used to lock the Ti:Sa at the magic wavelength.

Nevertheless, we see that the greater lever arm would unable us to pinpoint the magic wavelength with an uncertainty of 7 MHz, more than a factor of three better than during the first campaign (21 MHz quoted above). However, the dispersion of the data points leads us to believe that frequency excursions of the wavemeter could introduce a potential bias in the measurement, and we therefore only use the

value of ν_{magic} determined during the first campaign.

We also get a second estimate of the coefficient $\frac{\partial \Delta \kappa^S}{\partial \nu}(\nu_{magic}) = 1.17(6) \times 10^{-4}$ Hz/E_{rec}/MHz in reasonable agreement with the coefficient extracted from the first campaign. We can note that this coefficient is in agreement with the one found by the RIKEN group of $1.1(3) \times 10^{-4}$ Hz/E_{rec}/MHz within the stated error bars [118].

Overall, we can estimate the shift and the associated uncertainty at our nominal lattice depth of 60 E_{rec}. Working at a detuning of -2 MHz from the measured magic wavelength to compensate the non-linear and linear shifts, we obtain a clock correction $\Delta \nu_{LLS}$ = -0.6 $\times$ 10^{-17} with an uncertainty of 5.1×10^{-17}, at the same level of uncertainty as the work of [118].

5.3.2 Vector shift

The vector light shift is given by [59]:

$$\Delta \nu_{VLS} = \alpha^V \frac{m_F}{2F} \xi \frac{E^2}{2h} = \kappa^V \xi E^2 \qquad (5.9)$$

where ξ is the degree of ellipticity of the lattice light field, κ^V is the vector light-shift coefficient, and E is the electric field.
The vector shift acts as a pseudo-magnetic field on the atoms, which means that we can measure its effect by studying the splitting between the two Zeeman components as a function of the trap depth (or equivalently lattice intensity).
Such a study, realized by interleaving configurations with different trap depth is shown on Figure 5.5. We observe the expected behavior, which is that the splitting increases linearly as a function of trap depth, because the vector shift creates the equivalent of a linear Zeeman effect on the two π components of the clock transition, whose strength depends on the amplitude of the trapping field at the position of the atoms.

From a linear fit to the data, we extract an effective vector light-shift coefficient for our clock, which encompasses the residual ellipticity of the lattice light, $\kappa^V_{(eff)}$ = 0.087(1) Hz/E_{rec}.

One important thing to note, is that this effect in independent of the detuning from the magic wavelength.

At our nominal trap depth of 60 recoils, the splitting between the two Zeeman components arising from the vector light-shift is 5.2 Hz.
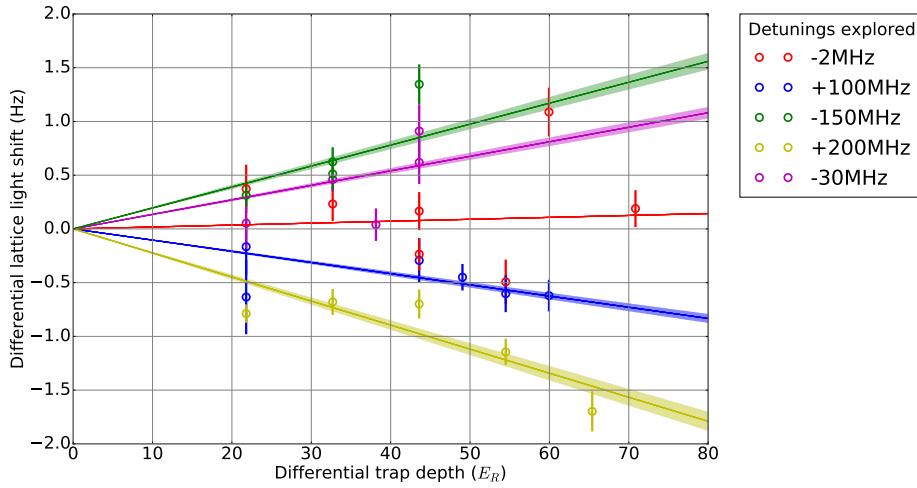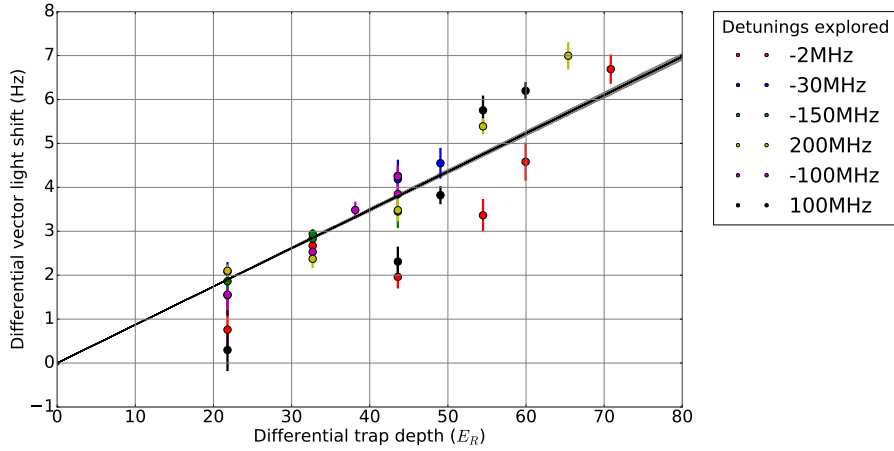
Figure 5.5. *Lattice AC differential vector stark shift (Hz) as a function of the differential lattice depth in recoil energy. The detuning (in MHz) from 826 855 533 MHz corresponding to each curve is shown on the plot with matching color. The black line shows the result of a fit of the data with a linear model, the shaded grey area is the 1σ confidence intervals on the fit.*

However, since this effect is strictly equivalent to a 1st order Zeeman shift on the transition, it is rejected when locking with the stretched servo on the two Zeeman components and is not an issue at our nominal uncertainty.

5.3.3 Higher order terms

A χ^2 test yields a probability of 0.96 for the linear fit of the first systematics measurement campaign, which gives us confidence that higher order terms are experimentally not resolved at our present level of uncertainty.

Nevertheless, when aiming for the 10^{-17} level accuracy, these have to be taken into account.

We evaluated the lattice light shift with the complete model presented in [44] using the theoretical estimation of coefficients of the nonlinear terms and our experimental determination of the linear ones.

In this model, the total lattice light-shift including non-linear terms

writes:

$$\Delta\nu_{LS} = \left(\frac{\partial\Delta\kappa_{E1}}{\partial\nu}\delta\nu - \Delta\kappa^{qm}\right)(2n+1)\sqrt{\frac{E_{rec}}{4\alpha_{E1}}}I^{1/2}$$
$$- \left[\frac{\partial\Delta\kappa_{E1}}{\partial\nu}\delta\nu + (\Delta\beta(\xi)/h)(2n^2+2n+1)\frac{3E_{rec}}{4\alpha_{E1}}\right]I \qquad (5.10)$$
$$+ (\Delta\beta(\xi)/h)(2n+1)\sqrt{\frac{E_{rec}}{\alpha_{E1}}}I^{3/2}$$
$$- \Delta\beta(\xi)/hI^2$$

$$\Delta\nu_{LS} = c_{1/2}I^{1/2} + c_1 I + c_{3/2}I^{3/2} + c_2 I^2 \qquad (5.11)$$

Where $\Delta\beta(\xi)$ is the polarization-dependent differential hyperpolarizability coefficient and ξ is the probe polarization ellipticity.

From this nonlinear model we generate datapoints at the values of detuning and lattice depth probed experimentally and perform a linear analysis in the same way as we do for the experimental data. We check then that the values of $\frac{\partial\Delta\kappa^S}{\partial\nu}(\nu_{magic})$ and ν_{magic} obtained are consistent with the experimental ones. At our operating working point of 60 E_{rec} we get a clock correction of $\Delta\nu_{non-lin.LLS}$ = -6 × 10^{-17} with an uncertainty of 4 × 10^{-17} assuming 10 % uncertainty on the theoretical non-linear coefficients.

5.4   Zeeman Shift

We will now deal with the effect of an external magnetic field on the clock transition, namely Zeeman frequency shifts.

The effect of an external magnetic field on the clock transition is to introduce a frequency shift on the π Zeeman components given by

$$\Delta\nu_{mag} = m_F g_F \mu_B B_z - \beta_Z B_z^2 \qquad (5.12)$$

where g_F is the g-factor of the transition, μ_B is the Bohr's magneton in frequency units, β_z is the 2nd order Zeeman coefficient and B_z is the projection of the field along the polarization of the probe beam.

The first step towards the measurements of Zeeman effects is to make sure that our magnetic field at the position of the atoms is well defined. To do so, we perform spectroscopic measurements on the clock transition, using the atoms as a magnetic probe (see Section 3.2.1).

5.4.1   Linear Zeeman effect

Once the magnetic bias quantization axis is sufficiently well defined, we can look at Zeeman shifts affecting the clock transition.

The linear (1st order) Zeeman effect is intrinsically rejected by our method of interleaved integration on the two Zeeman components, which I presented in Section 4.1.

However, the reading of the splitting of the two π transitions, which is twice the 1st order Zeeman shift, provides us with a very nice in-situ calibration and measurement of the value of the magnetic field at the position of the atoms, in order to estimate the 2nd order Zeeman effect. As we will see below, for a typical Zeeman splitting of 500 Hz, this calibration is valid to the % level (and not higher because of the vector shift of $\simeq 5$ Hz which biases the measurement).

5.4.2   Quadratic Zeeman effect

Similarly to the lattice light-shift case (see section 5.3) we perform digital lock-in detection running four independent integrators, one pair operating at a reference bias field B_{REF} and locking on each of the two π components, and another pair operating at a variable bias field B_{bias}, also on the two π components of the transition. For each integrator pair we then construct the two quantities:

$$\nu_m(B) = \frac{1}{2}[\nu_{mag}(\pi^+, B) + \nu_{mag}(\pi^-, B)] \tag{5.13}$$

$$\Delta\nu(B) = \nu_{mag}(\pi^+, B) - \nu_{mag}(\pi^-, B) \tag{5.14}$$

which are related to the relevant parameters of equation 5.12 by:

$$\nu_m(B_{bias}) - \nu_m(B_{REF}) = -\beta_z(B_{bias}^2 - B_{REF}^2) \tag{5.15}$$

$$\Delta\nu(B) = g_F\mu_B B + \Delta\nu_{VLS} \tag{5.16}$$

where $\Delta\nu_{VLS}$ is the vector component of the lattice light-shift, which is indistinguishable from the linear Zeeman effect.

A measurement of this last quantity can be obtained by analyzing the data presented in section 5.3 extracting the splitting between the two π components as a function of the lattice depth. At our nominal trap depth of 60 E_{rec} we obtain $\Delta\nu_{VLS} \simeq 5.2$ Hz $\ll \Delta\nu(B_{bias})$, indicating a residual ellipticity of the probe beam of about 3 % if we use the vector polarizability given in [35].

Now neglecting the vector light shift, we can use the measurement of $\Delta\nu(B)$ as an in situ calibration of the magnetic field and we get the quadratic Zeeman shift

$$\Delta\nu_{QZS} = \frac{\beta_Z}{(g_F\mu_B)^2}(\Delta\nu(B_{REF})^2 - \Delta\nu(B_{bias})^2) \qquad (5.17)$$

We plot in figure 5.6 the differential shift of the center frequency of the clock transition as a function of the difference of the square of the splittings for the two interleaved configurations.

We are able to vary the value of the bias magnetic field from 550 to 90 μT, which given the expected small sensitivity of the mercury transition to magnetic fields is currently limiting the accuracy of the measurement. From the slope of a fit to the data according to equation
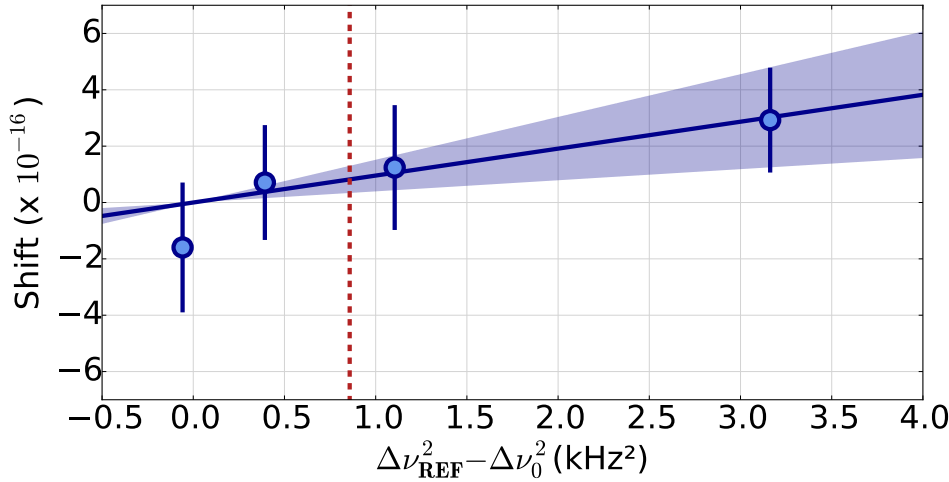
Figure 5.6. *Quadratic Zeeman shift as a function of the square of the splitting between the two π components. The plain black line is a linear fit to the data, and the shaded area represent the 1σ confidence intervals on the fit. The red dotted line is our nominal operating point.*

5.17, we obtain the atomic coefficient $\gamma_Z = \beta_Z(g_F\mu_B)^{-2}$. We find $\gamma_Z = 1.7(6) \times 10^{-7}$ Hz^{-1}, in good agreement with the value of $1.5(2) \times 10^{-7}$ Hz^{-1} found in [118]. This results in a frequency shift of -2.5 $\times 10^{-17}$ at our nominal splitting of 400 Hz (corresponding to a bias magnetic field of 120 μT), with an uncertainty of 0.9×10^{-17}. We therefore apply a clock correction of 2.5×10^{-17}.

This measurement is limited by the statistics of the measurement and the small available lever arm on the magnetic field that we are able to create, however toward the end of my PhD work we have installed a

new magnetic coil on the vacuum chamber, which results in a factor of 10 improvement on the maximum magnetic field that we are able to create at the position of the atoms. Unfortunately, I didn't have time to take data using this improved lever arm during the course of my thesis.

5.5   Blackbody Radiation Shift

The black body radiation (BBR) shift arises from a differential AC Stark shift of the clock levels due to the electromagnetic radiation in thermal equilibrium with the environment of the atomic sample.

The frequency shift induced by the environment at a temperature T can be written as

$$\delta\nu_{BBR} = -\frac{2\sigma}{h\epsilon_0 c}\Delta\alpha_s T^4(1 + \eta T^2) \qquad (5.18)$$

where σ is the Stefan-Boltzmann constant, $\Delta\alpha_{\mathrm{st}}$ is the differential static polarizability between the excited and the ground state, and η is the so-called dynamical coefficient which takes into account the dependence of the differential polarizability on frequency. Based on the frequencies of the relevant transitions we expect that Mercury should behave similarly to Yb for which $\eta T^2 < 0.02$ [3]. The resulting frequency shift and associated uncertainty are in that case expected to be below 1×10^{-17} and therefore negligible with respect to the present uncertainty over the static term.

From the above written equation, we can see that the BBR shift depends both on atomic coefficients, which can be measured or calculated, and on an accurate estimation of the thermal environment of the atoms. It is this second point that is currently limiting most optical lattice clocks BBR evaluations.

As the BBR shift is the most significant item in the uncertainty budget of the best optical lattice clocks based on Sr [75], [24], [52] or Yb [54] atoms, much effort has been devoted to tackling this problem in several groups around the world. This includes ultra-precise in-situ radiation thermometry [7], radiation shielding [3], or cryogenic setups [113]. An alternative method is to use as a frequency standard an atom which is very weakly sensitive to the BBR shift, such as Hg or Mg [50].

In the case of Hg, the sensitivity to this effect is much smaller than for Sr (30 times) or Yb (16 times) [44], and therefore controlling this shift down to the 10^{-17} level uncertainty only requires the knowledge of the thermal environment of the atoms at the level of a few Kelvin. The limit to the evaluation of the BBR shift will then arise from the uncertainty that we apply to the atomic coefficients, for which only theoretical estimates are available.
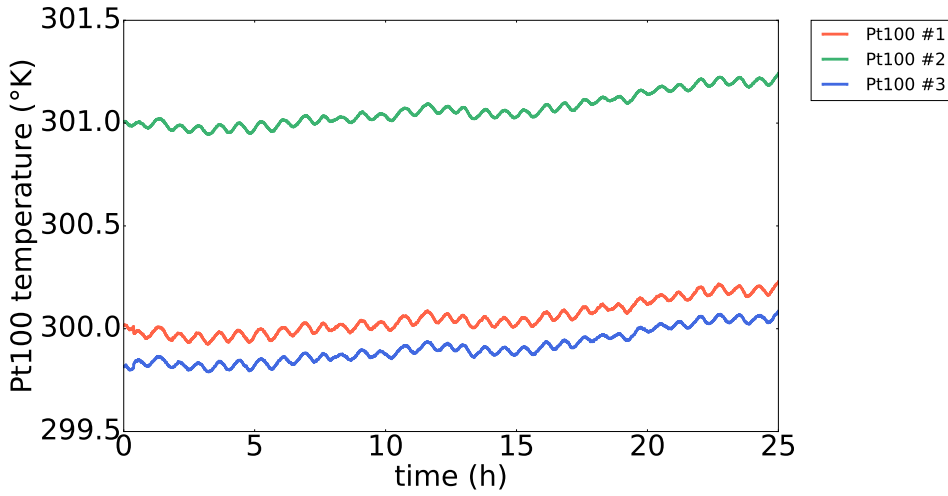
Figure 5.7. *Temperature of the 3 calibrated Pt100 sensors surrounding the vacuum chamber over the course of a 25 hours measurement run.*

Nevertheless, in order to evaluate both temperature and thermal gradients in the environment seen by the atoms, we have put three 100 ohms platinum resistors (Pt100) sensors in contact with the vacuum chamber. As can be seen on figure 5.7, the three sensors measure temperature differences no higher than 1.5 K over the course of 24h.

The average measured temperatures for Pt100 # 1, 2 and 3 are respectively 300.1°K, 301.1°K and 300°K over this representative measurement run. We apply a 1.5K uncertainty on the measured temperature (mean of the three Pt100 temperatures) at the atoms position.

Assuming a 10 % uncertainty on the **calculated** differential polarizability [35] and with a measured temperature around the atoms of $(301.0\pm1.5)\,\text{K}$, we get a clock correction of 1.6×10^{-16} with an uncertainty of 2×10^{-17}.

As the mercury clock progresses further down to the 10^{-18} range accuracy, a direct measurement of the static differential polarizability,

as was done on Sr [70] and Yb [103] will become crucial.

5.6   Measurement of the Phase Chirp Introduced by the Pulsing of the Clock Acousto-Optics Modulator

The switching on and off of the AOM to produce the clock and state selection pulses introduce RF power transients in the AOM crystal.

The net effect of these transients is to introduce phase chirps on the clock laser field, due to path length and index of refraction variations, which in turn create a frequency shift on the clock.

This effect is quite challenging to measure via the digital lock-in detection technique so we realized a pulsed, interferometric measurement of the phase transients similar to the ones found in refs. [99], [18], [46]. The clock light after passing through the AOM is beat with a small part of the beam taken before the AOM, which forms a CW reference arm. This reference light passes through another identical AOM for heterodyning the beat signal.

The beatnote in the UV is collected onto a fast photodiode and analyzed in the time domain to extract the phase information.

A schematic of the measurement setup is shown on figure 5.8:

5.6.1   Digital I/Q demodulation for phase estimation

We acquire the optical beatnote (signal), the RF beatnote (reference) providing our phase reference, and a common time-tag.

The procedure for the analysis in the time domain, which allows us to extract the phase information related to the pulsing of the AOM is the following:

- We first compute the initial phase ϕ_0 for both the signal and the reference by fitting the time traces with a function of the form $A\cos(2\pi ft) - B\sin(2\pi ft) + C$ and extracting $\phi_0 = atan(B/A)$.

- We then demodulate the signal and the reference by computing the in-phase (I) and in quadrature (Q) components.

- The I/Q data are then filtered with a order 3 low-pass Butterworth filter with a cutoff frequency of 100 Hz and an anti-aliasing
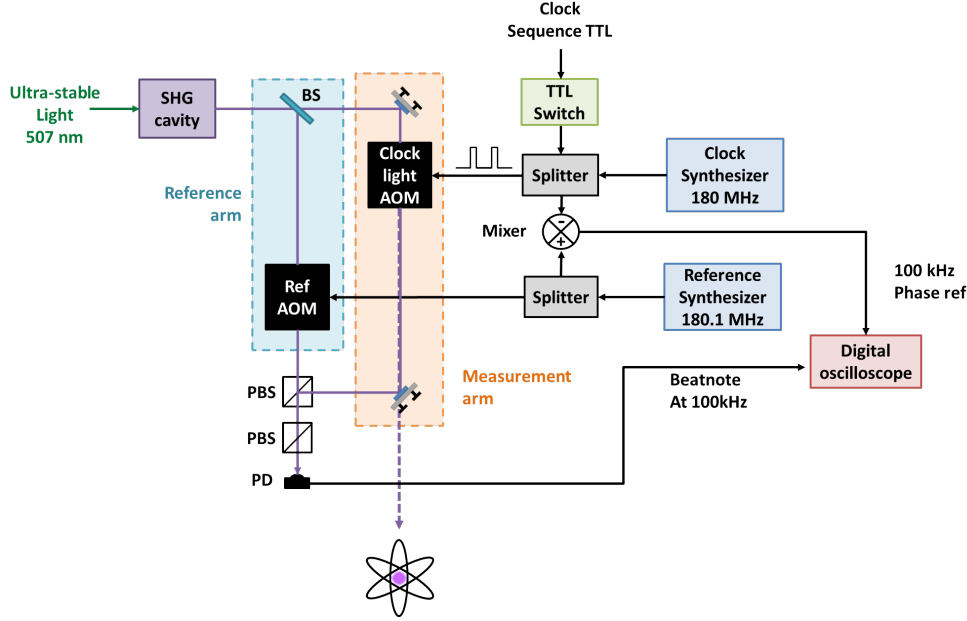
Figure 5.8. *Scheme of the AOM phase-transient measurement setup. Two synthesizers are used to drive the clock and the reference arm AOM, respectively at 180 and 180.1 MHz. The pulses are created via a TTL signal sent to the clock AOM. We take a small amount of clock light at 266 nm from the output of the second harmonic generation cavity using a beam-sampler (BS). This light is sent to the reference AOM (Ref AOM), while the remaining light goes through the usual clock beam path and is pulsed through the clock light AOM. The measurement and reference arms are overlapped at the output port of a polarizing beam-splitter (PBS), their polarizations are matched thanks to a second PBS, and sent to a photodiode (PD). The resulting beatnote at 100 kHz is acquired with a digital oscilloscope and the phase is extracted by numerically computing the amplitude of the in-phase and in-quadrature components. Two splitters and a mixer provide the phase reference for the demodulation.*

filter is applied (decimation by a factor 64).

- The obtained time traces are normalized by the quadratic mean of the I and Q signals.

- Finally, the phase of each signal is computed according to the formula $\phi^{(ref/sig)} = atan(\frac{Q^{(ref/sig)}}{I^{(ref/sig)}})$, followed by the absolute phase $\phi = \phi^{(sig)} - \phi^{(ref)}$.

5.6.2   Results and shift estimation

The results of the averaging of 654 consecutive measurements is shown on figure 5.9 (a) for several RF driving powers of the AOM: -4

dBm, -9 dBm and -14 dBm on the software of the experiment, corresponding respectively to 1.7 W, 0.5 W and 0.17 W of driving RF power.

The frequency shift $\Delta\nu_{probe} = \frac{1}{2\pi}\frac{d\phi}{dt}$ corresponding to the slope of the time traces is plotted in Figure 5.9 (b). We fit this graph with a linear
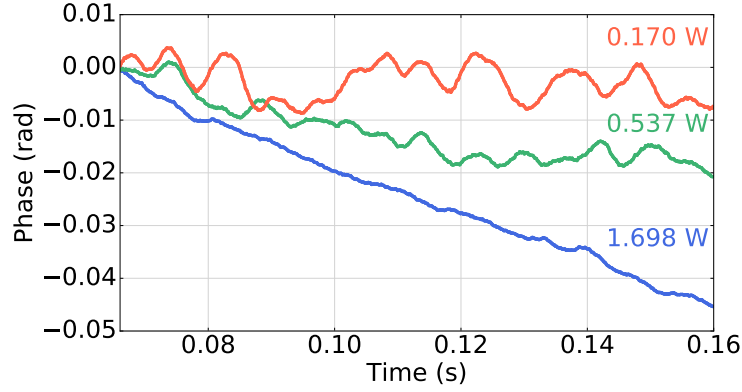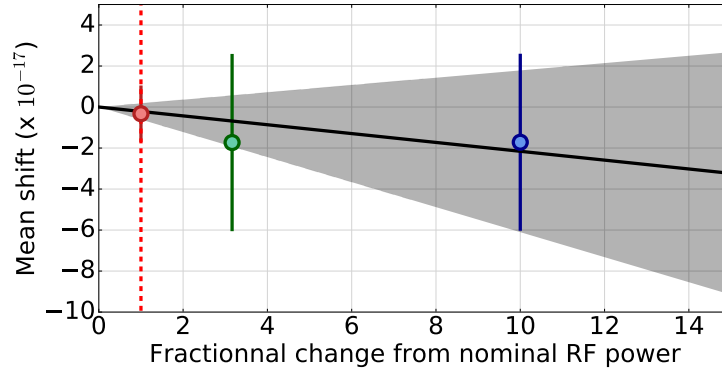
Figure 5.9. *(a) Typical time-trace of the computed phase of the beatnote inside the probe pulses time window for several RF powers (b) Frequency shift introduced by the AOM phase chirp as a function of the fractional RF power with respect to our nominal RF power of 170 mW. The black dotted lines materialize 1σ confidence interval on the fit represented in full black line, and the nominal operating point of the clock is indicated by the red dotted line.*

model, and extrapolate the shift to a RF power of 170 mW driving the AOM, which corresponds to the typical value for the operation of the clock at $\simeq 0.1$ s of Rabi time, we obtain a frequency correction of 3×10^{-18} (red dotted line on the plot) consistent with zero with an uncertainty below 10^{-17}.

The relatively big error bars of Figure 5.9 (b) are due to dispersion in

the phase extracted from the different runs for each data point. This dispersion might be because of the poor signal to noise ratio of the measurement, which is quite hard to perform at 266 nm. Alternatively, it can also come from the fact that the two arms of the interferometer are not stabilized, which means that relative optical path-lengths fluctuations can spoil the measurement.

In the future, when targeting below 10^{-17} uncertainties, a more thorough estimation of this effect will become necessary, with more work needed on the data acquisition, averaging procedure and to stabilize the optical path-lengths in the interferometer. Moreover, the contribution from the state selection pulses is hard to decouple from the contribution of the clock pulse itself, and might be a significant contribution to a potential frequency shift.

Figure 5.10. *Time sequence for probing in Rabi configuration. The blue pulses represent the RF power sent to the clock AOM as a function of time, close to the atomic resonance. The violet pulses are the cooling light applied to the atoms for pushing and detecting.*

Alternatively, Ramsey spectroscopy offers the possibility to mitigate this shift. Indeed, when performing Rabi spectroscopy, the state selection pulses and the clock pulses are severely asymmetric (see Figure 5.10), because short state selection π pulses a desirable for efficient population transfer, while long Rabi π pulses are needed for narrow transition probing.

In the case of Ramsey spectroscopy, as shown on Figure 5.11, we can easily have all pulses realized with the same RF power.

A simple yet efficient idea to mitigate the shift would therefore consist in never switching off the AOM, but simply operating it at constant power, and setting the detuning close to resonance during the probing
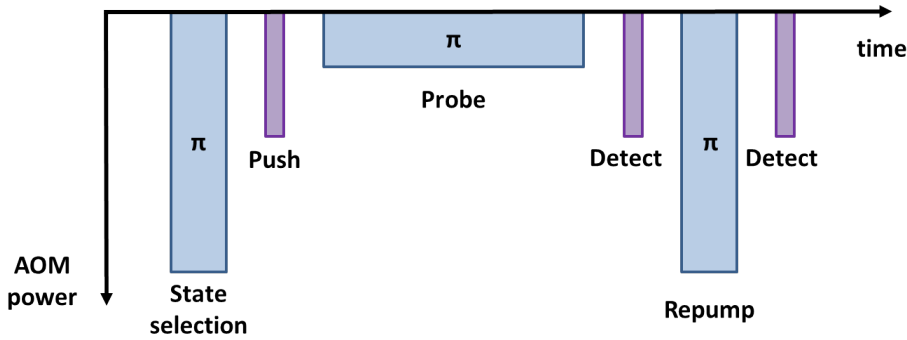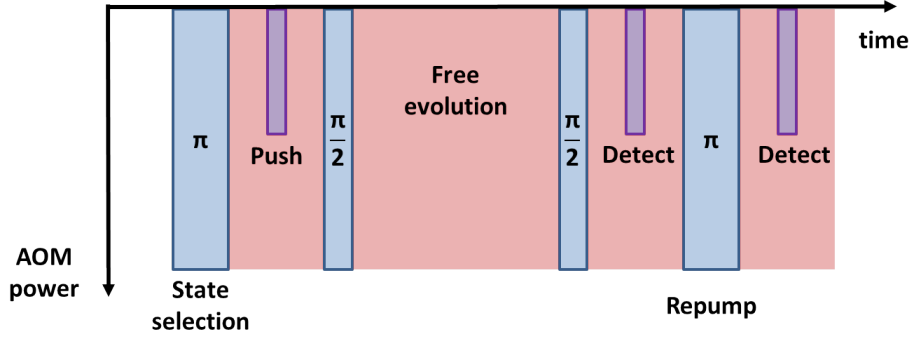
Figure 5.11. *Time sequence for probing in Ramsey configuration. The blue pulses represent the RF power sent to the clock AOM as a function of time, close to the atomic resonance. Alternatively, the red pulses represent the RF power sent to the clock AOM far detuned from the atomic resonance. The violet pulses are the cooling light applied to the atoms for pushing and detecting.*

phases (blue rectangles of Figure 5.11) and far detuned from resonance during the "dark time" phases (red rectangles of Figure 5.11), in order to avoid creating a light-shift on the atoms. Using this technique, the shift due to the AOM transient would be completely eliminated without the need for complex free-space Doppler cancellation techniques. These techniques will be required however to cancel fluctuations in the unavoidable free-space optical path-lengths associated with probing the atoms with UV light, for which optical fibers are not yet commercially available, although some progress have been made recently [15], [61].

5.7   Other Shifts

5.7.1   Background gas collisions

The Van-der-Waals potential governing long-range neutral atoms dipolar interactions is of the form:

$$V(R) = -\frac{C_6}{R^6} \qquad (5.19)$$

Where R is the inter-particle separation, and C_6 is a constant dispersion coefficient which depends on the nature of the two particles colliding. For Hg - Hg collisions, this coefficient is 268 in units of $\mathrm{Ha}a_0^6$ (Hartree times Bohr's radius to the 6th power) [29]. The frequency shift associated with this type of interaction stems from the different

phase-shift acquired by the two clock states during the collision process.

Under certain approximation (for example neglecting terms other than C_6/R^6) and in the case of Ramsey spectroscopy, an approximate formula can be written [27]:

$$-\frac{\Delta\nu}{\nu} = \Delta A/(13.8\pi\nu T_R)\Delta C_6/C_6 \tag{5.20}$$

Where ΔA is the percentage of cold atoms ejected from the lattice during the Ramsey/Rabi time T_R.

ΔA can be estimated based on the lifetime of the atoms in the optical lattice, which in our case is close to 300 ms.

Under these assumption, we calculate that the frequency correction associated with this shift is small enough to be neglected at our present uncertainty.

Moreover, since Formula 5.20 very loosely applies to our case, applying a non-zero correction is dangerous at this point. In order to better estimate this shift, the theoretical model has to be refined, and/or an experimental characterization has to be performed, for example by measuring the shift associated with a change of the background pressure inside the vacuum chamber. This measurement is quite hard to do, because changes in the background pressure occur very slowly, and therefore another frequency standard has to be used as a frequency reference, and the accuracies of both standards have to be maintained over the several days/weeks that the measurement might take.

5.8   Final Uncertainty Budget

The final uncertainty budget for the mercury clock at the end of this thesis is presented on Figure 5.12. We apply a total correction of 17.4×10^{-17} ($\simeq$ 0.2 Hz) to the clock transition frequency in nominal clock operation.

The main limitation to the accuracy is the linear lattice light-shift (in red in the table). Some systematics (shown in violet in the table) are only limited by the statistics of the measurements presented above, and can therefore be easily reduced by taking more data. For some other systematics, represented by the color yellow/orange, only

	Correction (10^{-17})	Uncertainty (10^{-17})
Lattice light shift linear	**-0.6**	**5.1**
Cold collisions	5.2	6.4
Second order Zeeman	2.5	0.9
Lattice light shift non-linear	-6	4
BBR	16.1	2.2
Background gas collisions	0	2.0
AOM chirp	0.2	0.4
Probe light shift	0	0.1
TOTAL	**17.4**	**9.6**

Figure 5.12. *Final uncertainty budget for the mercury clock, limited by the statistics on the estimation of the linear lattice light-shift coefficient.*

theoretical estimates are available. When targeting the 10^{-18} level of accuracy, BBR coefficients, non-linear lattice light shifts and pressure shifts will need to be experimentally characterized. Finally, the shifts associated with the interrogation light pulses are shown in blue, and we see that for both the probe light shift and the AOM phase chirp, the correction applied is consistent with zero shift within the stated uncertainty. This study of the physics of the mercury clock transition has allowed us to measurement atomic coefficients specific to the mercury atom (2nd order Zeeman coefficient, lattice light-shift coefficient etc.) and that we can therefore compare with the values found in other labs. Comparing with the only other available clock with similar performances as ours, we have all found all coefficient to be in reasonable agreement with the ones measured in [118].

The final uncertainty for the mercury clock is 9.6×10^{-17}, a factor of 60 improvement with respect to the latest estimation before the beginning of this thesis [65].

The mercury clock uncertainty is therefore slightly below the uncertainty of the best cesium fountain clocks in the world [33], below

the current physical realization of the SI second. This makes it imperative to develop techniques to compare our clock with the best primary frequency standards, but also with other standards whose accuracy are below the realization of the SI, namely other optical clocks. This is the subject of the next chapter of this thesis.

Chapter 6

Frequency Ratio Measurements for Fundamental Physics and Metrology

The final chapter of this thesis deals with the measurement of frequency ratios between highly-accurate atomic clocks via a fibered optical frequency comb. Most of the results described in this chapter are based on [111].

Frequency ratios are dimensionless physical quantities which play an important role in frequency metrology and are paramount in assessing the consistency and accuracy of clocks [58]. These measurements are essential to compare clocks whose uncertainties are below the limits of the physical artifacts used to realize the SI second.

A crude scheme, but nevertheless useful to understand the principle of the ratio measurement is sketched on figure 6.1.

The heart of the comparison is the optical frequency comb (OFC), which provides a link between the optical and microwave domains as well as an almost noiseless link between optical frequencies, [78].
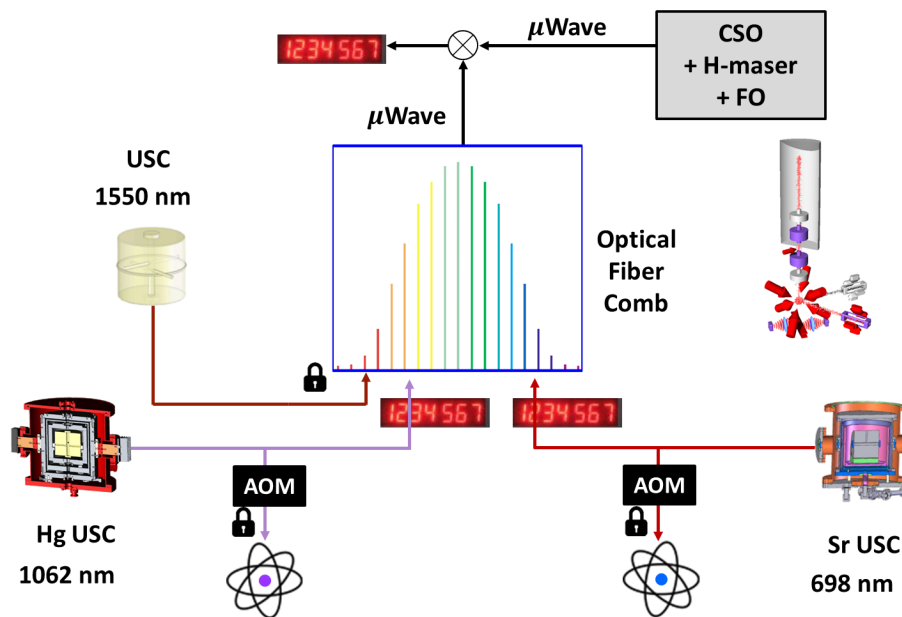
Figure 6.1. *Overall scheme of the frequency ratios measurements setup using an optical frequency comb.*

6.1   Purpose of Frequency Ratios Measurements

6.1.1   Redefinition of the SI second

With the continuous improvement of optical frequency standards uncertainties over the last decade, beyond the accuracy of the best cesium frequency standards used to realize the SI second, there has been much talk about a possible redefinition of the SI second in terms of an optical frequency [93].

To date, several frequency standards report uncertainty budgets in the low 10^{-18} range accuracy [39], [7], but these uncertainty budgets are only ascertained via self-comparisons, using the techniques discussed in Chapter 5, which means that these are only relative measurements which might be overlooking potential frequency biases.

The only way to check the consistency of the uncertainty budgets is to compare independent atomic clocks, by performing both comparisons between clocks based on the same species [113], [74], and then by measuring ratios between the transition frequencies of different atomic species [73], [108]. These measurements address dimensionless and universal physical quantities of nature allowing for con-

sistency checks to be performed in different labs around the world.

We therefore argue that frequency ratio measurements are essential tools to ascertain the reliability of optical atomic clocks and more generally optical frequency metrology in view of the redefinition of the SI second.

6.1.2   Time variation of fundamental constants

Paul Dirac was the first, in 1937, to introduce the idea that the physical constants of Nature (parameters appearing in physical laws, independent from measurement units, whose values cannot be calculated or inferred from operational theories, only measured experimentally) might in fact not be proper constants, but rather parameters that vary in time, and whose deep significance could be linked to cosmological parameters such as the age of the Universe [23].

Among those dimensionless physical constants, the fine structure constant [72]

$$\alpha = \frac{e^2}{4\pi\epsilon_0 \hbar c} \sim \frac{1}{137.035\ 999\ 160(33)} \tag{6.1}$$

where e is the electron charge, ϵ_0 is the vacuum permittivity, $\hbar = h/2\pi$ and c is the speed of light, is the coupling constant between electrons and photons. As such, it is the dominant parameter for the value of electronic transition frequencies in atoms, molecules, and ions.

Following this reasoning, a variation of the fine structure constant entails a change in the frequencies of atomic spectra. The sensitivity of a given atomic transition to the value of α is usually characterized by a coefficient, which depends on the considered atomic species and electronic transition [25]

$$\frac{\delta\nu}{\nu} = K_\alpha^{(atom)}\frac{\delta\alpha}{\alpha} \tag{6.2}$$

One of the key aspects to take into account, is that since different atoms have different electronic configurations, their sensitivity to a putative variation of the fine structure constant will be different (see Table 6.1). We can then write the sensitivity of **frequency ratios** to variations of α:

$$\frac{\delta(\nu_1/\nu_2)}{\nu_1/\nu_2} = (K_\alpha^{(1)} - K_\alpha^{(2)})\frac{\delta\alpha}{\alpha} \tag{6.3}$$

It is worth noting that, unlike Equation 6.2, Equation 6.3 is completely independent on the unit chosen to measure ν, reflecting the fact that

Table 6.1. *Sensitivity of a time variation of the fine structure constant for atoms currently used in optical clocks.*

Atom	transition wavelength (nm)	K_α (calc)	Transition
^{87}Sr	698	0.062	$^1S_0 \to {}^3P_0$
^{171}Yb	578	0.314	$^1S_0 \to {}^3P_0$
^{199}Hg	266	0.813	$^1S_0 \to {}^3P_0$
^{27}Al$^+$	267	0.008	$^1S_0 \to {}^3P_0$
^{171}Yb$^+$	436	0.996	$^2S_{1/2} \to {}^2D_{3/2}$ (E2)
^{171}Yb$^+$	467	-5.953	$^2S_{1/2} \to {}^2F_{7/2}$ (E3)
^{199}Hg$^+$	282	-2.940	$^2S_{1/2} \to {}^2D_{5/2}$

ν_1/ν_2, as pointed-out above, is a dimensionless quantity.

Several possible schemes can be envisioned to detect a potential variation of the fine structure constant:

- Measure the frequency ratio between a transition which is sensitive (for example mercury), and one which is almost insensitive (for example strontium) to α variations. In that case, the strontium clock would be used as an anchor, while the variation on the ratio will be due to the mercury transition sensitivity.

- A second possibility is to find two transitions with are both sensitive to α variations, but with opposite signs of sensitivity coefficients. It is for example the case of the $\nu_{\mathrm{Hg}}/\nu_{\mathrm{Yb}^+}$ (E3) frequency ratio.

In this case, the sensitivity is clearly enhanced.

6.2   Detailed Experimental Scheme

The detailed layout of the frequency comparison setup is shown on figure 6.2.

The light coming from the mercury and strontium clock laser is first sent to the respective optical tables for atomic interrogation thanks to a phase-compensated fiber link (using AOM1 and AOM6 as frequency actuators for the PLL) and locked onto their respective atomic transition.
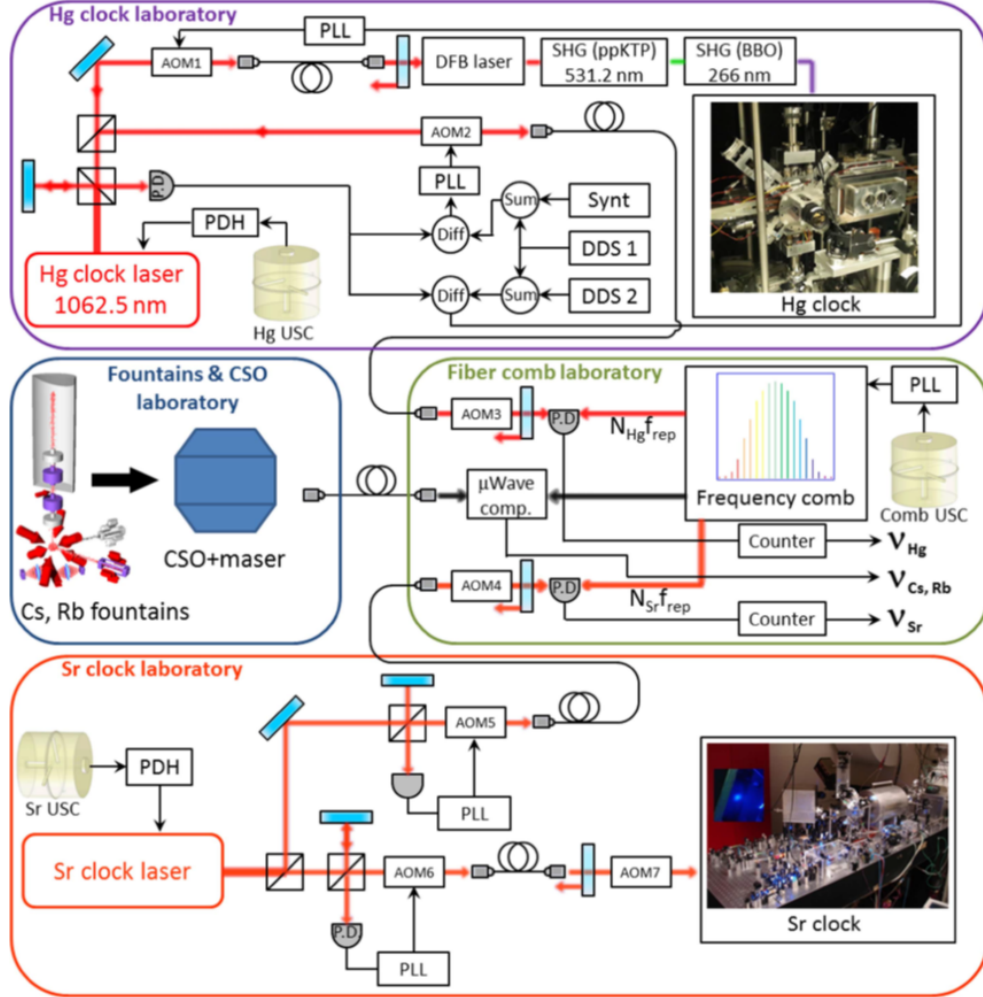
Figure 6.2. *Experimental scheme for comparing the mercury clock with microwave and optical standards. A small amount of probe light from each clock is sent to the fiber comb via frequency-stabilized optical fibers. For the mercury clock the stabilized path does not include the two stages of frequency doubling. The fiber comb is also connected to the (maser + CSO)ensemble via a frequency stabilized optical link, locked to the Cs and Rb fountains. The comb simultaneously measures all the frequencies. Note that the comb measures the frequency of the Hg clock in the infra-red and not in the UV. Picture taken from [111].*

Simultaneously, the light is sent to the optical frequency comb via actively phase-stabilized optical fiber links (using AOM5 and AOM2 as actuator respectively for Sr and Hg) and beat with the light from the comb, allowing frequency comparisons directly in the optical domain.

The mercury/comb beatnote, whose frequency can be tuned by AOM3 (for example to make sure that it is sufficiently far away from f_{rep} for a good signal to noise ratio) is usually kept around 140 MHz, and can be either counted straightforwardly using a frequency counter or actively used to perform spectral purity transfer (see Chapter 4).

The equations of the two optical beatnotes are:

$$\nu_{Hg}^{beat} = \nu_{Hg}^{USL} - N_{Hg} f_{rep} \tag{6.4}$$

$$\nu_{Sr}^{beat} = \nu_{Sr}^{USL} - N_{Sr} f_{rep} \tag{6.5}$$

as f_0 is detected and mixed-out, implementing an effective carrier-envelope-offset-free frequency comb. The two beatnotes are then counted against the microwave clock ensemble, which is therefore in common mode for the measurement, allowing optical frequency comparison at the level of 10^{-20} [57], far below the accuracy of either clocks.

Similarly, the light coming from the microwave clock ensemble, composed of a Cryogenic Sapphire Oscillator (CSO) and a hydrogen maser interrogating the Rb and Cs fountains is sent to the comb via a compensated microwave link. The ultrastable microwave derived from the CSO at 11.98 GHz is down converted into a signal at 8.985 GHz and used to modulate the amplitude of a 1.5μm laser diode injected in a compensated 200 meter fiber. The 36th harmonics of the repetition rate of the comb at a frequency around 9 GHz is detected by a high-speed photodiode and counted against the 8.985 signal from the microwave frequency standards, providing the "flywheel" to bridge the frequency gap between the optical and microwave domains.

This signal is also used to clock all the auxiliary synthesizers ensuring that its noise is common-mode with respect to every possible frequency difference.

6.3   Comparison With Microwave Frequency Standards

6.3.1   Hg/Cs frequency ratio

We performed a direct measurement of the mercury to cesium clock transitions frequency ratio, which we find to be

$$\frac{\nu_{\mathrm{Hg}}}{\nu_{\mathrm{Cs}}} = 122\ 769.552\ 729\ 311\ 011(45) \tag{6.6}$$

with a total fractional accuracy of 3.7×10^{-16} where the total uncertainty is the sum of three contributions: the systematic uncertainty on the mercury clock, the accuracy of the ^{133}Cs fountain [33] and of the frequency comb and the statistical uncertainty over the ratio measurement. The latter can be inferred from Figure 6.4 (a) where I plot the Overlapping Allan deviation of the $\frac{\nu_{\mathrm{Hg}}}{\nu_{\mathrm{Cs}}}$ ratio measurement in relative units as a function of integration time. The statistical uncertainty on the measurement, which is set by the quantum-projection-noise-limited Cs fountain clock instability and the measurement time, is the main contribution to the final uncertainty.
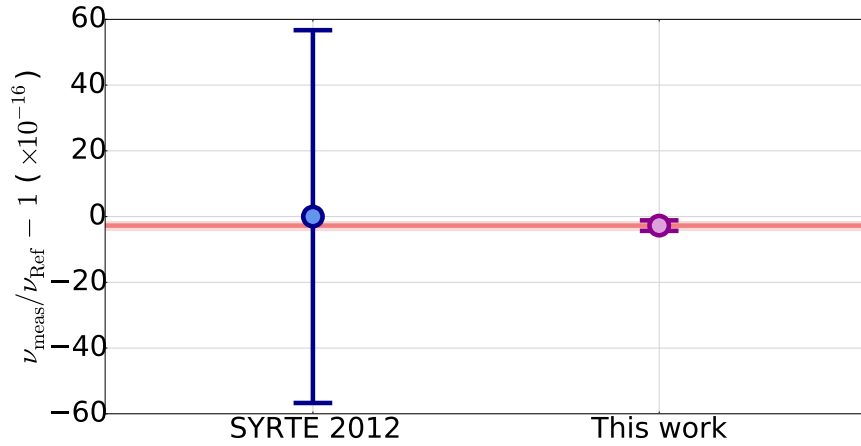
Figure 6.3. *Ratio between the measured absolute frequency of the mercury clock transition and the value of SYRTE's measurement in 2012 taken as reference (offset by unity). The 2012 measurement is in blue and the present measurement in violet. The horizontal red line and pale red shaded area are respectively the weighted mean of the two frequency measurements and the 1σ uncertainty on the mean.*

This is the most accurate direct measurement of the absolute frequency (i.e. with respect to a Cs frequency standard) of the mercury

clock transition, ν_{Hg} = 1128 575 290 808 154.62 Hz $\pm$0.19 Hz (statistical) $\pm$0.38 Hz (systematic including Cs accuracy). The previous best direct measurement had been obtained by our group and published in 2012 [65] with a fractional frequency uncertainty on the ratio measurement of 5.7×10^{-15}, the result is shown on Figure 6.3.

This work represents an improvement over the previous value by a factor 15.

6.3.2 Hg/Rb frequency ratio

We performed the first ever direct-measurement of the mercury to rubidium clock transitions frequency ratio. We obtain the value
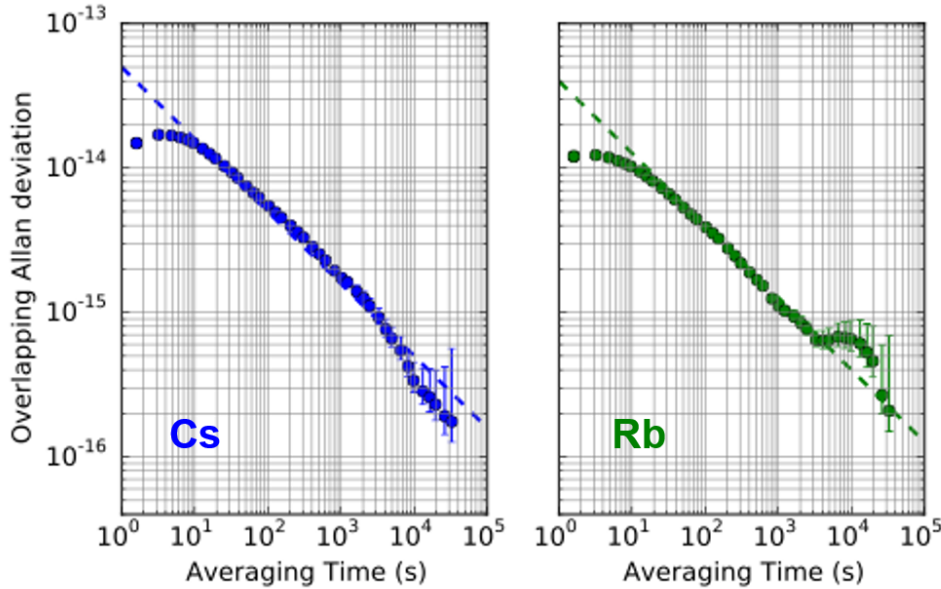
Figure 6.4. *Overlapping Allan deviation of the frequency ratio between Hg and FO2-Cs (left) and Hg and FO2-Rb (right). The dotted lines represent the stabilities of the fountains (limited by the quantum projection noise) over the length of the 2015 measurement campaign (3 weeks, 40 h of useful data),averaging as $\tau^{-1/2}$. Picture taken from [111].*

$$\frac{\nu_{\mathrm{Hg}}}{\nu_{\mathrm{Rb}}} = 165\ 124.754\ 879\ 997\ 258(62) \tag{6.7}$$

with a total fractional uncertainty of 3.8×10^{-16}.

Using this measured value and the best know measurement of the $\nu_{\mathrm{Rb}}/\nu_{\mathrm{Cs}}$ frequency ratio, and noting that $\nu_{\mathrm{Hg}} = (\nu_{\mathrm{Hg}}/\nu_{\mathrm{Rb}})(\nu_{\mathrm{Rb}}/\nu_{\mathrm{Cs}})\nu_{\mathrm{Cs}}$,

we can construct a 2nd "semi-independent"[1] value of the absolute frequency of the mercury clock transition, using Rb as a secondary representation of the SI second [34]. We find a value of ν_{Hg} = 1128 575 290 808 154.19 Hz ±0.15 Hz (statistical) ±0.40 Hz (systematics), in good agreement with the direct measurement with Cs presented above.

The stability of the microwave comparisons can be seen on the overlapping Allan deviation of clock frequency fluctuation of Figure 6.4. We can see on the plots the limit of the stability of the frequency ratios measurements, set in both cases by the quantum projection noise limited stability of the microwave clocks.

6.3.3   Gravitational redshift estimation and correction

General relativity dictates that the frequency of the clock is shifted towards smaller frequencies when it is operated in a weaker gravitational field by an amount [14]

$$\Delta\omega_{rs} = \frac{gL}{c^2}\omega_{clock} \tag{6.8}$$

At the surface of the earth, this gravitational redshift is approximately 10^{-16} per meter of elevation, which means that it is a significant correction to the measured frequency ratios at the stated uncertainty and needs to be properly taken into account [66].

The results of the comparison presented above take into account the gravitational redshift due to a height difference of 4.25(2) m (4.17(2) m) between the Hg clock and the Cs (Rb) fountain, calculated based on a leveling campaign carried out in 2013. The gravitational red shifts introduced by the height difference of 3(1) cm between the Hg and Sr clocks (Hg lying higher than Sr) contribute to less than 10^{-17}.

6.4   Comparison With a Strontium Optical Lattice Clock

For the first time during my thesis, thanks to the improvements described in the previous chapters, we were able to perform several direct optical-to-optical comparisons of the mercury clock with two

---

[1]The Cs and RB frequency references used in the comparison are operated within a single dual-species fountain apparatus, and are therefore not fully independent.
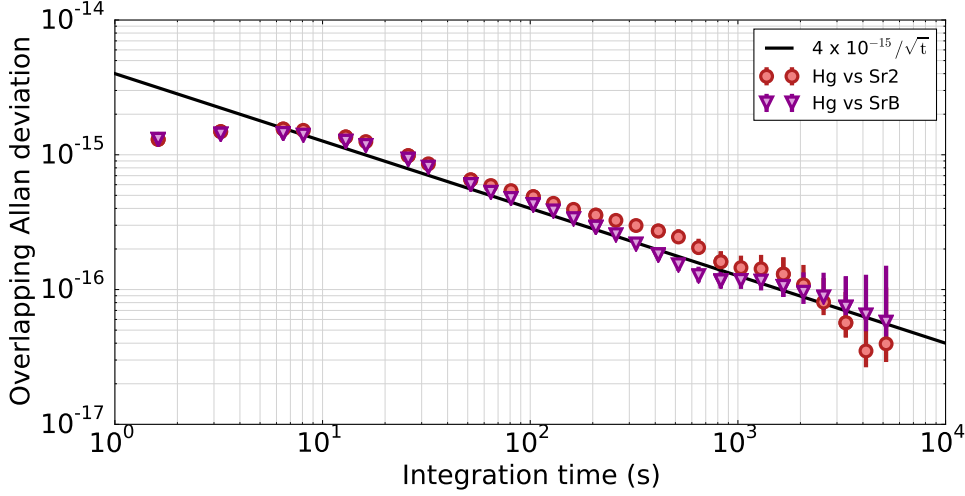
Figure 6.5. *Stability of the Hg/Sr comparison against SrB (violet triangles) and Sr2 (red dots). The black dashed line represents a stability of 4×10^{-15} at 1 second going down as $1/\sqrt{\tau}$.*

strontium clocks at SYRTE, which we will call SrB and Sr2 in the following, over the course of the thesis.

Figure 6.5 shows the Allan deviation of the frequency difference between the optical clocks for one such measurement over approximately 2 hours. The comparison averages down with a stability at one second of around 4×10^{-15} and reaches the mid 10^{-17} range after one hour of integration. We can note that the stability is much better than in the case of the comparison of mercury with microwave frequency standards, as expected from the increase in the atomic quality factor for optical clock transitions.

The uncertainty budget for the comparison is shown on Figure 6.6 The uncertainty of the comparison is mainly limited by the accuracy of the mercury clock evaluated as 1.7×10^{-16} (see Chapter 5), as the Strontium clocks contribute only 4.0×10^{-17} to the final uncertainty budget. As previously stated, the gravitational red-shift, corresponding to a height difference of 3 cm between the atomic ensembles is not relevant (below 10^{-17}) for the level of accuracy tested here.

We extract from the data the ratio of the mercury to strontium clock transitions:

$$\frac{\nu_{\mathrm{Hg}}}{\nu_{\mathrm{Sr}}} = 2.629\,314\,209\,898\,909\,15(46) \tag{6.9}$$

with a total uncertainty of 1.8×10^{-16}. This uncertainty is below the accuracy of the best Cs fountain clocks in the world, and therefore is

	Relative Uncertainty (10^{-17})
Sr clock	4.1
Hg clock	**16.7**
U_B (syst. total)	18
U_A (stat.)	5.0

Figure 6.6. *Final uncertainty budget for the mercury to strontium direct optical-to-optical clock comparison. U_B is the quadratic sum of the systematic uncertainty of the two optical clocks. The statistical uncertainty U_A takes into account the flicker floor of the frequency ratio measurement of 5×10^{-17}.*

below the accuracy of the current realization of the second from the SI system of units, a landmark for the mercury clock on the way to its ultimate accuracy. This frequency ratio has also been measured in the
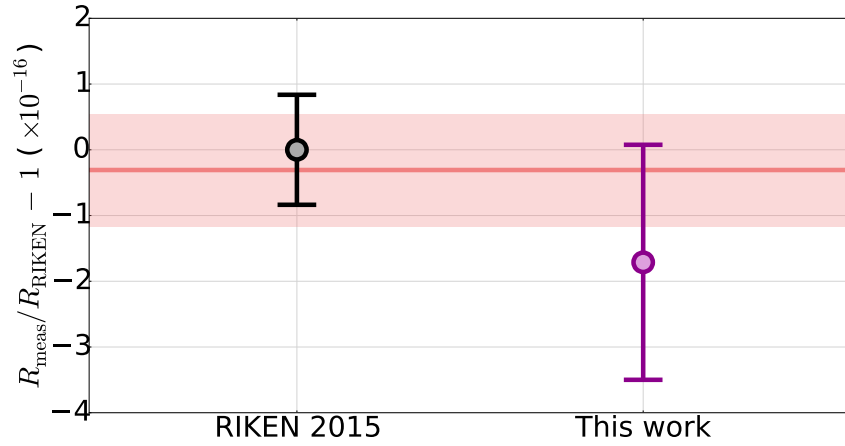
Figure 6.7. *Ratio between the measured ν_{Hg}/ν_{Sr} from our work and the value from the RIKEN group (offset by unity). We have plotted here the measurement in reference [118] (black) and the measurement of this work (violet). The horizontal red line and pale red shaded area are respectively the weighted mean of the two ratio values and the 1σ uncertainty on the mean.*

group of H. Katori at RIKEN (Japan) [118] with an uncertainty of 8.4 $\times 10^{-17}$, and as can be seen on Figure 6.7 with a good agreement with our value. We can note that this level of agreement between two completely independent labs, four different optical lattice clocks setups

on two sides of the world is a very good news for the mercury optical lattice clock as an accurate and reproducible frequency standard.

To our knowledge the ν_{Hg}/ν_{Sr} frequency ratio is now one of the best known physical quantities measured independently in different laboratories.

6.5 Measurement of Frequency Ratios via European Fiber Network

Towards the end of this thesis, a European comparison involving ultrastable fiber links [119] connecting SYRTE with PTB in Germany [56] and NPL in the United Kingdom allowed us to measure the ratio of the (optical) clock transition ν_{Hg}/ν_{Yb^+} for the first time, as well as comparing our mercury clock with Sr clocks at PTB and NPL.
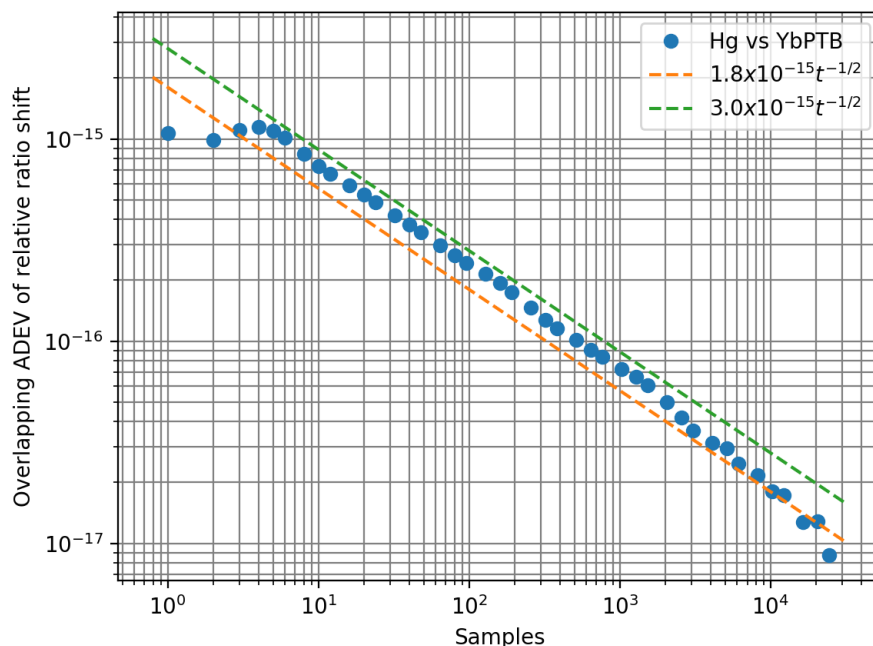
Figure 6.8. *Stability of the Hg/Yb$^+$ comparison through the European fiber link against the PTB Yb$^+$ ion clock. The inferred stability is around 2.5×10^{-15} at 1 second going down as $1/\sqrt{\tau}$ to the 1×10^{-17} level in 10 000 seconds.*

The stability of the comparison against the ν_{Yb^+} clock at PTB [39] through the European fiber link is shown on Figure 6.8. The frequency

ratio measurement reaches a statistical uncertainty of 1×10^{-17} in 10 000 seconds, with no sign of frequency flickering. During these measurements, the magic wavelength frequency was continuously locked to the operational optical frequency comb.

As was previously mentioned, this ratio is very relevant for the monitoring of a potential variation of the fine structure constant α, since the (E3) Yb$^+$ clock transition is very sensitive to this variation, while the Hg clock is relatively less sensitive, but with a sensitivity coefficient of opposite sign, enhancing the sensitivity of the $\nu_{\text{Hg}}/\nu_{\text{Yb}^+}$ ratio to $\dot{\alpha}$ (see Section 6.1.2).

6.6   Long-Term Monitoring and Fundamental Constants

In the course of this thesis, the Hg/Sr clock frequency ratio has been measured several times with uncertainties in the low 10^{-16} range. As discussed in section 6.1, this is a first step towards long-term monitoring of a potential variation of the fine structure constant.

Moreover, we have also measured the ratios Hg/Cs and Hg/Rb down to the state of the art uncertainty of SYRTE's microwave standards, which are very relevant to potential variation of the proton to electron mass ratio μ [38] [28], as well as probing the coupling between fundamental constants and Gravity [5].

Conclusion

In this thesis manuscript, I have presented my main contributions to the mercury optical lattice clock setup at SYRTE in order to reach much higher clock performances. I have designed and built a new cooling laser system working reliably over several weeks at an output power of 50 mW at the challenging wavelength of 254 nm with minimal maintenance, I have also installed a new Ti:Sa laser for the lattice light, along with its frequency control, which will allow the study of the systematics related to the trapping environment below the 10^{-17} level of fractional frequency accuracy. I have also helped contribute to the installation of a new infrared amplifier for the clock light.

With these key technical improvements, the reliability and up-time of the experiment was drastically increased, and the clock stability was improved to a value of 1.2×10^{-15} at one second of integration time, allowing measurement resolution at the 10^{-17} level for the study of the physical parameters of the clock. I have demonstrated measurement and control of the frequency systematics below the 10^{-16} level, with a final uncertainty of 9.6×10^{-17}, below the realization of the SI second by Cs frequency standards [33].

With the increased accuracy, it became scientifically relevant to compare our clock with Cs fountains. This measurement was already realized in our group in 2012 [65] with an accuracy (limited by the mercury clock) of 5.4×10^{-15}. In this work, we reach an accuracy for the clock comparison of 3.7×10^{-16}, mainly limited by the microwave standard, a factor of 15 improvement with respect to the previous measurement. We also realized the first direct measurement of the Hg/Rb frequency ratio, to the level of 3.8×10^{-16}. Maybe even more important, we have measured for the first time in our lab, and the second time ever, the ratio of the clock transition frequencies $\nu_{\mathrm{Hg}}/\nu_{\mathrm{Sr}}$ below the current realization of the SI second, and in good agreement with

the previous value. These measurement as well as the ones performed in the lab of Prof. Katori in RIKEN lead to the recognition of the ^{199}Hg clock transition as a Secondary Representation of the Second by the 2017 CCTF (Consultative Committee for Time and Frequency). Filling and improving the list of *Recommended values of standard frequencies for applications including the practical realization of the metre and secondary representations of the second* is an important task toward the redefinition of the SI second.

We have also laid the groundwork for further improvements of the clock setup. A second cooling laser system has been build and is now producing UV light at 254 nm for use in a 2D-MOT which had been used shortly in the early times of the experiment [85] before being abandoned for lack of enough UV power to reliably operate it. The re-operation of the 2D-MOT is expected to take place in the coming weeks (all the optics necessary to bring the light to the 2D-MOT chamber are still in place and the last step remains to align the new UV laser system on the old optical path). This will enable a great increase in loading rate into the MOT and the optical lattice, enabling shorter cycle times and longer interrogation times, improving the stability of the clock by potentially a factor of 5. With the longer lifetime of the atoms in the optical lattice, it should be straightforward to measure for the first time the lifetime of the clock state of mercury, which is the subject of conflicting data in the literature. Indeed, [35] predicts a lifetime of $\simeq$ 100 seconds, while a more recent calculation expects a lifetime of 1.3 seconds [87]. Moreover, the 2D MOT will allow clock operation with much higher atomic densities, enabling the study of density-related frequency shifts in the mercury clock (so far still unresolved on our experiment).

The results presented in this thesis show no limitation to the potential accuracy of a clock based on ^{199}Hg, and mercury remains a good candidate for a room temperature frequency standard with accuracy of 10^{-18} or below. The referencing of the lattice light to the optical frequency comb will prove essential in reducing the uncertainty associated with the lattice light-shift below the 10^{-17} level, and allow the investigation of higher-order lattice light-shifts, which need to be experimentally studied to determine to which extend they might limit the mercury optical lattice clock accuracy at the low 10^{-18} level, and for which theoretical calculations vary from one publication to the next

[44], [79]. To reach the 10^{-18} level of uncertainty however, a measurement of the static and dynamic BBR coefficients will be needed, either through a direct measurement of the static polarizability, or thanks to a new vacuum chamber cooled down to cryogenic temperatures and compared to a room temperature mercury clock.

I expect that transfer of spectral purity using an optical frequency comb will be an important enabling technique for the future of optical frequency metrology, allowing to share the stability of a single ultrastable clock laser between several users and/or experiments. A first step towards this direction has been made by locking the mercury clock laser to a 1.5 μm ultrastable cavity using the frequency comb, and synchronized interrogation with the Sr clock has been performed for the first time. The advantage of this method has not been fully demonstrated in the attempt made in the course of this thesis with only a modest improvement of the frequency ratio frequency stability from 4×10^{-15} at one second for uncorrelated clocks to 3×10^{-15} at one second for the synchronous measurement. The limit on this measurement was set by the frequency drifts of the Fabry-Perot cavity at 1.5 μm used to stabilize the optical frequency comb. One simple solution to overcome this problem on the short term is to directly transfer the spectral properties of the mercury cavity to the strontium clock laser via the comb. On the long term, a first project aims at building a long Fabry-Perot cavity to provide a much improved frequency reference with respect to the currently available cavities, while a second project investigates laser frequency stabilization based on spectral hole burning in rare-earth doped crystals. Both alternatives have the potential to provide ultrastable frequency references to the comb, and through the comb to the mercury laser, improving even more the stability of the clock to the low 10^{-16} level at 1 second.

Finally, with an accuracy at the 10^{-17} level and below, optical clocks are expected to contribute to the monitoring of fundamental constants, and the mercury clock provides a unique opportunity for ultra-accurate frequency ratio measurement all over Europe thanks to the newly built ultra-stable fiber network architecture [56]. Frequency ratios with ionic species such as Yb^+ (PTB, NPL), both on the quadrupole and octupole transition [28], [39], have for example never been measured and are scientifically exciting in view of searching for putative variations of the fine structure constant.

The prospect for the mercury clock are therefore numerous, but other exciting opportunities lie in the study of ultra-cold mercury atoms as provided by the setup. Collisional properties of mercury through photo-associative spectroscopy would provide insight into the collisional physics of mercury, and would allow for a better estimation of collisional shifts through the measurement of clock states scattering lengths. Moreover, quantum degeneracy has not yet been reached with mercury atoms, and ours is one of the very few setups in the world for which this goal would be within reach, opening the door to a three-dimensional Fermi-degenerate mercury optical lattice clock with ultimate accuracy and stability below the 10^{-18} level at room temperature [11].

Bibliography

[1] Ali Al-Masoudi, Sören Dörscher, Sebastian Häfner, Uwe Sterr, and Christian Lisdat. Noise and instability of an optical lattice clock. *Phys. Rev. A*, 92:063814, Dec 2015.

[2] D. W. Allan. Statistics of atomic frequency standards. *Proceedings of the IEEE*, 54(2):221–230, Feb 1966.

[3] K. Beloy, N. Hinkley, N. B. Phillips, J. A. Sherman, M. Schioppo, J. Lehman, A. Feldman, L. M. Hanssen, C. W. Oates, and A. D. Ludlow. Atomic clock with 1×10^{-18} room-temperature blackbody stark uncertainty. *Phys. Rev. Lett.*, 113:260801, Dec 2014.

[4] M.C. Bigeon. Probabilité de transition de la raie 6 ^{1}S$_0$-6 ^{3}P$_0$ du mercure. *Journal de Physique*, 28:51, 1967.

[5] S. Blatt, A. D. Ludlow, G. K. Campbell, J. W. Thomsen, T. Zelevinsky, M. M. Boyd, J. Ye, X. Baillard, M. Fouché, R. Le Targat, A. Brusch, P. Lemonde, M. Takamoto, F.-L. Hong, H. Katori, and V. V. Flambaum. New limits on coupling of fundamental constants to gravity using ^{87}Sr optical lattice clocks. *Phys. Rev. Lett.*, 100:140801, Apr 2008.

[6] S. Blatt, J. W. Thomsen, G. K. Campbell, A. D. Ludlow, M. D. Swallows, M. J. Martin, M. M. Boyd, and J. Ye. Rabi spectroscopy and excitation inhomogeneity in a one-dimensional optical lattice clock. *Phys. Rev. A*, 80:052703, Nov 2009.

[7] B. J. Bloom, T. L. Nicholson, J. R. Williams, S. L. Campbell, M. Bishof, X. Zhang, W. Zhang, S. L. Bromley, and J. Ye. An optical lattice clock with accuracy and stability at the 10^{-18} level. *Nature*, 506(7486):71–75, feb 2014.

[8] Justin G. Bohnet, Zilong Chen, Joshua M. Weiner, Dominic Meiser, Murray J. Holland, and James K. Thompson. A steady-state superradiant laser with less than one intracavity photon. *Nature*, 484(7392):78–81, April 2012.

[9] G. K. Campbell, M. M. Boyd, J. W. Thomsen, M. J. Martin, S. Blatt, M. D. Swallows, T. L. Nicholson, T. Fortier, C. W. Oates, S. A. Diddams, N. D. Lemke, P. Naidon, P. Julienne, Jun Ye, and A. D. Ludlow. Probing interactions between ultracold fermions. *Science*, 324(5925):360–363, 2009.

[10] S. L. Campbell. *A Fermi-Degenerate Three-Dimensional Optical Lattice Clock*. PhD thesis, University of Colorado at Boulder, 2017.

[11] S.L. Campbell, R.B. Hutson, G.E. Marti, A. Goban, N. Dark-wah Oppong, R.L. McNally, L. Sonderhouse, Robinson J.M., W. Zhang, B.J. Bloom, and J. Ye. A Fermi-degenerate three-dimensional optical lattice clock. *ArXiv e-prints*, aug 2017.

[12] J.-S. Chen, S. M. Brewer, C. W. Chou, D. J. Wineland, D. R. Leibrandt, and D. B. Hume. Sympathetic ground state cooling and time-dilation shifts in an $^{27}Al^+$ optical clock. *Phys. Rev. Lett.*, 118:053002, Jan 2017.

[13] C. W. Chou, D. B. Hume, J. C. J. Koelemeij, D. J. Wineland, and T. Rosenband. Frequency comparison of two high-accuracy Al^+ optical clocks. *Phys. Rev. Lett.*, 104:070802, Feb 2010.

[14] C. W. Chou, D. B. Hume, T. Rosenband, and D. J. Wineland. Optical clocks and relativity. *Science*, 329(5999):1630–1633, 2010.

[15] Yves Colombe, Daniel H. Slichter, Andrew C. Wilson, Dietrich Leibfried, and David J. Wineland. Single-mode optical fiber for high-power, low-loss UV transmission. *Opt. Express*, 22(16):19783–19793, Aug 2014.

[16] Jean Dalibard. *Collisional dynamics of ultra-cold atomic gases, in Bose-Einstein Condensation in Atomic Gases, Proceedings of the International School of Physics "Enrico Fermi"*, pages 321–349. M. Inguscio, S. Stringari, C.E. Wieman, 1999.

[17] S. T. Dawkins, R. Chicireanu, M. Petersen, J. Millo, D. V. Magalhães, C. Mandache, Y. Le Coq, and S. Bize. An ultra-stable referenced interrogation system in the deep ultraviolet for a mercury optical lattice clock. *Applied Physics B*, 99(1):41–46, 2010.

[18] C. Degenhardt, T. Nazarova, C. Lisdat, H. Stoehr, U. Sterr, and F. Riehle. Influence of chirped excitation pulses in an optical clock with ultracold calcium atoms. *IEEE Transactions on Instrumentation and Measurement*, 54(2):771–775, April 2005.

[19] Hans Dehmelt. Experiments with an isolated subatomic particle at rest. *Rev. Mod. Phys.*, 62:525–530, Jul 1990.

[20] P. Delva, J. Lodewyck, S. Bilicki, E. Bookjans, G. Vallet, R. Le Targat, P.-E. Pottie, C. Guerlin, F. Meynadier, C. Le Poncin-Lafitte, O. Lopez, A. Amy-Klein, W.-K. Lee, N. Quintin, C. Lisdat, A. Al-Masoudi, S. Dörscher, C. Grebing, G. Grosche, A. Kuhl, S. Raupach, U. Sterr, I. R. Hill, R. Hobson, W. Bowden, J. Kronjäger, G. Marra, A. Rolland, F. N. Baynes, H. S. Margolis, and P. Gill. Test of special relativity using a fiber network of optical clocks. *Phys. Rev. Lett.*, 118:221102, Jun 2017.

[21] G John Dick. Local oscillator induced instabilities in trapped ion frequency standards. Technical report, CALIFORNIA INST OF TECH PASADENA JET PROPULSION LAB, 1987.

[22] F. Diedrich, J. C. Bergquist, Wayne M. Itano, and D. J. Wineland. Laser cooling to the zero-point energy of motion. *Phys. Rev. Lett.*, 62:403–406, Jan 1989.

[23] P. A. M. Dirac. A new basis for cosmology. *Proceedings of the Royal Society of London A: Mathematical, Physical and Engineering Sciences*, 165(921):199–208, 1938.

[24] Stephan Falke, Nathan Lemke, Christian Grebing, Burghard Lipphardt, Stefan Weyers, Vladislav Gerginov, Nils Huntemann, Christian Hagemann, Ali Al-Masoudi, Sebastian Häfner, Stefan Vogt, Uwe Sterr, and Christian Lisdat. A strontium lattice clock with 3×10^{-17} inaccuracy and its frequency. *New Journal of Physics*, 16(7):073023, 2014.

[25] V V Flambaum and V A Dzuba. Search for variation of the fundamental constants in atomic, molecular, and nuclear spectra. *Canadian Journal of Physics*, 87(1):25–33, 2009.

[26] Kurt Gibble. Decoherence and collisional frequency shifts of trapped bosons and fermions. *Phys. Rev. Lett.*, 103:113202, Sep 2009.

[27] Kurt Gibble. Scattering of cold-atom coherences by hot atoms: Frequency shifts from background-gas collisions. *Phys. Rev. Lett.*, 110:180802, May 2013.

[28] R. M. Godun, P. B. R. Nisbet-Jones, J. M. Jones, S. A. King, L. A. M. Johnson, H. S. Margolis, K. Szymaniec, S. N. Lea, K. Bongs, and P. Gill. Frequency ratio of two optical clock transitions in ^{171}Yb$^+$ and constraints on the time variation of fundamental constants. *Phys. Rev. Lett.*, 113:210801, Nov 2014.

[29] Tim Gould and Tomas Bucko. C6 coefficients and dipole polarizabilities for all atoms and many ions in rows 1-6 of the periodic table. *Journal of Chemical Theory and Computation*, 12(8):3603–3613, 2016. PMID: 27304856.

[30] Rudolf Grimm, Matthias Weidemüller, and Yurii B. Ovchinnikov. Optical dipole traps for neutral atoms. volume 42 of *Advances In Atomic, Molecular, and Optical Physics*, pages 95 – 170. Academic Press, 2000.

[31] G. Grynberg and C. Robilliard. Cold atoms in dissipative optical lattices. *Physics Reports*, 355(5):335 – 451, 2001.

[32] J Guéna, M Abgrall, A Clairon, and S Bize. Contributing to TAI with a secondary representation of the SI second. *Metrologia*, 51(1):108, 2014.

[33] J. Guéna, M. Abgrall, D. Rovera, P. Laurent, B. Chupin, M. Lours, G. Santarelli, P. Rosenbusch, M.E. Tobar, Ruoxin Li, K. Gibble, A. Clairon, and S. Bize. Progress in atomic fountains at LNE − SYRTE. *Ultrasonics, Ferroelectrics, and Frequency Control, IEEE Transactions on*, 59(3):391–409, March 2012.

[34] J Guéna, S Weyers, M Abgrall, C Grebing, V Gerginov, P Rosenbusch, S Bize, B Lipphardt, H Denker, N Quintin, S M F Raupach, D Nicolodi, F Stefani, N Chiodo, S Koke, A Kuhl, F Wiotte, F Meynadier, E Camisard, C Chardonnet, Y Le Coq, M Lours, G Santarelli, A Amy-Klein, R Le Targat, O Lopez, P E Pottie, and G Grosche. First international comparison of fountain primary frequency standards via a long distance optical fiber link. *Metrologia*, 54(3):348, 2017.

[35] H. Hachisu, K. Miyagishi, S. G. Porsev, A. Derevianko, V. D. Ovsiannikov, V. G. Pal'chikov, M. Takamoto, and H. Katori. Trapping of neutral mercury atoms and prospects for optical lattice clocks. *Phys. Rev. Lett.*, 100:053001, Feb 2008.

[36] D. M. Harber, H. J. Lewandowski, J. M. McGuirk, and E. A. Cornell. Effect of cold collisions on spin coherence and resonance shifts in a magnetically trapped ultracold gas. *Phys. Rev. A*, 66:053616, Nov 2002.

[37] N. Hinkley, J. A. Sherman, N. B. Phillips, M. Schioppo, N. D. Lemke, K. Beloy, M. Pizzocaro, C. W. Oates, and A. D. Ludlow. An atomic clock with 10^{-18} instability. *Science*, 341(6151):1215–1218, 2013.

[38] N. Huntemann, B. Lipphardt, Chr. Tamm, V. Gerginov, S. Weyers, and E. Peik. Improved limit on a temporal variation of m_p/m_e from comparisons of Yb^+ and Cs atomic clocks. *Phys. Rev. Lett.*, 113:210802, Nov 2014.

[39] N. Huntemann, C. Sanner, B. Lipphardt, Chr. Tamm, and E. Peik. Single-ion atomic clock with 3×10^{-18} systematic uncertainty. *Phys. Rev. Lett.*, 116:063001, Feb 2016.

[40] W. M. Itano, J. C. Bergquist, J. J. Bollinger, J. M. Gilligan, D. J. Heinzen, F. L. Moore, M. G. Raizen, and D. J. Wineland. Quantum projection noise: Population fluctuations in two-level systems. *Phys. Rev. A*, 47:3554–3570, May 1993.

[41] R. Jáuregui, N. Poli, G. Roati, and G. Modugno. Anharmonic parametric excitation in optical lattices. *Phys. Rev. A*, 64:033403, Aug 2001.

[42] B Jian, P Dubé, and A A Madej. Quantum projection noise limited stability of a ^{88}Sr$^+$ atomic clock. *Journal of Physics: Conference Series*, 723(1):012023, 2016.

[43] H. Katori. Spectroscopy of strontium atoms in the Lamb-Dicke confinement. In *Proc. of the 6th Symposium on Frequency Standards and Metrology*, page 323. World scientific, Singapore, 2001.

[44] Hidetoshi Katori, V. D. Ovsiannikov, S. I. Marmo, and V. G. Palchikov. Strategies for reducing the light shift in atomic clocks. *Phys. Rev. A*, 91:052503, May 2015.

[45] Hidetoshi Katori, Masao Takamoto, V. G. Pal'chikov, and V. D. Ovsiannikov. Ultrastable optical clock with neutral atoms in an engineered light shift trap. *Phys. Rev. Lett.*, 91:173005, Oct 2003.

[46] M. Kazda, V. Gerginov, N. Huntemann, B. Lipphardt, and S. Weyers. Phase analysis for frequency standards in the microwave and optical domains. *IEEE Transactions on Ultrasonics, Ferroelectrics, and Frequency Control*, 63(7):970–974, July 2016.

[47] J Keller, T Burgermeister, D Kalincev, J Kiethe, and T E Mehlstäubler. Evaluation of trap-induced systematic frequency shifts for a multi-ion optical clock at the 10^{-19} level. *Journal of Physics: Conference Series*, 723(1):012027, 2016.

[48] T. Kessler, C. Hagemann, C. Grebing, T. Legero, U. Sterr, F. Riehle, M. J. Martin, L. Chen, and J. Ye. A sub-40-mHz-linewidth laser based on a silicon single-crystal optical cavity. *Nat Photon*, 6(10):687–692, October 2012.

[49] S. B. Koller, J. Grotti, St. Vogt, A. Al-Masoudi, S. Dörscher, S. Häfner, U. Sterr, and Ch. Lisdat. Transportable optical lattice clock with 7×10^{-17} uncertainty. *Phys. Rev. Lett.*, 118:073601, Feb 2017.

[50] A. P. Kulosa, D. Fim, K. H. Zipfel, S. Rühmann, S. Sauer, N. Jha, K. Gibble, W. Ertmer, E. M. Rasel, M. S. Safronova, U. I.

Safronova, and S. G. Porsev. Towards a Mg lattice clock: Observation of the $^1S_0-^3P_0$ transition and determination of the magic wavelength. *Phys. Rev. Lett.*, 115:240801, Dec 2015.

[51] L.D. Landau and E.M. Lifshitz. *Quantum Mechanics: Non-Relativistic Theory.* Course of Theoretical Physics. Elsevier Science, 1981.

[52] R. Le Targat, L. Lorini, Y. Le Coq, M. Zawada, J. Guéna, M. Abgrall, M. Gurov, P. Rosenbusch, D. G. Rovera, B. Nagórny, R. Gartman, P. G. Westergaard, M. E. Tobar, M. Lours, G. Santarelli, A. Clairon, S. Bize, P. Laurent, P. Lemonde, and J. Lodewyck. Experimental realization of an optical second with strontium lattice clocks. *Nat Commun*, 4:–, jul 2013.

[53] D. Leibfried, R. Blatt, C. Monroe, and D. Wineland. Quantum dynamics of single trapped ions. *Rev. Mod. Phys.*, 75:281–324, Mar 2003.

[54] N. D. Lemke, A. D. Ludlow, Z. W. Barber, T. M. Fortier, S. A. Diddams, Y. Jiang, S. R. Jefferts, T. P. Heavner, T. E. Parker, and C. W. Oates. Spin-$1/2$ optical lattice clock. *Phys. Rev. Lett.*, 103:063001, Aug 2009.

[55] N. D. Lemke, J. von Stecher, J. A. Sherman, A. M. Rey, C. W. Oates, and A. D. Ludlow. p-wave cold collisions in an optical lattice clock. *Phys. Rev. Lett.*, 107:103902, Aug 2011.

[56] C. Lisdat, G. Grosche, N. Quintin, C. Shi, S.M.F. Raupach, C. Grebing, D. Nicolodi, F. Stefani, A. Al-Masoudi, S. Dörscher, S. Häfner, J.-L. Robyr, N. Chiodo, S. Bilicki, E. Bookjans, A. Koczwara, S. Koke, A. Kuhl, F. Wiotte, F. Meynadier, E. Camisard, M. Abgrall, M. Lours, T. Legero, H. Schnatz, U. Sterr, H. Denker, C. Chardonnet, Y. Le Coq, G. Santarelli, A. Amy-Klein, R. Le Targat, J. Lodewyck, O Lopez, and P.-E. Pottie. A clock network for geodesy and fundamental science. *Nature Communications*, 7:12443–, August 2016.

[57] Jérôme Lodewyck, Slawomir Bilicki, Eva Bookjans, Jean-Luc Robyr, Chunyan Shi, Grégoire Vallet, Rodolphe Le Targat, Daniele Nicolodi, Yann Le Coq, Jocelyne Guéna, Michel Abgrall,

Peter Rosenbusch, and Sébastien Bize. Optical to microwave clock frequency ratios with a nearly continuous strontium optical lattice clock. *Metrologia*, 53(4):1123, 2016.

[58] A. D. Ludlow, T. Zelevinsky, G. K. Campbell, S. Blatt, M. M. Boyd, M. H. G. de Miranda, M. J. Martin, J. W. Thomsen, S. M. Foreman, Jun Ye, T. M. Fortier, J. E. Stalnaker, S. A. Diddams, Y. Le Coq, Z. W. Barber, N. Poli, N. D. Lemke, K. M. Beck, and C. W. Oates. Sr lattice clock at 1×10^{-16} fractional uncertainty by remote optical evaluation with a Ca clock. *Science*, 319(5871):1805–1808, 2008.

[59] Andrew D. Ludlow, Martin M. Boyd, Jun Ye, E. Peik, and P. O. Schmidt. Optical atomic clocks. *Rev. Mod. Phys.*, 87:637–701, Jun 2015.

[60] M. D. Lukin, M. Fleischhauer, R. Cote, L. M. Duan, D. Jaksch, J. I. Cirac, and P. Zoller. Dipole blockade and quantum information processing in mesoscopic atomic ensembles. *Phys. Rev. Lett.*, 87:037901, Jun 2001.

[61] Christian D. Marciniak, Harrison B. Ball, Alex T.-H. Hung, and Michael J. Biercuk. Towards fully commercial, UV-compatible fiber patch cords. *Opt. Express*, 25(14):15643–15661, Jul 2017.

[62] Michael J. Martin. *Quantum Metrology and Many-Body Physics: Pushing the Frontier of the Optical Lattice Clock*. PhD thesis, University of Colorado, 2013.

[63] J. J. McFerran, D. V. Magalhaes, C. Mandache, J. Millo, W. Zhang, Y. Le Coq, G. Santarelli, and S. Bize. Laser locking of the $^{199}\mathrm{Hg}\,^1\mathrm{S}_0 - {}^3\mathrm{P}_0$ transition with 5.7×10^{-15} fractional frequency instability. *Opt. Lett.*, 37(17):3477–3479, Sep 2012.

[64] J. J. McFerran, L. Yi, S. Mejri, and S. Bize. Sub-doppler cooling of fermionic Hg isotopes in a magneto-optical trap. *Opt. Lett.*, 35(18):3078–3080, 2010.

[65] J. J. McFerran, L. Yi, S. Mejri, S. Di Manno, W. Zhang, J. Guéna, Y. Le Coq, and S. Bize. Neutral atom frequency reference in the deep ultraviolet with fractional uncertainty $= 5.7 \times 10^{-15}$. *Phys. Rev. Lett.*, 108:183004, May 2012.

[66] J. J. McFerran, L. Yi, S. Mejri, S. Di Manno, W. Zhang, J. Guéna, Y. Le Coq, and S. Bize. Erratum: Neutral atom frequency reference in the deep ultraviolet with fractional uncertainty = 5.7×10^{-15} [phys. rev. lett. 108, 183004 (2012)]. *Phys. Rev. Lett.*, 115:219901, Nov 2015.

[67] D. Meiser, Jun Ye, D. R. Carlson, and M. J. Holland. Prospects for a millihertz-linewidth laser. *Phys. Rev. Lett.*, 102:163601, Apr 2009.

[68] S. Mejri, J. J. McFerran, L. Yi, Y. Le Coq, and S. Bize. Ultraviolet laser spectroscopy of neutral mercury in a one-dimensional optical lattice. *Phys. Rev. A*, 84:032507, Sep 2011.

[69] H. J. Metcalf and P. van der Straten. Laser cooling and trapping of atoms. *J. Opt. Soc. Am. B*, 20(5):887–908, May 2003.

[70] Thomas Middelmann, Stephan Falke, Christian Lisdat, and Uwe Sterr. High accuracy correction of blackbody radiation shift in an optical lattice clock. *Phys. Rev. Lett.*, 109:263004, Dec 2012.

[71] J. Millo, D. V. Magalhães, C. Mandache, Y. Le Coq, E. M. L. English, P. G. Westergaard, J. Lodewyck, S. Bize, P. Lemonde, and G. Santarelli. Ultrastable lasers based on vibration insensitive cavities. *Phys. Rev. A*, 79:053829, May 2009.

[72] Peter J. Mohr, David B. Newell, and Barry N. Taylor. CODATA recommended values of the fundamental physical constants: 2014. *Rev. Mod. Phys.*, 88:035009, Sep 2016.

[73] Nils Nemitz, Takuya Ohkubo, Masao Takamoto, Ichiro Ushijima, Manoj Das, Noriaki Ohmae, and Hidetoshi Katori. Frequency ratio of Yb and Sr clocks with 5×10^{-17} uncertainty at 150 seconds averaging time. *Nat Photon*, 10(4):258–261, apr 2016.

[74] T. L. Nicholson, M. J. Martin, J. R. Williams, B. J. Bloom, M. Bishof, M. D. Swallows, S. L. Campbell, and J. Ye. Comparison of two independent Sr optical clocks with 1×10^{-17} stability at 10^3 s. *Phys. Rev. Lett.*, 109:230801, Dec 2012.

[75] T.L. Nicholson, S.L. Campbell, R.B. Hutson, G.E. Marti, B.J. Bloom, R.L. McNally, W. Zhang, M.D. Barrett, M.S. Safronova,

G.F. Strouse, W.L. Tew, and J. Ye. Systematic evaluation of an atomic clock at 2×10^{-18} total uncertainty. *Nat Commun*, 6:–, apr 2015.

[76] Daniele Nicolodi, Berengere Argence, Wei Zhang, Rodolphe Le Targat, Giorgio Santarelli, and Yann Le Coq. Spectral purity transfer between optical wavelengths at the 10^{-18} level. *Nat Photon*, 8(3):219–223, March 2014.

[77] Matthew A. Norcia, Matthew N. Winchester, Julia R. K. Cline, and James K. Thompson. Superradiance on the millihertz linewidth strontium clock transition. *Science Advances*, 2(10), 2016.

[78] Noriaki Ohmae, Naoya Kuse, Martin E. Fermann, and Hidetoshi Katori. All-polarization-maintaining, single-port Er:fiber comb for high-stability comparison of optical lattice clocks. *Applied Physics Express*, 10(6):062503, 2017.

[79] V. D. Ovsiannikov, S. I. Marmo, V. G. Palchikov, and H. Katori. Higher-order effects on the precision of clocks of neutral atoms in optical lattices. *Phys. Rev. A*, 93:043420, Apr 2016.

[80] V D Ovsyannikov, Vitalii G Pal'chikov, H Katori, and M Takamoto. Polarisation and dispersion properties of light shifts in ultrastable optical frequency standards. *Quantum Electronics*, 36(1):3, 2006.

[81] Wolfgang Paul. Electromagnetic traps for charged and neutral particles. *Rev. Mod. Phys.*, 62:531–540, Jul 1990.

[82] F. Pereira Dos Santos, H. Marion, S. Bize, Y. Sortais, A. Clairon, and C. Salomon. Controlling the cold collision shift in high precision atomic interferometry. *Phys. Rev. Lett.*, 89:233004, Nov 2002.

[83] M. Petersen, R. Chicireanu, S. T. Dawkins, D. V. Magalhães, C. Mandache, Y. Le Coq, A. Clairon, and S. Bize. Doppler-free spectroscopy of the ${}^1\text{S}_0 - {}^3\text{P}_0$ optical clock transition in laser-cooled fermionic isotopes of neutral mercury. *Phys. Rev. Lett.*, 101:183004, Oct 2008.

[84] M. Petersen, J. Millo, D.V. Magalhães, C. Mandache, S.T. Dawkins, R. Chicireanu, Y. Lecoq, O. Acef, G. Santarelli, A. Clairon, and S. Bize. Magneto-optical trap of neutral mercury for an optical lattice clock. 2008.

[85] Michael M. Petersen. *Laser-cooling of Neutral Mercury and Laser-spectroscopy of the* $^1S_0 - ^3P_0$ *optical clock transition*. PhD thesis, Université Paris VI, 2009.

[86] Gérard Petit, Felicitas Arias, and Gianna Panfilo. International atomic time: Status and future challenges. *Comptes Rendus Physique*, 16(5):480 – 488, 2015. The measurement of time / La mesure du temps.

[87] S. G. Porsev, U. I. Safronova, and M. S. Safronova. A theoretical study of the g-factor of the 6s6p $^3P_0$ state of mercury. *ArXiv e-prints*, March 2017.

[88] Audrey Quessada, Richard P Kovacich, Irène Courtillot, André Clairon, Giorgio Santarelli, and Pierre Lemonde. The Dick effect for an optical frequency standard. *Journal of Optics B: Quantum and Semiclassical Optics*, 5(2):S150, 2003.

[89] E. L. Raab, M. Prentiss, Alex Cable, Steven Chu, and D. E. Pritchard. Trapping of neutral sodium atoms with radiation pressure. *Phys. Rev. Lett.*, 59:2631–2634, Dec 1987.

[90] L. Ricci, M. Weidemüller, T. Esslinger, A. Hemmerich, C. Zimmermann, V. Vuletic, W. König, and T.W. Hänsch. A compact grating-stabilized diode laser system for atomic physics. *Optics Communications*, 117(5):541 – 549, 1995.

[91] Fritz Riehle. *Atomic and Molecular Frequency References, in Frequency Standards: Basics and Applications*, pages 117–165. Wiley-VCH Verlag GmbH & Co. KGaA, 2005.

[92] Fritz Riehle. *Preparation and Interrogation of Atoms and Molecules, in Frequency Standards: Basics and Applications*, pages 167–202. Wiley-VCH Verlag GmbH & Co. KGaA, 2005.

[93] Fritz Riehle. Towards a redefinition of the second based on optical atomic clocks. *Comptes Rendus Physique*, 16(5):506 – 515, 2015. The measurement of time / La mesure du temps.

[94] Fritz Riehle. Optical clock networks. *Nat Photon*, 11(1):25–31, January 2017.

[95] Erling Riis, David S. Weiss, Kathryn A. Moler, and Steven Chu. Atom funnel for the production of a slow, high-density atomic beam. *Phys. Rev. Lett.*, 64:1658–1661, Apr 1990.

[96] T. Rosenband, D. B. Hume, P. O. Schmidt, C. W. Chou, A. Brusch, L. Lorini, W. H. Oskay, R. E. Drullinger, T. M. Fortier, J. E. Stalnaker, S. A. Diddams, W. C. Swann, N. R. Newbury, W. M. Itano, D. J. Wineland, and J. C. Bergquist. Frequency ratio of Al^+ and Hg^+ single-ion optical clocks; metrology at the 17th decimal place. *Science*, 319(5871):1808–1812, 2008.

[97] G D Rovera, S Bize, B Chupin, J Guéna, Ph Laurent, P Rosenbusch, P Uhrich, and M Abgrall. $UTC(OP)$ based on $LNE-SYRTE$ atomic fountain primary frequency standards. *Metrologia*, 53(3):S81, 2016.

[98] G. Santarelli, C. Audoin, A. Makdissi, P. Laurent, G. J. Dick, and A. Clairon. Frequency stability degradation of an oscillator slaved to a periodically interrogated atomic resonator. *IEEE Transactions on Ultrasonics, Ferroelectrics, and Frequency Control*, 45(4):887–894, July 1998.

[99] G. Santarelli, G. Governatori, D. Chambon, M. Lours, P. Rosenbusch, J. Guena, F. Chapelet, S. Bize, M. E. Tobar, P. Laurent, T. Potier, and A. Clairon. Switching atomic fountain clock microwave interrogation signal and high-resolution phase measurements. *IEEE Transactions on Ultrasonics, Ferroelectrics, and Frequency Control*, 56(7):1319–1326, July 2009.

[100] G. Santarelli, Ph. Laurent, P. Lemonde, A. Clairon, A. G. Mann, S. Chang, A. N. Luiten, and C. Salomon. Quantum projection noise in an atomic fountain: A high stability cesium frequency standard. *Phys. Rev. Lett.*, 82:4619–4622, Jun 1999.

[101] L De Sarlo, M Favier, R Tyumenev, and S Bize. A mercury optical lattice clock at $LNE-SYRTE$. *Journal of Physics: Conference Series*, 723(1):012017, 2016.

[102] M. Schioppo, Brown R. C., McGrew W. F., Hinkley N., Fasano R. J., Beloy K., Yoon T. H., Milani G., Nicolodi D., Sherman J. A., Phillips N. B., Oates C. W., and Ludlow A. D. Ultrastable optical clock with two cold-atom ensembles. *Nat Photon*, 11(1):48–52, jan 2017.

[103] J. A. Sherman, N. D. Lemke, N. Hinkley, M. Pizzocaro, R. W. Fox, A. D. Ludlow, and C. W. Oates. High-accuracy measurement of atomic polarizability in an optical lattice clock. *Phys. Rev. Lett.*, 108:153002, Apr 2012.

[104] Matthew D. Swallows, Michael Bishof, Yige Lin, Sebastian Blatt, Michael J. Martin, Ana Maria Rey, and Jun Ye. Suppression of collisional shifts in a strongly interacting lattice clock. *Science*, 331(6020):1043–1046, 2011.

[105] Masao Takamoto, Feng-Lei Hong, Ryoichi Higashi, Yasuhisa Fujii, Michito Imae, and Hidetoshi Katori. Improved frequency measurement of a one-dimensional optical lattice clock with a spin-polarized fermionic ^{87}Sr isotope. *Journal of the Physical Society of Japan*, 75(10):104302, 2006.

[106] Masao Takamoto and Hidetoshi Katori. Spectroscopy of the ^{1}S$_0$ $-^3$ P$_0$ clock transition of ^{87}Sr in an optical lattice. *Phys. Rev. Lett.*, 91(22):223001, Nov 2003.

[107] Masao Takamoto, Tetsushi Takano, and Hidetoshi Katori. Frequency comparison of optical lattice clocks beyond the dick limit. *Nat Photon*, 5(5):288–292, May 2011.

[108] Tetsushi Takano, Ray Mizushima, and Hidetoshi Katori. Precise determination of the isotope shift of ^{88}Sr-^{87}Sr optical lattice clock by sharing perturbations. *Applied Physics Express*, 10(7):072801, 2017.

[109] Tetsushi Takano, Masao Takamoto, Ichiro Ushijima, Noriaki Ohmae, Tomoya Akatsuka, Atsushi Yamaguchi, Yuki Kuroishi, Hiroshi Munekane, Basara Miyahara, and Hidetoshi Katori. Geopotential measurements with synchronously linked optical lattice clocks. *Nat Photon*, 10(10):662–666, oct 2016.

[110] H.R. Telle, B. Lipphardt, and J. Stenger. Kerr-lens, mode-locked lasers as transfer oscillators for optical frequency measurements. *Applied Physics B*, 74(1):1–6, Jan 2002.

[111] R Tyumenev, M Favier, S Bilicki, E Bookjans, R Le Targat, J Lodewyck, D Nicolodi, Y Le Coq, M Abgrall, J Guéna, L De Sarlo, and S Bize. Comparing a mercury optical lattice clock with microwave and optical frequency standards. *New Journal of Physics*, 18(11):113002, 2016.

[112] Rinat Tyumenev. *Mercury lattice clock: from the Lamb-Dicke spectroscopy to stable clock operation*. PhD thesis, Université Paris VI, 2015.

[113] Ichiro Ushijima, Masao Takamoto, Manoj Das, Takuya Ohkubo, and Hidetoshi Katori. Cryogenic optical lattice clocks. *Nat Photon*, 9(3):185–189, mar 2015.

[114] Jean-Philippe Uzan. Varying constants, gravitation and cosmology. *Living Reviews in Relativity*, 14(2), 2011.

[115] Philip G. Westergaard, Bjarke T. R. Christensen, David Tieri, Rastin Matin, John Cooper, Murray Holland, Jun Ye, and Jan W. Thomsen. Observation of motion-dependent nonlinear dispersion with narrow-linewidth atoms in an optical cavity. *Phys. Rev. Lett.*, 114:093002, Mar 2015.

[116] D. J. Wineland and Wayne M. Itano. Laser cooling of atoms. *Phys. Rev. A*, 20:1521–1540, Oct 1979.

[117] D.J. Wineland, C. Monroe, W.M. Itano, D. Leibfried, B.E. King, and D.M. Meekhof. Experimental issues in coherent quantum-state manipulation of trapped atomic ions. *Journal of Research of the National Institute of Standards and Technology*, 103(3):259–328, 1998. cited By 836.

[118] Kazuhiro Yamanaka, Noriaki Ohmae, Ichiro Ushijima, Masao Takamoto, and Hidetoshi Katori. Frequency ratio of ^{199}Hg and ^{87}Sr optical lattice clocks beyond the SI limit. *Phys. Rev. Lett.*, 114:230801, Jun 2015.

[119] Jun Ye, Jin-Long Peng, R. Jason Jones, Kevin W. Holman, John L. Hall, David J. Jones, Scott A. Diddams, John Kitching, Sebastien Bize, James C. Bergquist, Leo W. Hollberg, Lennart Robertsson, and Long-Sheng Ma. Delivery of high-stability optical and microwave frequency standards over an optical fiber network. *J. Opt. Soc. Am. B*, 20(7):1459–1467, Jul 2003.

[120] L. Yi, S. Mejri, J. J. McFerran, Y. Le Coq, and S. Bize. Optical lattice trapping of ^{199}Hg and determination of the magic wavelength for the ultraviolet ^{1}S$_0$ $\leftrightarrow^3$ P$_0$ clock transition. *Phys. Rev. Lett.*, 106:073005, Feb 2011.